HyMARC: A Consortium for Advancing Hydrogen Storage Materials

Thomas Gennett (National Renewable Energy Laboratory [NREL]) and Mark Allendorf (Sandia National Laboratories [SNL]) (Primary Contacts); Jeffrey Long (Lawrence Berkeley National Laboratory [LBNL]), Tom Autrey (Pacific Northwest National Laboratory [PNNL]), David Prendergast (LBNL), Michael Toney (SLAC National Accelerator Laboratory [SLAC]), Craig Brown, and Terry Udovic (National Institute of Standards and Technology [NIST])
National Renewable Energy Laboratory
15013 Denver West Parkway
Golden, CO 80401
Phone: 303-384-6628
Email: thomas.gennett@nrel.gov, mdallen@sandia.gov

Participants
- **NREL:** Phil Parilla, Katie Hurst, Steve Christensen, Kristin Munch, Courtney Pailing, Wade Braunecker, John Perkins, Sarah Shulda, Robert Bell, Noemi Leick, Madison Martinez, Jacob Tarver (NIST), Mira Dimitrievska (NIST), Nick Strange (SLAC), Gayle Bentley, Ashley Gaulding, Rachel Mow, Glory Russell-Parks, Brian Trewyn, Colin Wolden
- **SNL:** Vitalie Stavila, Lennie Klebanoff, Rob Kolasinski, Farid El Gabaly, Xiaowang Zhao, Annabelle Benin, James White
- **PNNL:** Mark Bowden, Abhi Karkamkar, Bojana Ginovska, Samantha Johnson, Ba Tran, Kriston Brooks
- **LLNL:** Tae Wook Heo, ShinYoung Kang, Liwen Wan, Keith Ray, Rongpei Shi, Alex Baker, Jonathan Lee
- **LBNL:** Martin Head-Gordon, Hanna Breunig, Hiroyasu Furukawa, Jeff Urban.

DOE Manager: Ned Stetson
Phone: 202-586-9995
Email: Ned.Stetson@ee.doe.gov

Project Start Date: October 1, 2015
Project End Date: September 30, 2022

Overall Objectives

- Advance the core competencies of the DOE Fuel Cell Technologies Office (FCTO) program as related to the characterization, evaluation, qualification, and validation of next-generation and current hydrogen storage materials.
- Expand the foundational knowledge base required to understand and modify the thermodynamic and kinetic limitations of hydrogen storage and carrier materials to accelerate the development and discovery of successful materials.
- Support the Hydrogen Materials Advanced Research Consortium (HyMARC) seedling projects using the core capabilities and expertise that exist within the HyMARC Energy Materials Network.
- Initiate a research effort focused on hydrogen carriers that will investigate pathways leading to optimized materials for efficient, safe, and economical transport of hydrogen from a production facility to the city gate.
- Develop a Data Hub for hosting, sharing, and making key datasets available to the public, based on the data needs and publication processes of the HyMARC consortium. A key component to accelerating research across a diverse portfolio with research teams positioned across the United States is data accessibility.
- Develop a series of advanced characterization tools that allow for rapid advancement and in-depth understanding of next-generation hydrogen storage materials.
- Demonstrate the importance of computational methods in developing and understanding next-generation hydrogen storage materials.
- Validate new concepts for hydrogen storage mechanisms in adsorbents and hydrides.
- Accelerate discovery of breakthrough storage materials by developing foundational understanding of phenomena governing thermodynamics and kinetics.
- Develop community tools and capabilities to enable materials discovery, including computational models and databases, new characterization tools and methods, and tailorable synthetic platforms.
- Provide gas sorption and other property data needed to develop thermodynamic models of sorbents and metal hydrides, including the effects of ultrahigh hydrogen pressure.

- Synthesize metal hydrides and sorbents in a variety of formats (e.g., bulk powders, thin films, nanostructures) and develop in situ techniques for their characterization.
- Identify the structure, composition, and reactivity of gas-surface and solid-solid hydride surfaces contributing to rate-limiting desorption and uptake.

Fiscal Year (FY) 2019 Objectives

- Establish the thermodynamic properties of sorbent materials for sorption/desorption cycles under the practical conditions expected for on-board hydrogen systems. This includes the prediction and measurement for such properties as enthalpy, entropy, binding energies, heat capacity, and thermal conductivity.
- Benchmarking theory:
  - Couple theory with experiment to benchmark and validate the computational predictions.
  - Unravel complex phenomena, guide experimental work, and accelerate progress.
  - Provide accurate computational modeling for hydrogen adsorbed in porous and hydride materials.
- Enhance volumetric capacities in parallel to current seedling projects through materials design and/or crystallite growth processes.
- Investigate both the step-function isotherms in expandable metal organic frameworks (MOFs) and focus efforts to understand how mass transport limits can be controlled within dynamic pore structures for high-surface-area materials.
- Develop sorbents with a greater density of strong binding sites on the pore surface.
- Compute predictions of metal hydride thermodynamics that fully account for both enthalpic and entropic effects. Develop a more general protocol to provide data for a wider range of hydrides.
- Expand strategies for thermodynamic tuning through new synthetic routes and prototype models that iterate with experiments to establish confidence in predictions.
- Develop kinetic predictions using multiscale modeling with models simulating phase nucleation, growth, and mass transport/diffusion that simulate processes occurring at length scales ranging from single-digit nanometers to tens of microns, thereby allowing the effects of grain boundaries, phase nucleation, and mass transport kinetics to be assessed.
- Integrate spectroscopy and theory though combining several spectroscopies to probe surface, near-surface, and bulk length scales.
- Develop alternate approaches to prepare baseline hydrogen carriers (i.e., NH_3 and CH_3OH) without molecular hydrogen.
- Develop alternate hydrogen carriers through new concepts in liquids and solids.
- Establish the catalytic processes for chemical compression of hydrogen through the use of catalyst materials.
- Establish new processes for the loading and unloading of hydrogen from carriers through the use of thermal, light, or pressure activated processes.
- Determine cost of transport at modeled temperature and pressure conditions for adsorbents in a techno-economic analysis.
- Advance the characterization capabilities through collaborations at various DOE user facilities.
- Develop a Data Hub for hosting, sharing, and making key datasets available to the public, based on the data needs and publication processes of the HyMARC consortium.
- Measure H_2 isotherms to validate a computational model used to screen catalysts that can accelerate hydrogen uptake.
- Model the interactions between B_xH_y species using density functional theory and use the results to generate pair potentials needed to simulate metal hydride decomposition.
- Determine theoretical limits of confinement-induced entropy changes in complex metal

hydrides using molecular dynamics simulations of surface energies

- Implement an Explainable Machine Learning approach to identify property-feature relationships.
- Develop catalysts based on MOFs to facilitate release of H_2 from alcohols and polyols with potential to serve as hydrogen carriers.

Technical Barriers

This project addresses the following technical barriers from the Hydrogen Storage section of the FCTO Multi-Year Research, Development, and Demonstration Plan[1]:

General:

- Cost
- Weight
- Volume
- Efficiency
- Refueling time.

Reversible Solid-State Material:

- Hydrogen capacity and reversibility
- Understanding of hydrogen physi- and chemisorption
- Test protocols and evaluation facilities.

Technical Targets

Hydrogen Storage Materials: This project is conducting validation studies of various framework materials, sorbents, hydrides**,** and model compounds. Concurrently, the team also is developing new characterization tools for the rapid enhancement of materials development. Insights gained from these studies will be applied toward the design and synthesis of hydrogen storage materials that meet the DOE onboard 2020 automotive hydrogen storage targets shown in Table 1.

FY 2019 Accomplishments

- Established a pathway for the utilization of porous liquids as possible hydrogen carriers.
  - *Particle size*: Demonstrated control of 3-D "COF-300" colloids from 50 nm to 600 nm.
  - *Surface area*: Improved covalent organic framework (COF) colloids from 20 m^2/g with modified literature procedure to 500 m^2/g using new catalyst/conditions; "regrowth" technique further improves to 1400 m^2/g, but no longer colloidal.
  - *Resuspension/purification*: Developed protocol to purify colloids in solution using centrifugation (all existing literature on colloidal COFs reports irreversible aggregation during purification).
  - *Functionalization of COF colloids*: Successfully tethered ionic liquids (ILs) and other functional groups to COF shell using several different synthetic approaches, and verified functionalization with diffuse reflectance infrared Fourier transform spectroscopy (DRIFTS). Functionalization helps facilitate suspension of colloids in bulk ILs (no settling/floating of particles after 6 h of centrifuging).
  - *Porous liquid*: Successfully synthesized first stable COF/IL-based porous liquids. Solid state nuclear magnetic resonance (NMR) experiments currently underway probing structure-property relationships regarding solvent exclusion from COF pores.
  - *COF monolith:* Developed protocol for first COF-based monolith (characterization and patent application underway).
  - *H_2 desorption*: Confirmed solubility of H_2 in certain ILs with temperature programmed desorption (TPD). H_2 desorption studies in the first COF/IL-based porous liquids are underway.
- Determined three no-go projects.
- Expanded the capabilities of the thermal conductivity apparatus to conduct measurements under two different dosing conditions: equilibrium pressure and stoichiometric micro-dosing conditions.

[1] https://www.energy.gov/eere/fuelcells/downloads/fuel-cell-technologies-office-multi-year-research-development-and-22

- Established issues and corrected same that could affect the accuracy in determining isosteric heats (Q_{st}) from isotherm data.
- Developed and validated a high-temperature pressure, composition, temperature (PCT) capability.
- Enhanced low temperature melt/solidification cyclability of $Mg(BH_4)_2$ via a novel additive, tetramethylammonium borohydride (TMAB). TMAB also affects the melt/solidification behavior of $Mg(BH_4)_2$:xTHF samples.
- Deposited thin film TiN coatings with thicknesses ranging from 5 to 20 nm onto MgH_2 particles by atomic layer deposition (ALD).
- Selected the Mg-MgH_2 system for an encapsulation experiment designed to test metal hydrides under mechanical stress.
- Optical properties and X-ray absorption spectroscopy (XAS) of ALD TiN thin films on Si showed the incorporation of oxygen into TiN film.
- Found synthetic methodology for altering the plasmon frequency of TiN coatings.
- Demonstrated reproducible hydrogen measurements in the flat-cell design measurement cell.
- Created a new sample cell that will provide more efficient and uniform exposure of the sample to the light.
- Communicated with the Prendergast group to model TiN/MgH_2 interaction.
- DFT calculations of the energy levels at the TiN/MgH_2 interface showed pathways of electron transfer for TiN to MgH_2.
- Demonstrated light-activated H_2 desorption from two different material systems (TiN/MgH_2, TiO_x/MBH) using LED light at ambient temperature.
- Showed that ALD Al_2O_3 coated TiN mixed with MgH_2 desorbed only 20% of the H_2 desorbed from a TiN+MgH_2 sample.
- Data Hub software upgrade: Updated the open source codebase for the Data Hub to the latest CKAN version (2.8). This provides loads of improved functionality as well as the ability to share the Data Hub instance with other developers as Docker containers.
- New public dataset: Added the Hydrogen Storage Materials Database data and metadata to the Data Hub, with resources to query the data, including a public Jupyter Notebook analyzing and visualizing some of these data.
- Google Analytics and interactive report: Developed a HyMARC Google Analytics report (available here: HyMARC External Report) to capture statistics on usage, such as the Data Hub user demographics and geography, as well as popular downloads.
- New data tool: Deployed the Multi-file Uploader Tool. This data tool performs three main functions: (1) Create a new dataset and upload many files at once of any file type; (2) add many files to an existing dataset; and (3) choose a routine metadata extractor module (based on the instrument and file type) to automatically extract metadata as part of the file upload process. This data tool has FY 2020 plans for further integration and development on the Data Hub user interface.
- New data tool: Developed XRD Unmix for automated analysis of X-ray diffraction (XRD) patterns. By comparing to a reference set of patterns, this tool determines the percentage of each reference pattern present in the experimental spectra.
- Implemented a new in situ capillary-based sample cell for synchrotron X-ray characterization (XRD, small angle X-ray scattering [SAXS], XAS, X-ray Raman scattering [XRS]) at SLAC. Demonstrated new temperature capabilities of the sample cell by performing baseline XRD measurements on γ-$Mg(BH_4)_2$ between -170°C and 600°C. The cell is compatible with XRD (and pair distribution function analysis [PDF]), SAXS, XAS, and XRS techniques under high-pressure, flow, or vacuum and is available to all HyMARC laboratories.
- Provided evidence of pore infiltration of γ-$Mg(BH_4)_2$ with trimethylaluminum (TMA) during ALD coating using results from SAXS—*in collaboration with NREL, Christensen seedling project*.

- Used in situ SAXS to characterize $Mg(BH_4)_2$ infiltrated porous carbons as a function of temperature. The SAXS results suggest that melt-infiltrated templated carbons, CMK-3, retain a fixed size distribution up to ~600°C, which effectively prevents particle agglomeration commonly observed in bulk $Mg(BH_4)_2$—*in collaboration with V. Stavila, Sandia National Laboratories*.
- Used XRD to demonstrate the impact of compression on phenyl and partially fluorinated phenyl COF pellets. Minimal changes in the diffraction for the partially fluorinated COF suggest that the compression has limited influence on crystallinity while effectively reducing the dead space of the powder—*in collaboration with NREL, Johnson seedling project*.
- Provided X-ray characterization support for NREL, SNL, and LBNL with future experiments planned with PNNL and NIST in Fall 2019.
- Evaluated stability of MOFs under high-pressure hydrogen and showed that most are stable to both 5–100 bar H_2 cycling (up to 1,000 cycles) and under 700 bar H_2.
- Developed synthetic routes to monoliths of several Zr-based MOFs, including UiO-66-1,4-NDC, UiO-67, and NU-1000.
- Demonstrated a ≈55% higher volumetric hydrogen uptake in UiO-67 monolith compared to the powder version of this material.
- Established infrastructure for differential scanning calorimetry (DSC) at high pressures (0–431 bar) and temperatures (20°–600°C), including quantitatively measuring the melting point and melting enthalpy of $Mg(BH_4)_2$.
- Probed dehydrogenation and rehydrogenation of the Li-N-H storage system using scanning transmission X-ray microscopy (STXM), which revealed an inversed core-shell structure contradicting the conventional paradigm.
- Demonstrated that eutectic melting of $LiBH_4$-$Mg(BH_4)_2$ mixtures only occurs under very high hydrogen pressure (350 to 1,000 bar), which is required to suppress the dehydrogenation reaction.
- Established a molecular dynamics modeling framework to provide the fundamental basis for theory predictions of energetics and kinetics of hydrogen storage reactions.
- Established in situ X-ray photoelectron spectroscopy XPS and low-energy ion scattering techniques to track hydrogen transport to the surface and subsequent desorption using $Mg(BH_4)_2$ as an example.
- Reported the synthesis of molecularly dispersed $Mg(BH_4)_2$ within the pores of a non-innocent functionalized MOF.
- Created a theory-experimental framework for understanding how additive species react with MgB_2 and how the B-B bonding is disrupted.
- Used Hydrogen Storage Engineering Center of Excellence models to determine the benefits of using nanoconfined metal hydrides (e.g., nano-Li_3N) in an operational hydrogen storage tank.
- Developed "explainable" machine learning method for discovery of new metal hydrides.
- Demonstrated catalytic acceleration of hydrogen production from polyols.
- Synthesized framework materials for physisorption of hydrogen storage at room temperature.
  - Measured the thermodynamics of H_2 binding in $V_2Cl_{2.8}$(btdd) through variable-temperature (VT) DRIFTS measurements.
  - Measured high-pressure ambient temperature H_2 isotherms of Cu(I)-MFU-4*l*.
  - Synthesized variants of UiO-67 containing pyridinyl phenol and bipyridine functionality and achieved quantitative metalation with Cu(I), Re(I), and Mn(I).
  - Demonstrated that metalation with metal carbonyl species allows material activation via pathways other than classical solvent removal, previously the most challenging synthetic step.
  - Synthesized fluorinated derivatives of Co(bdp).
  - Verified successful formation of monolithic HKUST-1 via a sol-gel process.

- Developed infrared (IR) methods for characterizing hydrogen adsorbent materials.
  - Characterized Ca- and Mg-exchanged zeolites with VT Fourier transform infrared (FT-IR) spectroscopy.
  - Developed methods for error analysis for VT FT-IR thermodynamic data.
- Initiated hardware upgrades for FT-IR and NMR analysis at operational conditions.
- Computed binding energies, predicted IR redshift, and performed energy decomposition analysis for molecular hydrogen binding to adsorbents.
- Identified accurate density functionals for hydrogen binding to structures containing main group elements.
- Studied the theoretical performance of an adsorbent-filled fixed-bed tube trailer.
  - Mathematically modeled hydrogen uptake in a tube trailer fixed bed for M_2(dobdc) and M_2(*m*-dobdc) (M = Co and Ni) using a dual-site Langmuir equation.
  - Critically assessed the effects of flow rate, adsorption time, packing densities, thermal management, temperature, purge gas quantity, and bed size on baseline performance of M_2(dobdc) and M_2(*m*-dobdc) (M = Co and Ni).
- Estimated the levelized cost of hydrogen delivery (\$/kg H_2) using M_2(dobdc) and M_2(*m*-dobdc) (M = Co and Ni) and benchmarked results with a 500-bar compressed gas carrier system and cryogenic liquid carrier system (LH_2).
  - Developed detailed energy and material balances for emerging and incumbent hydrogen delivery technologies: MOF-H_2 trucks; 500-bar compressed H_2 trucks, and LH_2.
  - Performed prospective techno-economic analysis to calculate capital and operational costs for a broad range of hydrogen delivery scenarios.
- Hosted webinar with Argonne National Laboratory on "Hydrogen Carriers for Bulk Storage and Transport of Hydrogen" to introduce the concept, approach, and current challenges to the scientific community. https://www.energy.gov/eere/fuelcells/hydrogen-carriers-bulk-storage-and-transport-hydrogen-webinar-text-version
- Measured ΔG^0 (ca. 0 kJ/mol H_2) and showed reversibility of hydrogen uptake and release in formate/bicarbonate reaction couple in collaboration with Korea Institute of Science and Technology and defined a new metric for comparing the storable, transportable, and usable capacity of hydrogen carriers leading to the publication of an invited perspective on hydrogen carriers.
- Measured reversible uptake of hydrogen through four cycles of magnesium borohydride to magnesium deca-borane system below 180°C showing the possibility of multiple cycles.
- Used theory to down-select critical pathways involved with reversible uptake of hydrogen in magnesium borohydride to better understand how to control selectivity.
- Used a combination of XRD and NMR to demonstrate multiply pathways to prepare adducts of magnesium borohydride responsible for low-temperature reversibility.
- Combined in situ NMR and reaction calorimetry to measure the enthalpy of reaction in the first step leading to reversible hydrogen uptake by triborane intermediate to benchmark theory.
- Investigated the potential of using chemical compression in liquid carriers.
- Developed experimental NMR methods to quantify complex product mixtures formed upon hydrogen release and uptake to give the community an approach to compare reactivity of different additives.
- Assisted HyMARC seedling projects (Hawaii) and HyMARC collaborators (NREL, LLNL, SNL, SNS, NIST).
- Devised a new method for estimating nucleation and crystallization driving forces for metal hydride intermediates based on morphology-dependent energetics.
- Refined the advanced phase nucleation modeling framework to examine nucleation

pathways for metal hydrides that involve amorphous intermediates.

- Predicted the nucleation pathway for $Mg(BH_4)_2$ formation, including a possible transition in mechanism under high-pressure cycling conditions.
- Improved the modeling framework for effects of mechanical stress on metal hydride thermodynamics by incorporating the properties of the host medium as well as the effects of packing and loading.
- Demonstrated the first full simulation of metal hydride (de)hydrogenation incorporating chemical reaction, diffusion, stress, and phase transformation kinetics.
- Use computed energetics to show how $Mg(BH_4)_2$ confined in a MOF can exhibit lowered decomposition temperature when confined in a "non-innocent" host.
- Developed a new theory explaining the effects of additives on MgB_2 rehydrogenation in terms of ionic and covalent interaction effects.
- Performed initial energy landscape calculations of gas-phase formation of formic acid hydrogen carriers and their conjugate base formate using Pd catalysts.
- Completed physical incorporation of additives $MgCl_2$, $CaCl_2$, and MgI_2 into $NaBH_4$, which shows that halogens affect to crystal lattice rather than binding energy within the system.
- Significantly reduced the onset of weight loss in $NaBH_4$-$CaCl_2$ additives to below 100°C.
- Synthesized an $MgCl_2$-$Mg(BH_4)_2$ eutectic mixture by a solution-based method, which improves dehydrogenation kinetics in $Mg(BH_4)_2$.
- Demonstrated the Ni/BN catalytic system offers significant benefits for dehydrogenation reaction of liquid organic hydrogen carriers (LOHCs) compared to pure Ni nanoparticle and Ni/Carbon substrates.

Table 1. Progress toward Meeting Technical Targets for Hydrogen Storage Materials

Characteristic	Units	DOE 2020 Storage System Targets	Project Status on Materials Basis
Gravimetric capacity	kg H_2/kg system	0.045 (sorbent)	0.07
Volumetric capacity	kg H_2/L system	0.030 (sorbent)	0.033
PGM total loading	mg-PGM/cm^2_{geo}	≤0.125	0.092, cathode
Min/max delivery temperature	°C	-40/85	-160/30 (sorbent)
Min/max delivery temperature	°C	-40/85	180 (hydride)

PGM – platinum group metal

INTRODUCTION

The DOE FCTO hydrogen storage program supports research and development of technologies to lower the cost of near-term physical storage options and longer-term materials-based hydrogen storage approaches. The program conducts R&D of low-pressure, materials-based technologies and innovative approaches to increase the hydrogen storage capacity, reduce cost, and broaden the range of commercial applications for hydrogen. These advanced-material activities focus on development of core capabilities designed to enable the development of novel materials with the potential to store hydrogen near room temperature, at low-to-moderate pressures, and at energy densities greater than either liquid or compressed hydrogen on a systems basis. Key activities include improving the energetics, temperature, and rates of hydrogen release. Advanced concepts include high-capacity metal hydrides, chemical hydrogen storage materials, and hydrogen sorbent materials, as well as novel material synthesis processes. The overarching goal of the FCTO hydrogen storage program is to develop and demonstrate viable hydrogen storage technologies for transportation, stationary, portable power, and specialty vehicle applications (e.g., material handling equipment, airport ground support equipment), with a key goal of enabling >300-mile driving range across all light-duty vehicle platforms, without reducing vehicle performance or passenger cargo space.

This national laboratory consortium HyMARC brings together internationally recognized leaders in hydrogen storage materials characterization and development to provide a synergistic approach to validate hydrogen storage concepts and develop the key core capabilities necessary for accurate evaluation of hydrogen storage materials capacity, kinetics, and sorption/desorption physio-chemical processes. The overall approach involves collaborative experimental and modeling efforts. We are validating concepts and utilizing core capabilities to rapidly define, model, synthesize, and characterize the appropriate materials necessary for achieving the 2020 hydrogen storage goals set forth by DOE. The approach is multifaceted to mitigate risk and ensure success as we bridge the gap between physisorption and chemisorption to provide the basis for a new generation of hydrogen storage materials technologies.

APPROACH

HyMARC seeks to address critical gaps in the science of hydrogen storage by leveraging recent advances in predictive multiscale modeling, high-resolution in situ characterization, and novel material synthesis techniques. By focusing on the underlying thermodynamic and kinetic limitations of storage materials, we will generate foundational understanding that will accelerate the development of all types of advanced storage materials, including sorbents, metal hydrides, and liquid carriers.

RESULTS

Task 1: Sorbents

Issues for Accurate Isosteric Heat Determinations

During FY 2019, there was significant effort looking at issues that could affect the accuracy in determining isosteric heats (Q_{st}) from isotherm data. This was a follow-on consequence of the FY 2018 milestone effort to test and verify the variable-temperature cryo-PCT system by determining Q_{st} for a material, and in that process, several issues were recognized that could potentially impact the accuracy of Q_{st} determinations. The following table provides an overview of these issues and their current status.

Issues Concerning Isosteric Heat Determination

Green indicates good progress has been made, yellow still has significant effort and additional resources needed, and red indicates little progress and additional resources needed.

Label	Issue	Status/Comments
Experimental		
Adequate isotherm data collection	To maintain accuracy, how much isotherm data should be collected (especially at low pressure)?	Need adequate resolution and enough data for isotherm equation fit; exact sensitivity in progress.
Sensitivity analysis to calibration errors	What is the influence of calibration errors on Q_{st} determination?	General trends are understood. Additional work in progress.
Analysis		
Fitting/interpolation	How does isotherm equation choice for fitting affect Q_{st} accuracy?	High sensitivity to isotherm choice; analysis still continuing.
Best isotherm data fitting	What is the best fitting equation to use?	Somewhat unresolved; Toth equation seems OK.
Excess vs. absolute capacity	Raw data is excess capacity; Q_{st} calculations need absolute capacity. What is the best way to convert and how does this affect accuracy?	Absolute gives more intuitive results. How best to convert has limited choices and is unresolved.
Appropriate Q_{st} equation model	Conventional Q_{st} equation has assumptions; how valid are they and what errors do they introduce?	Partially unresolved; needs significant resources to develop modeling approach.
High pressure effects (supercritical region)	Conventional Q_{st} equation not valid in supercritical region; how should it be calculated correctly?	Unresolved; needs significant resources to develop modeling approach.
Q_{st} calculation protocol	What is the best protocol to calculate Q_{st}?	Explicit T generally adds too much bias. Linear fit Ln(P) vs. 1/T seems to provide robust results.
Temperature effects and T-dependence assumptions	Explicit T-dependence in isotherm equations can introduce bias in Q_{st}; how are these terms justified from thermodynamic or kinetic considerations?	Partially resolved; specific examples have been understood, but not completely.
Heterogenous adsorption sites	Real materials have different types of adsorption sites; what is the best way to capture this in the fit and how does this affect Q_{st}?	Partially resolved; specific examples have been understood, but can this be generalized?
Determining equilibrium constant, K(T)	van't Hoff analysis requires K(T); most of the same issues above apply to K(T) determination.	Only resolved as so far as the above have been resolved.
Validity of van't Hoff	Thermodynamics vs kinetics effects. How do kinetic effects bias thermodynamic calculations?	Unresolved; not much effort available for this right now.

Figure 1 is an example of the issue of excess versus absolute isotherms in determining Q_{st} values and shows that using absolute isotherms provides the intuitively satisfying consistency that Q_{st} should decrease with increasing coverage. This data was taken for a real activated carbon and then processed in different ways and illustrates that several Q_{st} issues are being considered necessarily at once. For instance, the data had to be fit with an isotherm equation (Sips equation with or without a term to represent the excess subtraction so the conversion to absolute could occur) and then the Q_{st} calculation was performed either pairwise isotherm or four-wise for a linear fit.

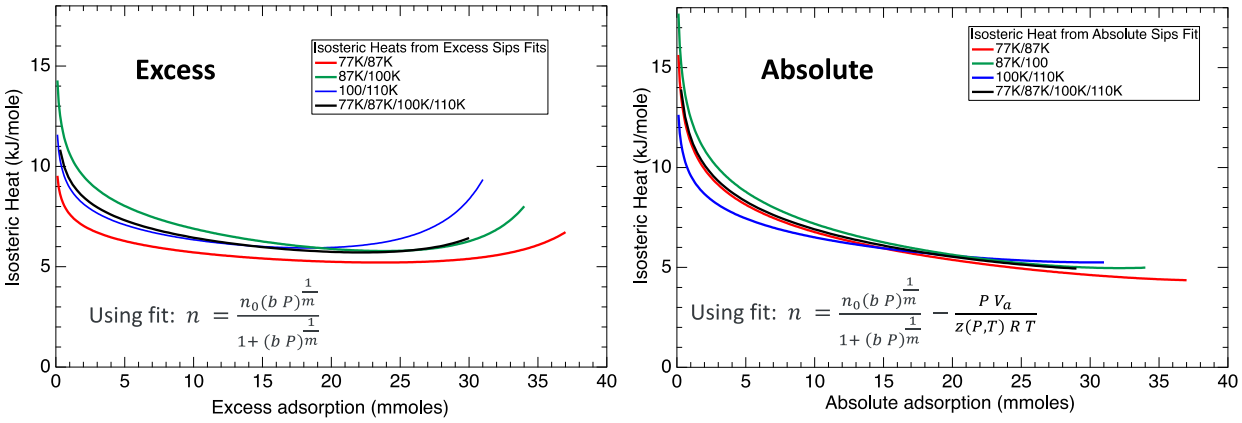

Figure 1. Comparison between Q_{st} using either the excess fit data or the excess fit data converted to absolute. In both cases, the isotherm has a Sips factor. Q_{st} is also calculated either using pairwise temperatures or with four temperatures and a linear fit of Ln(P) vs. 1/T.

Synthetic Routes to Dense MOF Monoliths

System volumetric capacity is an important technical target and most storage materials are underachievers. Powdered sorbents, for example, do not back efficiently and typically store only ~50 vol % H_2. Recently, Professor David Fairen-Jimenez at University of Cambridge reported a new solgel approach in which a MOF monolith with density nearly the same as the crystallographic value was synthesized [1]. We sought to demonstrate that this approach could be extended to other MOFs. In collaboration with LBNL (Jeff Long and Hiroyasu Furukawa) and Professor Fairen-Jimenez, we synthesized and measured hydrogen uptake for four zirconium-containing MOFs: UiO-66-BDC, UiO-66-NDC (1,4-napthalenedicarboxylate), and UiO-67-BPDC (biphenyldicarboxylate). These materials are representative of a large category of MOFs with potential for efficient, tailorable gas uptake. We optimized the solgel conditions and performed helium pycnometry measurements at LBNL to determine the specific volume of these materials. Hydrogen isotherms were obtained at 77 K and volumetric hydrogen uptake capacities for the powder and monolithic forms of UiO-66 (BDC) and UiO-66 (1,4-NDC) were compared. In both cases, a significant increase in the volumetric hydrogen uptake for was observed for the monolith relative to the powder form of the MOF materials. For example, the volumetric H_2 uptake by the UiO-67-BPDC monolith was ~55% higher than for the MOF powder (Figure 2). These results are extremely promising, suggesting that a critical limitation of powdered sorbents can be circumvented.

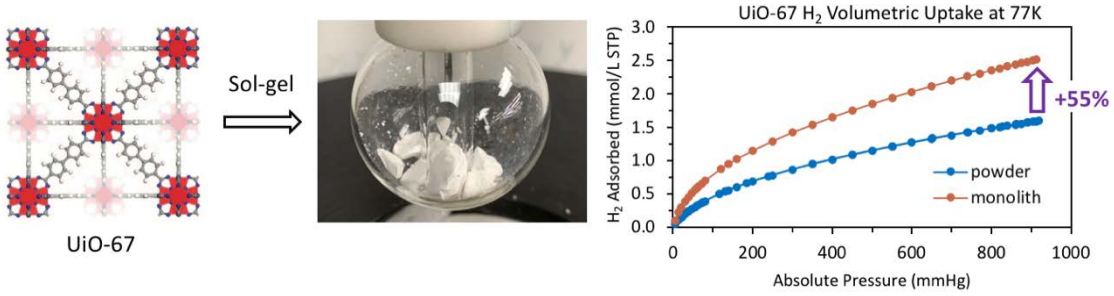

Figure 2. Left: ball and stick structure of UiO-67 (black spheres: carbon; blue: oxygen; red: Zr_6 cluster). Middle: UiO-67 monolith following solvent removal. Right: H_2 adsorption isotherms.

Frameworks with Optimal Binding Energies for H_2

π-backdonation plays a primary role in strong H_2 binding, and thus we predicted that MOFs bearing unsaturated V(II) and Cu(I) could yield enthalpies appropriate for room-temperature hydrogen storage between 5 and 100 bar. Last year, we successfully synthesized the framework $V_2Cl_{2.8}$(btdd), which features open V(II) sites (see Figure 3). In this reporting period, we characterized this material using the DRIFTS method at LBNL

(Figure 4). Through isotopic substitution studies, we unambiguously assigned a ν(H–H) stretch at 3,920 cm^{-1} to hydrogen bound at the open metal sites in our material. Notably, this is the lowest energy observed for H_2 bound at an open M^{2+} site and is higher than the frequency determined for H_2 bound at Cu(I) sites in Cu(I)-MFU-4*l* ($Zn_{(5-x)}Cu_xCl_{(4-x)}(btdd)_3$;[1] ν(H–H) = 3,252 cm^{-1}). This result supports our hypothesis that hydrogen adsorption occurs via a mechanism involving substantial backbonding from the vanadium sites, while smaller backbonding is involved relative to the copper(I)–H_2 interaction in Cu(I)-MFU-4*l*. Variable-temperature DRIFTS studies enabled us to determine enthalpy and entropy values for H_2 bound at the vanadium(II) sites. We determined a $-\Delta H_{ads}$ value of 21 kJ/mol, while the $-\Delta S_{ads}$ value was lower in magnitude than predicted, likely due to a different experimental contribution from the backbonding mechanism.

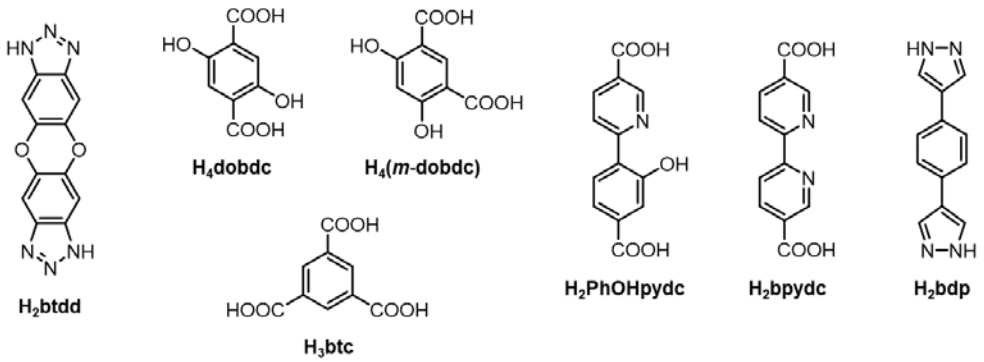

Figure 3. Structure of organic linkers used in this study

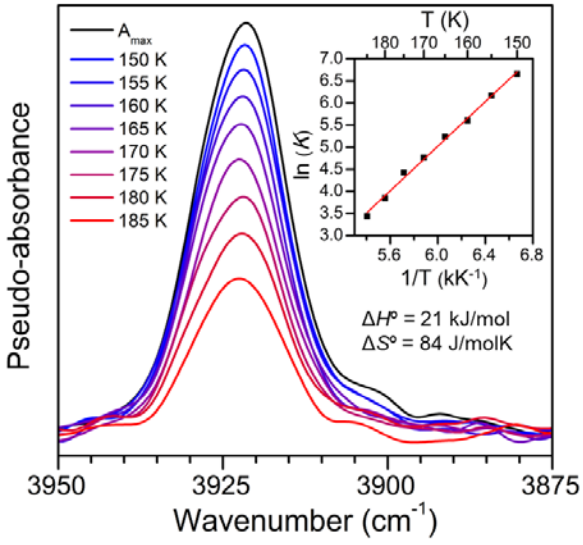

Figure 4. Variable-temperature difference spectra obtained by subtracting the IR spectra of H_2 adsorbed in $V_2Cl_{2.8}$(btdd) from the spectra obtained under equivalent dosings of D_2. Inset: van't Hoff plot used to determine thermodynamic parameters.

We have also previously reported VT-DRIFTS data for Cu(I)-MFU-4*l*, which binds H_2 more strongly than any other MOF, although the experimental $-\Delta H_{ads}$ = 33.6 kJ/mol is outside of the optimal enthalpy range of 15–25 kJ/mol for ambient temperature storage. High-pressure H_2 adsorption measurements were performed between 0–105 bar at 273, 298, 323, and 348 K to determine the usable capacities accessible for this framework (Figure 5). Total capacities corresponding to 1 H_2/Cu are reached at relatively low pressures, indicating that a sizeable fraction of the open copper sites would not contribute to usable capacity. As shown in Table 2, the usable volumetric capacity of Cu(I)-MFU-4*l* is smaller than that for Ni_2(*m*-dobdc) at 298 K. This difference is partly a function of the excessive binding enthalpy for Cu(I)-MFU-4*l* and also is reflective of the substantially lower density of open metal sites present in the latter material (approximately $1/8^{th}$ by volume compared to Ni_2(*m*-

dobdc)). As the storage temperature is increased, a larger percentage of Cu(I) sites bind H_2 and contribute to usable capacity. As a result, the volumetric usable capacity of Cu(I)-MFU-4*l* surpasses that of Ni_2(*m*-dobdc) at 348 K. Owing to lower density of the former material, its gravimetric usable capacity is superior to that of Ni_2(*m*-dobdc) at all measured temperatures.

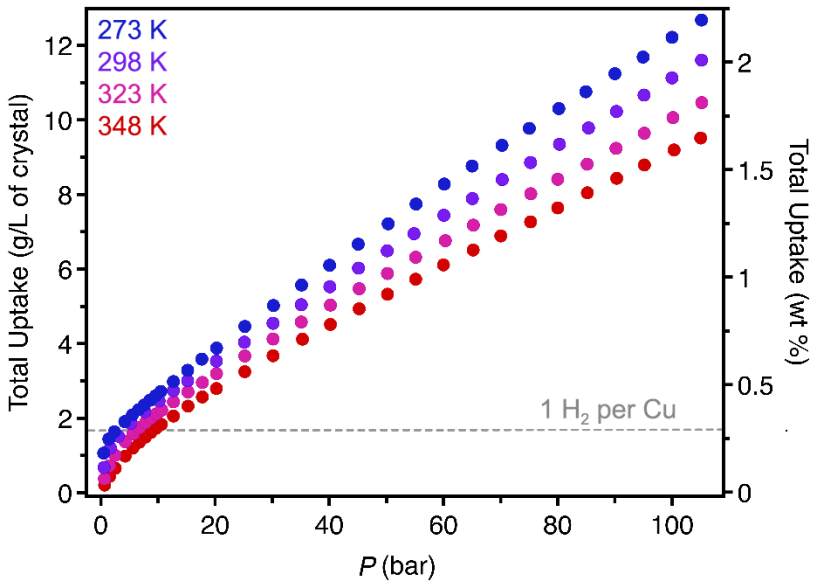

Figure 5. High-pressure H_2 adsorption isotherms for Cu(I)-MFU-4*l*. The crystallographic density was used to calculate volumetric uptake.

Table 2. Usable Capacities (5–100 bar) for Adsorptive Storage Using Cu(I)-MFU-4*l* and Ni_2(*m*-dobdc) Compared to Capacities Accessible with Compressed Hydrogen Using Tank under Otherwise Identical Conditions

Temperature	273 K	298 K	323 K	348 K
Compressed H_2 (g/L)	7.9	7.3	6.7	6.3
Cu^I-MFU-4*l* (g/L crystal)	10.2	9.3	8.6	8.1
Ni_2(*m*-dobdc) (g/L crystal)	14.1	11.0	9.3	7.9
Cu^I-MFU-4*l* (wt %)	1.8	1.6	1.5	1.4
Ni_2(*m*-dobdc) (wt %)	1.1	0.9	0.8	0.7

Multi-H_2 Binding in Frameworks

To enhance storage capacity, we also targeted MOFs with coordinatively unsaturated metal sites capable of binding multiple H_2 molecules per metal. Specifically, we prepared derivatives of the framework UiO-67 ($Zr_6O_4(OH)_4(bpdc)_6$, H_2bpdc = biphenyldicarboxylic acid) containing modified linkers featuring free pyridine and phenol groups (UiO-67-PhOHpydc, H_2PhOHpydc = 6-(4-carboxy-2-hydroxyphenyl)nicotinic acid; or bipyridine (UiO-67-bpydc, H_2bpydc = 2,2′-bipyridine-5,5′-dicarboxylic acid). We achieved quantitative metalation (based on inductively-coupled plasma–optical emission spectrometry analysis) of the pyridine-phenoxide sites in UiO-67-PhOHpydc, a long-standing challenge toward obtaining target materials with a high density of open metal sites. Metalation was achieved via gas-phase reactions with volatile reagents (e.g., copper amidinates) as well as solution reactions with copper acetate. However, activation of $Zr_6O_4(OH)_4(PhOpydc)_6Cu_6$ at elevated temperatures in vacuo did not yield coordinatively unsaturated Cu(I) sites for strong H_2 binding. ^{1}H-NMR spectra for digested $Zr_6O_4(OH)_4(PhOpydc)_6Cu_6$ revealed the presence of residual solvent and protonated ligands from metal precursors, which most likely block the Cu(I) sites. To prevent solvent coordination, we instead used $[Mn(CO)_5Br]$ and $[Re(CO)_5Cl]$ to metalate the free binding sites in UiO-67-bpydc [2]. Following coordination to the framework, photolysis with UV light or thermal treatment can be used to liberate the CO ligands, creating multiple open coordination sites. Using these metal carbonyls, we again achieved quantitative metalation of UiO-67-PhOHpydc and UiO-67-bpydc without loss of framework crystallinity or porosity. We are currently evaluating optimal methods for decarbonylation using photolysis and thermal treatment.

Flexible MOF Materials Development

MOFs with sharp step-shaped gas adsorption profiles can offer greatly improved usable capacities (as well as intrinsic heat management) relative to frameworks exhibiting Type I adsorption [3]. Step-shaped adsorption isotherms are often observed for flexible MOFs that undergo adsorption-induced structural phase changes upon gas adsorption, such as the framework Co(bdp) (H_2bdp = 1,4-benzenedipyrazole, Figure 3), which transitions to an expanded state when exposed to increasing pressures of methane [3]. A subsequent study of the frameworks Co(F-bdp), Co(*p*-F_2-bdp), and Co(*o*-F_2-bdp) using methane as a probe gas revealed that fluorine functionalization results in a reduction of the isotherm step pressures [4]. We accordingly sought to determine whether similar phase transitions and variations in step pressure would occur in these materials upon H_2 adsorption. Hydrogen isotherms obtained for these materials at 77 K and below 1 bar revealed minimal uptake. This result is likely because the collapsed phase is stabilized through ligand π–π interactions a large driving force is required to induce a phase change to the expanded state. We are pursuing alternative functionalization of H_2bdp ligand to destabilize these interactions and facilitate the desired phase change.

MOF Monolith Synthesis

Another approach to improve volumetric storage capacity is to densify adsorbent materials in powder form, a strategy used recently to achieve enhanced methane uptake in HKUST-1 ($Cu_3(btc)_2$; H_3btc = benzenetricarboxylic acid, Figure 3) [5]. In this reporting period, we prepared HKUST-1 according to the published procedure to verify the reproducibility of the monolith synthesis. Briefly, H_3btc and copper nitrate ethanolic solutions were mixed and stirred for 10 min. The solvent mixture was centrifuged to recover a wet gel sample, which was slowly dried at room temperature. Powder X-ray diffraction confirmed the crystallinity and phase purity of the sample, and the surface area of the monolith was estimated to be 1,750 m^2/g, slightly lower than the powder form of HKUST-1 (2,150 m^2/g). The density of the monolith (1.01 g/cm^3 by the Archimedean immersion method) is slightly higher than the single crystal density of HKUST-1 (0.88 g/cm^3). We performed low- and high-pressure adsorption measurements at cryogenic and ambient temperatures to evaluate the hydrogen storage capacity of this material (Figure 6). The total volumetric uptake for the HKUST-1 monolith was found to be greater than bulk density of H_2 under all our measurement conditions. More importantly, the total uptake in a monolith sample at 100 bar and 298 K is twice that of powder sample packed by hand (density of 0.43 g/cm^3) [6]. Detailed characterization of the monolith samples and expansion of this strategy to other MOF materials are in progress.

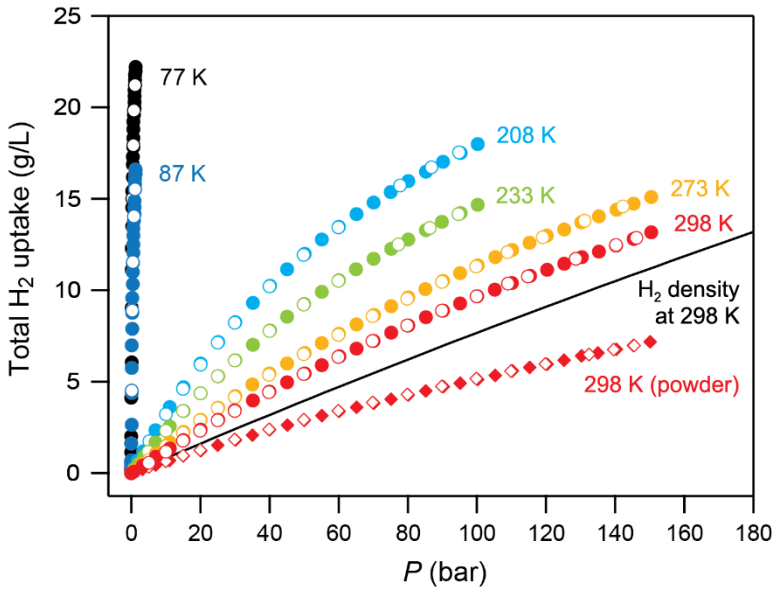

Figure 6. Total H_2 adsorption isotherms for the HKUST-1 monolith at 77, 87, 208, 233, 273, and 298 K (black, dark blue, light blue, green, orange, and red circles, respectively) shown alongside the total H_2 isotherm for HKUST-1 powder at 298 K (red diamonds). Filled and open symbols represent adsorption and desorption branches, respectively. The volumetric density of pure compressed H_2 at 298 K is also shown for reference (black line).

Evaluation of H_2 Adsorption Enthalpy and Entropy

Recently, we observed a very large temperature dependence of $\Delta H°$ and $\Delta S°$ upon H_2 adsorption in Cu(I)-MFU-4*l* by in situ DRIFTS and gas adsorption measurements. Our goal in this task was to understand the temperature dependence of these thermodynamic parameters through the study of the H_2 binding behavior in various materials under high pressures and ambient temperatures to better inform the design of novel materials.

DRIFTS Studies of H_2 Sorbent Materials

Variable-temperature FT-IR spectroscopy was performed on samples of Ca- and Mg-exchanged zeolite A (Figure 7). These materials feature open Ca and Mg sites, target metals of significant interest due to their highly polarizing nature. Upon H_2 dosing in both systems, a metal-dependent peak appears at 4,070 cm^{-1} for Mg zeolite A and 4,100 cm^{-1} for Ca zeolite A. Notably, the degree of bathochromic shift for Mg zeolite A is greater than that for Mg_2(dobdc), suggesting that the Mg ion occupies a more polarizing environment in the zeolite. Furthermore, the zeolites exhibit distinct broad peaks corresponding to secondary binding sites (4,114 and 4,125 cm^{-1} for Mg and Ca zeolite A, respectively), in contrast with the M_2(dobdc) and M_2(*m*-dobdc) framework series, which exhibit the same IR feature for secondary binding sites (at ~4,125 cm^{-1}) independent of metal identity. For zeolite A, these sites are attributed to Mg or Ca ions in differing coordination environments, although the possibility of a second, weaker H_2 adsorption site for the same ion cannot be ruled out. Efforts are ongoing to determine the thermodynamic parameters of these sites using VT FT-IR data, as well as to confirm the nature of the second site.

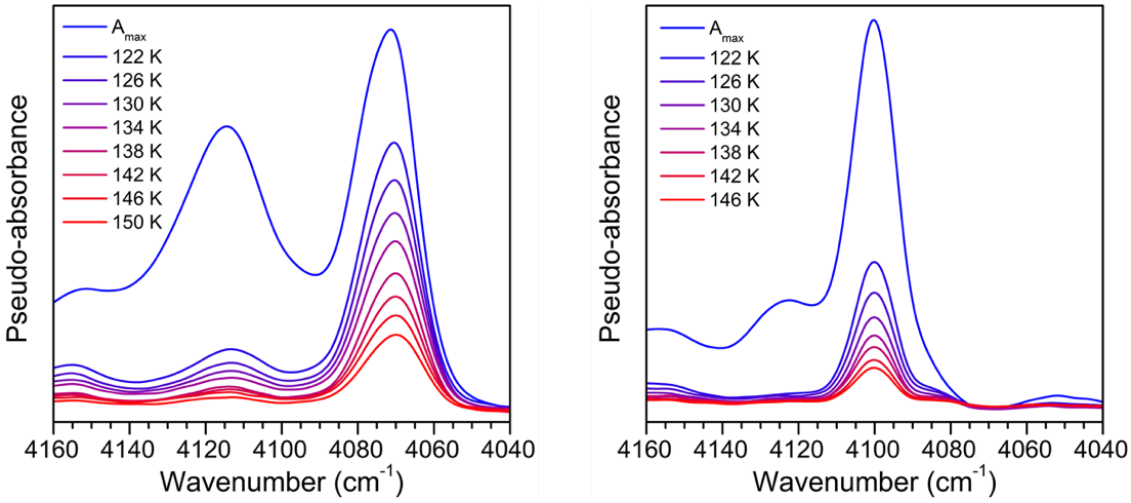

Figure 7. Variable-temperature FT-IR spectra of H_2 adsorbed in Mg- (left) and Ca-exchanged zeolite A (right)

Electronic Structure Computations for H_2 Storage

We used DFT to characterize binding sites in MOFs that show promise for enhancing usable H_2 capacities and to perform subsequent energy decomposition analysis. Following geometry optimizations of cluster models of the bare and bound hydrogen nodes, a systematic delineation of binding effects was performed, which allowed a separation of binding energy into contributions from frozen (includes dispersion), polarization, and charge transfer. Table 3 shows the energy decomposition analysis for hydrogen binding to two framework materials containing open Cu(I) and V(II) sites. A comparison of net contributions due to forward- and back-bonding revealed that back-bonding is dominant for Cu(I)-MOF, a conclusion reflected experimentally in the larger redshift of the ν(H–H) stretch for H_2 bound at open metal sites in Cu(I)-MFU-4*l* relative to $V_2Cl_{2.8}$(btdd) (see "Frameworks with Optimal Binding Energies for H_2"). This energy decomposition analysis may be leveraged for proposing binding motifs that increase material usable capacities. Potential energy surface of the copper scorpionate MOF Cu(I)-MFU-4*l* showed signatures of activated hydrogen adsorption via physisorbed precursors. Stationary point characterization along the molecular potential energy surface offered insight into the energy landscape for activated hydrogen adsorption that complemented structural information obtained from X-ray crystallography.

Table 3. Energy Contributions and IR Redshifts for Molecular Hydrogen Binding to MOFs Containing Open Cu(I) and V(II) Sites, Obtained Using the ωB97M-V Functional

The Cu(I) MOF shows significant contribution from back-bonding, which is reflected in a larger redshift of the *ν*(H–H) stretch.

Contribution (kJ/mol)	Cu(I)	V(II)
Frozen	38.5	11.4
Polarized	−44.5	−3.8
Charge Transfer	−46.1	−34.1
Δ*E*	−34.2	−26.9
Δ*E* forward	47%	81%
Δ*E* back	53%	19%
IR redshift (cm^{-1})	905	253

Benchmarking Density Functionals for H_2 Storage

We assessed the performance of different density functionals by comparing their predictions against highly accurate benchmark numbers from coupled cluster theory. The importance of core-valence contribution to the binding energies was identified and incorporated into the reference coupled cluster binding energies at the MP2 level of theory. Figure 8 shows the performance of ~50 density functionals along with reference benchmarks and results from commonly used and best-performing functionals. GAM, B97M-V, and B97M-rV were identified as inexpensive but accurate density functionals that can be used for high throughput screening purposes. The addition of an empirical dispersion correction (D3) was also found to improve the performance of the parent density functional only when the parent functional systematically predicts lower binding energies than the reference. In the future, we will write this work up in the form of a scientific publication.

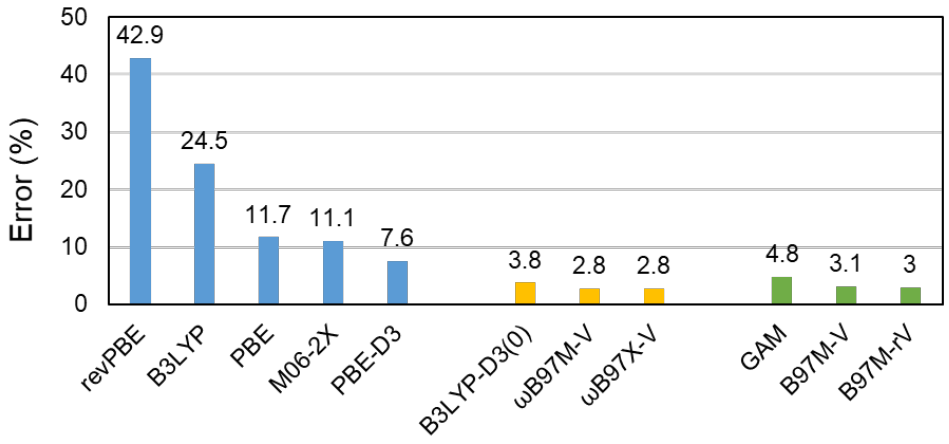

Figure 8. Performance of commonly used density functionals (blue), best performing functionals (yellow), and inexpensive best-performing functionals

Task 2: Hydrides

Phase Evolution of Lithium Amide during Dehydrogenation/Rehydrogenation

When metal hydrides are dehydrogenated or rehydrogenated, new solid-state phases are formed. Understanding the identity, microstructure, and rate of formation of these phases is critical for determining the rate-limiting step in each reaction and for developing effective computational models for simulating their chemistry. Lithium amide mixed with lithium hydride ($LiNH_2 + 2LiH$) is an attractive storage material because of its relatively high gravimetric density (10.3 wt % theoretical capacity). Probing internal interfaces in metal hydrides is difficult; transmission electron microscopy is ineffective because the materials are beam-sensitive.

We employed scanning transmission X-ray microscopy (STXM) to observe the composition, phase, and microstructure of partially dehydrogenated or rehydrogenated $LiNH_2$/LiH samples. Access to this instrumentation, which requires a synchrotron, was provided by the HyMARC approved program at the LBNL Advanced Light Source. The spatial resolution achievable is ~30 nm, which is sufficient to detect the presence of $LiNH_2$ and its decomposition products Li_2NH and Li_3N. STXM images in Figure 9 reveal the surprising result that partially dehydrogenated particles consist of a Li_3N core surrounded by a shell of Li_2NH. This conflicts with the conventional paradigm, which assumes that reactions at or near the particle surface leading to H_2 desorption are fast and that the rate-limiting step is a reaction that releases hydrogen into the bulk or in which released hydrogen diffuses to the surface.

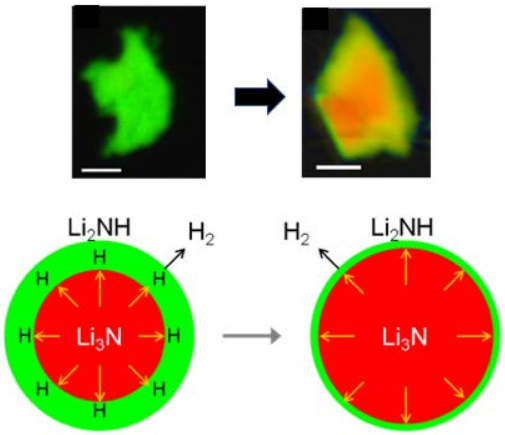

Figure 9. Top: STXM phase maps of $LiNH_2$ + 2 LiH dehydrogenated into static vacuum at 250°C (left) and into dynamic vacuum at 450°C (right). Red: Li_3N; green: Li_2NH. No significant amount of $LiNH_2$ was detected. Scale bar is 1 µm. Bottom: phase evolution schematic of particle dehydrogenation. The arrows indicate the direction of both the propagation of the growing phase and the flux of bound and gaseous hydrogen, with the black arrows representing the proposed rate-limiting step.

Metal Borohydride Eutectics

We determined that mixtures of $LiBH_4$ and $Mg(BH_4)_2$ partially decompose to form $[B_{10}H_{10}]^{2-}$ and $[B_{12}H_{12}]^{2-}$ species unless 350 to 1,000 bar H_2 back-pressure is used to suppress hydrogen desorption. In FY 2019, we established the infrastructure to experimentally probe the formation of metal borohydride eutectics by coupling a new Setaram calorimeter with a PCTPro instrument. In preliminary experiments, we probed the melting of pure $Mg(BH_4)_2$ under high hydrogen back-pressure. The heat flow measurements on the calorimeter showed an endothermic peak onset at 368°C, reaching its maximum at 375°C, and offset at 389°C, before a strong endothermic signal started at 392°C. The latter signal corresponds to substantial decomposition of the borohydride, whereas the peak at 375°C corresponds to $Mg(BH_4)_2$ melting. The integrated heat flow corresponds to an enthalpy of fusion of about 1.2 $kJ \cdot mol^{-1}$, consistent with previously reported values for metal borohydride melting.

Molecular Dynamics Modeling Framework for Metal Borohydrides

Borohydrides are attractive storage candidates because of their high gravimetric capacity. However, the chemical reactions occurring during dehydrogenation and rehydrogenation are complex and involve numerous molecule-like boron clusters such as $B_{12}H_{12}^{2-}$. Molecular dynamics is a computational tool that can predict the dynamics of the formation of these species, but it requires a force field (i.e., a mathematical description of the interactions between species based on Newton's laws). Developing and optimizing force fields, particularly ones that must account for a large number of molecule-molecule interactions, is extremely time consuming. Consequently, approaches to simplify this process are needed. We developed a method in which the intermolecular potentials are first predicted by DFT. Using these potentials, the phase interaction energies can be predicted by molecular dynamics. This year we focused on developing a force field for $Mg(BH_4)_2$, which has one of the highest gravimetric hydrogen capacities known (14.9 wt %). We computed interaction energies

for more than 700 bimolecular configurations of H_2, Mg^{2+}, MgH_2, BH_4^-, and $B_{12}H_{12}^{2-}$. We also completed the parameterization of 10 of the 15 molecule-molecule interaction force fields. Currently, we are implementing the force field in the LAMMPS molecular dynamics code, which was developed by Sandia, and will begin using it to predict reaction pathways for $Mg(BH_4)_2$ during the next fiscal year.

Borohydride Eutectic Formation

A potential strategy for destabilizing complex hydrides is to form a eutectic from a mixture with another compound. We tested this concept for $Mg(BH_4)_2$ by synthesizing mixtures with $LiBH_4$ and probing their melting behavior using variable-temperature X-ray diffraction (XRD). Our results show that eutectic melting without borohydride decomposition occurs under a hydrogen back-pressure between 350 and 1,000 bar H_2. Under these conditions, melting as low as 200°C was observed, compared with melting points of 280°C and 360°C for pure lithium and magnesium borohydrides, respectively. At pressures at or below 200 bar H_2, decomposition occurs with formation of $B_{12}H_{12}$-containing intermediates. The result is encouraging in that it demonstrates borohydride eutectic melting is possible. However, because $LiBH_4$ has the lowest melting point of the alkali metal and alkaline earth borohydrides, alternative compositions involving non-borohydride hydrides must be considered to achieve an even lower melting point.

In Situ Surface Characterization of $Mg(BH_4)_2$

Chemical reactions involving hydrogen at or near the surface of complex hydrides such as $Mg(BH_4)_2$ are very poorly understood and in some cases may be rate limiting (see discussion of the $LiNH_2$ above). Consequently, we applied a powerful suite of surface analytical tools available at SNL to probe these reactions and demonstrated that they can be used to track hydrogen transport to the surface and its subsequent desorption during heating. Surface hydrogen and surface chemical composition were detected using low-energy ion scattering and direct recoil spectroscopy. X-ray photoelectron spectroscopy (XPS) was used to determine the composition and oxidation state of the near-surface region to a depth of ~5 nm. The results suggest that hydrogen at the top surface is immediately desorbed, but subsequent release is kinetically limited by an initiation step. Moreover, the concentration of boron-containing species is elevated at the point of peak H_2 desorption, but magnesium subsequently segregates to the surface. These observations, which may have implications for the reversibility of the desorption process, are now being used to develop models to predict hydrogen release.

"Molecular" $Mg(BH_4)_2$ Stabilized By a Non-Innocent Nanoporous host

We sought to extend to the limit the concept of destabilizing metal hydrides by nanoconfinement by confining $Mg(BH_4)_2$ in a "non-innocent" host that we hypothesized could bind this hydride in molecular form. Nanoscaling is one of the most promising strategies for improving metal hydride hydrogen release and uptake thermodynamics and kinetics [2]. Theory and some experimental data suggest that hydride particles must be reduced to sizes smaller than 2 nm to have a significant effect on their thermodynamic stability. Examples of nanoscale complex hydrides such as $Mg(BH_4)_2$ are sparse and there are no measurements of thermodynamic data to indicate whether nanoconfinement affects stabilization. Using a MOF functionalized with bipyridine groups to coordinate the $Mg(BH_4)_2$ groups, we showed that individual hydride formula units can be formed and stabilized within the porous host. This synthesis of a complex hydride in molecular form is unprecedented. Its hydrogen release properties are indeed dramatically improved with the onset of hydrogen release as low as 120°C, >100°C lower than bulk.

Benefits of Nanoscaling

Although nanoscaling can shift the thermodynamics and kinetics of metal hydrides to improve their properties, nanoporous hosts that are often used are dead volume with no storage capacity. In collaboration with PNNL, we showed that the effective capacity of a nanohydride can actually be higher than bulk. This is because the thermal conductivity of hosts such as nanoporous carbon is much than bulk, which increases the H_2 release rate substantially. Using a finite element model of an operational storage tank developed by the Hydrogen Storage Engineering Center of Excellence, combined with data we obtained for bulk and nano-Li_3N, we determined that the gravimetric capacity of 6-nm hydride particles is 40 wt % of the 2020 DOE target vs. 33 wt % for

bulk; similarly, the volumetric capacity is 62 vol % of the 2020 DOE target for nano-Li_3N and 55 vol % for bulk (Figure 10). These results indicate that the DOE technical targets should not be considered in isolation during the discovery and development phases of potential storage materials.

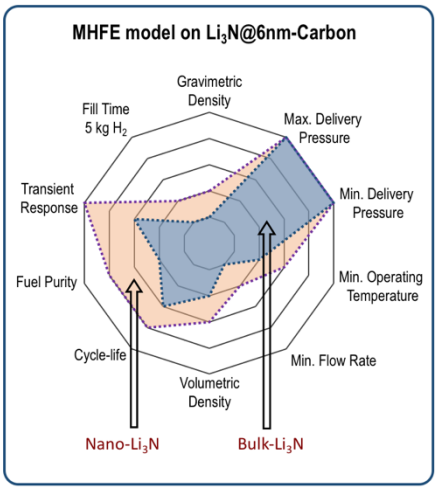

Figure 10. Comparison of bulk and nanoscale Li_3N properties vs. selected DOE technical targets. Rings correspond to (innermost to outermost) 20%, 40%, 60%, 80%, and 100% achievement of the target.

Explainable Machine Learning for Materials Discovery

Machine learning and data science approaches have potential to greatly accelerate discovery of new storage materials by revealing previously unsuspected relationships among material properties, thereby generating new scientific insight. This year we initiated a new effort to develop machine learning methods to accelerate discovery of new metal hydride storage materials. Although there are now several studies demonstrating the power of machine learning to identify sorbent materials with properties matched to DOE targets, this has not been explored for metal hydrides. We elected to use "explainable" methods rather than conventional "black box" classifiers because they are designed to identify material features that have the greatest influence on a particular material property and, thus, to generate new scientific insight. In our initial investigation, we employed the DOE Hydrogen Storage Materials Database of metal hydride properties (HYDPARK) [3]. Initial results of this investigation are shown in Figure 11. This database was cleaned to eliminate duplicate entries and compositions with missing thermodynamics data, resulting in a subset of 409 entries out of ~2,700 total. Although considerably smaller than the full set, this proved sufficient data to identify a strong correlation between the metal hydride equilibrium H_2 pressure and a volume-based descriptor ("mean_GSvolume_pa" in Figure 11) that can be computed using only the elemental composition of the intermetallic alloy. Remarkably, this simple structure-property correlation proved to be valid across a wide range of compositions and metal substitutions found in intermetallic hydrides, including A_2B, AB, AB_2, and AB_5 materials. Unfortunately, HYDPARK does not include enough complete entries for main-group hydrides to identify which features have the greatest influence on their equilibrium hydrogen pressure.

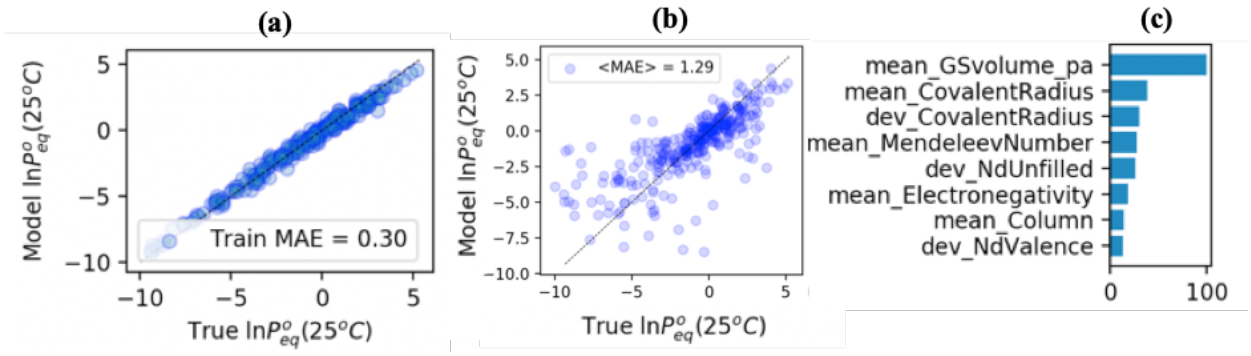

Figure 11. (a) Training set performance (MAE is the mean average error). (b) Performance of the model using the test data set. (c) Feature importance of the machine learning model for predicting equilibrium H_2 plateau pressure at standard temperature.

Morphology-Dependent Stability of Complex Metal Hydride Intermediates

Nucleation of complex metal hydride intermediate phases is one of the key factors limiting cycling kinetics. Accordingly, we developed a new approach to estimate the driving force for clustering, nucleation, and formation of solid phases by comparing the reaction energy landscape within three distinct *dimensionalities*—dispersed molecules (0D), clustered molecular chains (1D/2D, representative of interfacial or surface layers), and condensed-phase crystals (3D) [1]. Energies were obtained via an extensive search of atomic arrangements for Mg-B-H, Li-B-H, Na-B-H, Na-Al-H, Li-N-H systems at each dimensionality. Results are presented in Figure 12, which compares the energy gained upon proceeding from 0D to 1D/2D and on to 3D morphologies for all tested configurations. Configurations with large 0D-to-1D/2D energy differences have a strong driving force for clustering; those with large 1D/2D-to-3D energy differences have a strong driving force for crystallization and should nucleate easily. These values can generate approximate boundaries for likely expression of intermediates as crystalline phases, clusters, or dispersed molecules (marked with dashed lines in Figure 12, guided by X-ray diffraction observations of crystalline compounds where available). One feature of note is that although $Mg(BH_4)_2$ generally has a strong driving force for crystallization, there are a few select atomic configurations among we have tested that could favor 1D/2D morphologies. This could explain the formation of amorphous $Mg(BH_4)_2$ during cycling observed by Zavorotynska et al. [2] and indicates the possibility of stabilizing amorphous $Mg(BH_4)_2$ under certain processing and cycling conditions, presumably with improved nucleation/decomposition kinetics. Furthermore, our methodology provides an explanation as to why certain species in the Mg-B-H system (e.g., $Mg(B_3H_8)_2$, $MgB_{10}H_{10}$, and $MgB_{12}H_{12}$) are typically observed by nuclear magnetic resonance but not by X-ray diffraction, indicating a lack of long-ranged crystalline order.

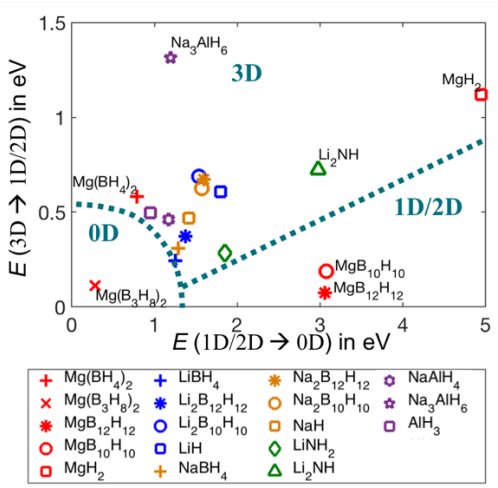

Figure 12. Morphology-dependent metastability map showing the relative driving forces for 1D/2D-to-3D and 0D-to-1D/2D interconversion. Possible boundaries for regions of the diagram corresponding to different favored morphologies are indicated with dotted lines. 1D/2D results are computed as averages of separate 1D and 2D results.

Advanced Modeling of Phase Nucleation Kinetics

Last year, we reported initial development of an advanced phase nucleation framework for directly computing the multi-step nucleation kinetics of crystalline intermediate phases (e.g., $MgB_2 \rightarrow MgB_{12}H_{12} \rightarrow Mg(BH_4)_2$). This year, we extended the model to examine nucleation pathways involving amorphous intermediates, which are often more relevant under realistic operating conditions. Specifically, we considered the formation of crystalline $Mg(BH_4)_2$ (C-$Mg(BH_4)_2$) by first nucleating amorphous $Mg(BH_4)_2$ or clusters (A-$Mg(BH_4)_2$). The associated energetics and driving forces were obtained from the morphology-dependent thermodynamics reported in Figure 12, with the energy of amorphous $Mg(BH_4)_2$ estimated from the energy difference between 3D and the 1D/2D morphologies. Figure 13 (upper panel) shows a parametric simulation study of the phase nucleation barriers as a function of particle size and hydrogen partial pressure for three different pathways: $MgB_2 \rightarrow$A-$Mg(BH_4)_2$, A-$Mg(BH_4)_2 \rightarrow$C-$Mg(BH_4)_2$, and $MgB_2 \rightarrow$C-$Mg(BH_4)_2$. The relative magnitudes of the barriers indicate three major trends. First, two-step nucleation via amorphous $Mg(BH_4)_2$ is preferred over direct nucleation of crystalline $Mg(BH_4)_2$ from MgB_2, suggesting chemical products condense before crystallizing. Second, all nucleation barriers vary with MgB_2 particle size, with the sensitivity dependent on the nucleation pathway. Third, there is a possible transition of the nucleation mechanism with increased hydrogen pressure (lower panel, Figure 13). In particular, at lower pressures, the barrier for the first step ($MgB_2 \rightarrow$A-$Mg(BH_4)_2$) is smaller than the second step (A-$Mg(BH_4)_2 \rightarrow$C-$Mg(BH_4)_2$), indicating that crystallization becomes relatively easier once the amorphous phase forms. On the other hand, at higher pressures, the barrier for the second step is higher than for the first step, which indicates formation of the amorphous phase without ever nucleating the crystalline phase. The work is a first step toward identifying synthesis and cycling conditions for formation of A-$Mg(BH_4)_2$, which could have kinetic advantages over C-$Mg(BH_4)_2$.

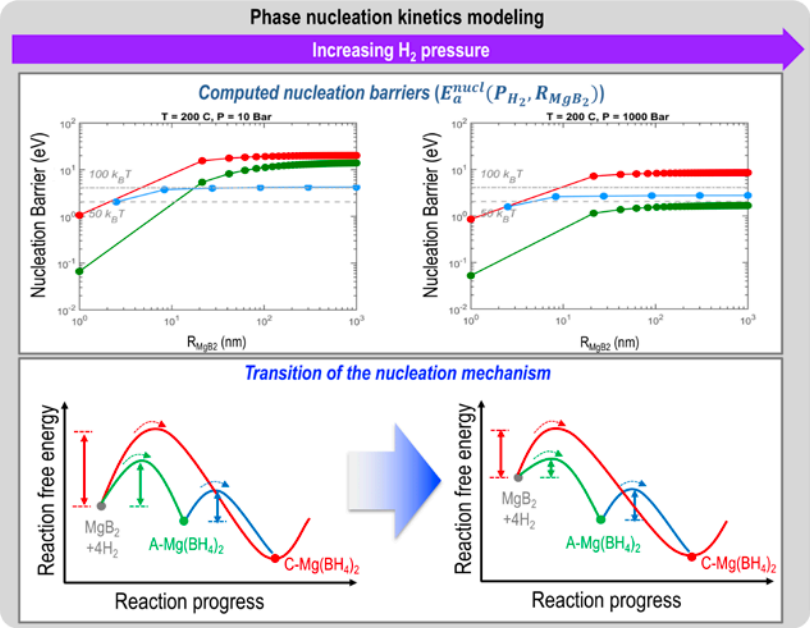

Figure 13. Advanced phase nucleation modeling: computed nucleation barriers for varying particle size and hydrogen partial pressure (upper panel: left = 10 bar, right = 1,000 bar); and possible transition of the nucleation mechanism (lower panel). Colored lines in the top panel correspond to the different possible reaction steps shown in the lower panel.

Mechanical Stress Effects on Thermodynamics

We previously identified mechanical stress as a promising avenue for favorably altering the thermodynamics of confined hydrides. This year, we further investigated its role by extending our previously developed model to account for two factors intended to introduce additional realism and accuracy: (i) realistic mechancial properties of host materials; and (ii) realistic mechanical boundary conditions for hydride-host composites. Experimentally, the composites can be synthesized in compact or loose forms (see Figure 14). Within the simulations, these conditions can be mapped onto two limiting cases of mechanical boundary conditions: (1) a completely constrained condition, corresponding to compact packing and high loading; and (2) a completely unconstrained condition, corresponding to loose packing and low loading (actual samples lie between these two cases). The corresponding enthalpy change from the characteristic strain energy (H_{el}^{char}) can therefore predict the thermodynamic effect of the clamping force exerted by the host during hydrogenation. In Figure 14b, we compare polycrystalline Mg-H encapsulated by carbon and alumina hosts (assuming only elastic deformation of Mg-H). As expected, the elastically stiffer alumina host induces more stored strain energy in the active material (Mg-H) as compared with the carbon host case. In addition, the alumna host gives rise to larger variability in the mechanical strain energy depending on the mechanical boundary condition for the composite, translating to higher sensitivity to packing and loading conditions.

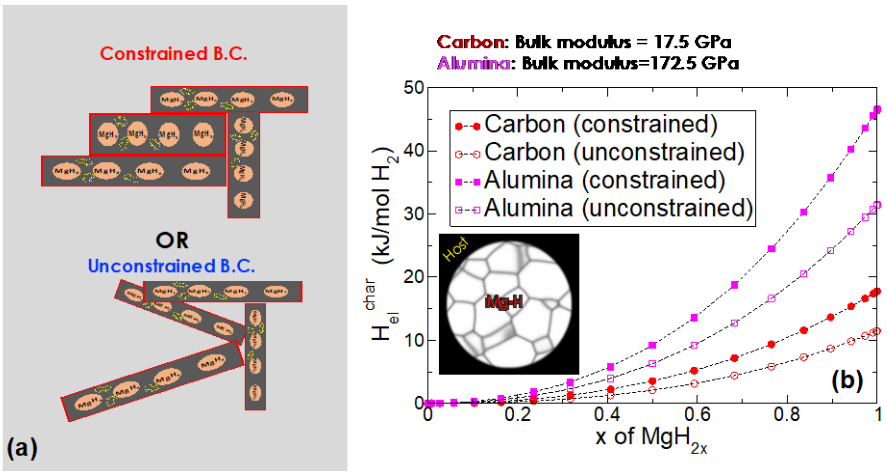

Figure 14. (a) Schematic of possible mechanical boundary conditions for host-active material composites. (b) Predicted mechanical strain energy under the two limiting boundary conditions in (a) for Mg-H encapsulated by two different host materials (assuming purely elastic deformation).

Integrated Mesoscale Model for Full Simulation of (De)hydrogenation

This year, we provided the first full demonstration of a mesoscale model that comprehensively includes all available temperature-sensitive parameters for chemical reaction, diffusion, stress, and phase transformations. This model allows us to simulate full (de)hydrogenation reactions for comparison to experiments and to explore which specific materials parameters could have the highest impact on overall kinetics. Palladium was chosen as a model demonstration system due to its chemical simplicity. Figure 15a shows simulated dehydrogenation of model polygranular PdH_x (with microstructure shown in the figure inset) at three different temperatures. As shown in the figure, we can monitor the temporal evolution of hydrogen content (see Figure 15a) within the storage medium as well as the co-evolving decomposition microstructure (see Figure 15b). Although further refinement and calibration are underway, this example demonstrates the utility of this model. By applying the kinetic analysis to simulated results, we are further able to extract the evolution of overall activation energy during the course of dehydrogenation, allowing us to examine the rate-limiting factors (Figure 15c).

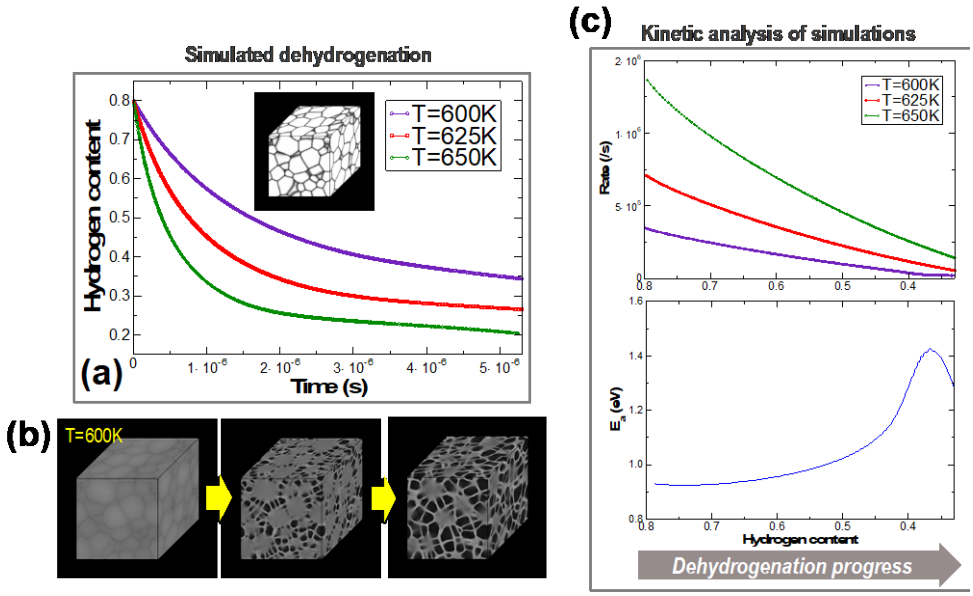

Figure 15. Full dehydrogenation simulations of PdH_x: (a) hydrogen content as a function of time monitored for three selected temperatures; (b) corresponding decomposition microstructure at a temperature of 600 K; and (c) kinetic analysis of the dehydrogenation simulations, showing the evolving overall activation energy with reaction progress.

Chemical Bond Activation in Borides and Borohydrides

We previously predicted that encapsulation of $Mg(BH_4)_2$ within a strongly interacting, "non-innocent" host material could help to activate sluggish B-H bonds for faster hydrogen release kinetics. This hypothesis relies on maintaining low dimensionality while suppressing entropy increases typically associated with surface degrees of freedom in non-interacting encapsulants. To this end, we initiated a joint experiment-theory study of $Mg(BH_4)_2$ confined within the MOF material UiO-67-bpy $(Zr_6(O)_4(OH)_4)(bpydc)_6)$. By comparing simulated and experimentally measured N K-edge X-ray absorption spectra, we confirmed that bipyridine N in the host are coordinated to Mg(II) to affect the Mg-BH_4 interactions. To evaluate the corresponding effect on hydrogen release kinetics in $Mg(BH_4)_2$, we computed the B-H dissociation energetics in bulk γ-$Mg(BH_4)_2$ versus $Mg(BH_4)_2$@UiO-67bpy. The dissociation energy in the latter case was found to be ~0.5 eV lower, which was supported by corresponding experimental thermogravimetric and Sieverts dehydrogenation measurements.

Rehydrogenation of MgB_2 has proven even more challenging, with limited reversibility only at extreme pressures. Our previous investigations suggested that the key to promoting B-B activation in MgB_2—and hence to reducing hydrogenation conditions—may lie in charge transfer to and from the extended boron sheets, which disturbs the pseudoaromatic stability. To further explore this phenomenon, we applied density functional theory calculations to isolated metal atoms adsorbed on an idealized MgB_2 surface. We found that metal atoms will interact electronically with the B plane to either induce charge transfer (ionic interaction with alkali metals or alkaline earth metals) or directly modify the B-B electronic bonding states (covalent interaction with open-shell transition metals). Notably, early transition metals generally contribute both ionic and covalent interactions (Figure 16a); we speculate that this flexibility makes them more effective for promoting hydrogenation because charge fluctuations around the B atoms can be more easily accommodated when hydrogen is adsorbed. As shown in Figure 16b, the saturation limit for hydrogenation of an MgB_2 surface prior to disrupting the B plane occurs at a surface B:H ratio of 2:3. This limit can be reached under milder conditions when atoms like Ti are added, translating to faster decomposition kinetics. Experimental validation of these effects is being conducted, along with further ab initio molecular dynamics simulations of direct MgB_2 hydrogenation. These activities satisfy one of our quarterly milestones to develop a computational approach to enable screening of additives to activate B-B bonds.

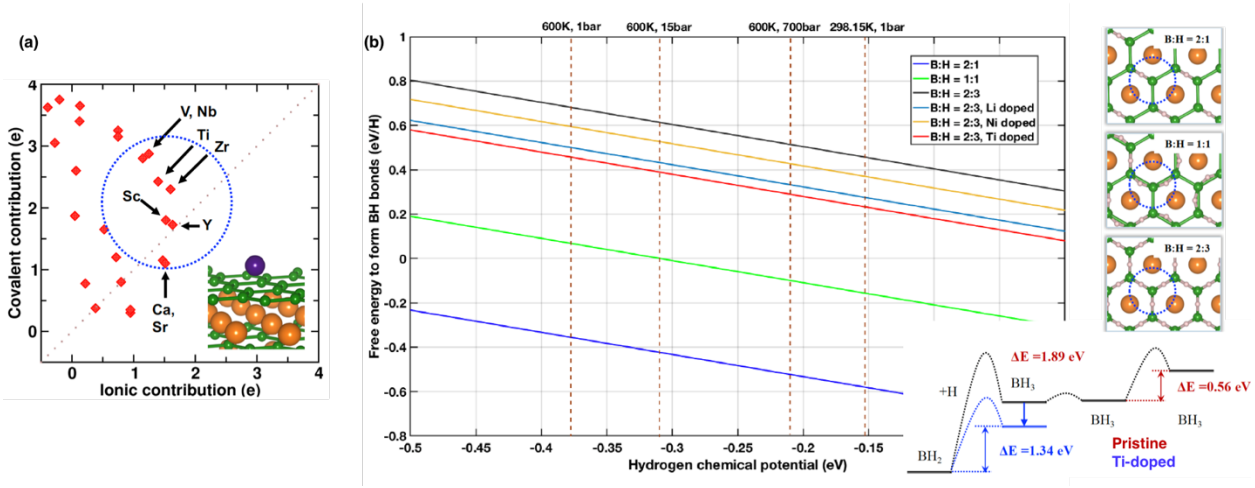

Figure 16. (a) Summary of ionic and covalent contribution of metal dopants on the MgB_2 surface. (b) Estimated Gibbs free energy for hydrogen absorption on the MgB_2 surface as a function of hydrogen chemical potential.

Demonstration of Multiple Cycles of H_2 Uptake and Release from Magnesium Borohydride, $Mg(BH_4)_2$

Previously we had observed a single cycle of H_2 uptake and release connecting $MgB_{10}H_{10}$ to $Mg(BH_4)_2$. In FY 2019 we measured reversible uptake of hydrogen through four cycles between magnesium borohydride and magnesium decaborane below 180°C, showing the possibility of multiple cycles.

(Reaction 2) $5Mg(BH_4)_2 \Leftrightarrow MgB_{10}H_{10} + 4MgH_2 + 11H_2$ 8.2 wt %

Validation that Variable Approaches Can be Used to Prepare the Precursor Complexes Leading to the Formation of an Adduct that Provides Reversible Release and Uptake of Hydrogen

We used a combination of XRD and NMR to demonstrate multiple pathways to prepare adducts of magnesium borohydride responsible for low temperature reversibility. Adducts were formed by mixing solid $Mg(BH_4)_2$ with the appropriate quantity of tetrahydrofuran (THF) or by adding the THF to an ether solution of $Mg(BH_4)_2$ and removing the ether under vacuum. The quantity of THF was determined using XRD, which showed different crystal structures for adducts containing different amounts of THF (Figure 16, left), and by comparing the intensities of proton NMR signals from THF and BH_4^-. Upon heating, the different BH_4^- environments in the solid collapsed into a single resonance when the compound underwent melting above 60°C (Figure 16, right).

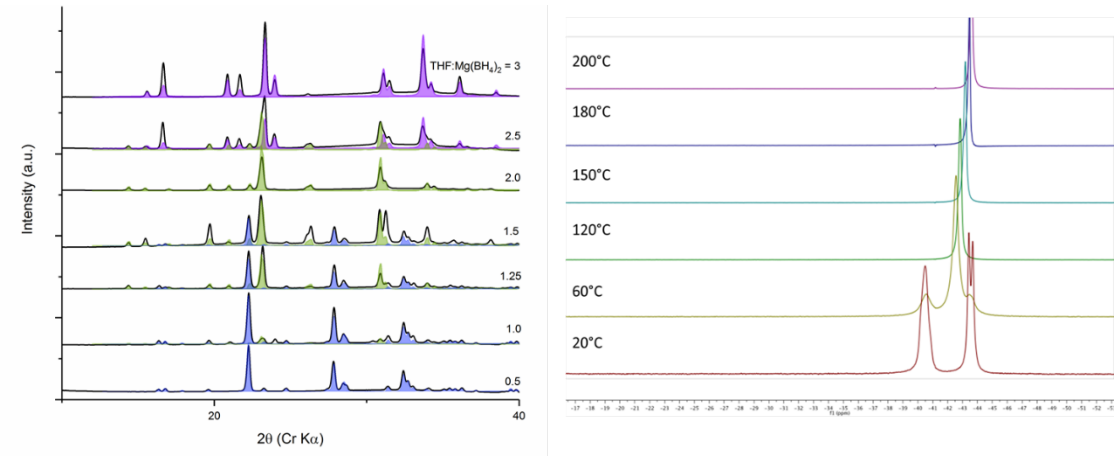

Figure 16. Left: XRD patterns of $Mg(BH_4)_2$ with different ratios of THF. The purple pattern corresponds to $Mg(BH_4)_2$·3THF, the green pattern to $Mg(BH_4)_2$·2THF, and the blue pattern to $Mg(BH_4)_2$·0.67THF. Right: In situ ^{11}B NMR spectra of $Mg(BH_4)_2$·2THF heated to 200°C.

Recommendations to Compare Intermediates Formed in the Release of H_2 from Borohydrides Using Different Additives

$Mg(BH_4)_2$ is a well-studied complex hydride. Several groups have suggested the addition of additives enhance the reactivity; however, it is difficult to compare one study to another as the approaches to identify and quantify intermediates vary from study to study. We used a combination of solid-state and solution-phase NMR to develop a recommended best practice for comparing different studies. Solid-state NMR provides an unadulterated comparison of the major intermediates, but the peaks can be broad and unresolved. To remedy this loss of features we showed that the analysis of the solution NMR in three different solvents provides more insight into the different products: (i) a mix of D_2O/THF dissolved most of the borane adducts but the sample is not stable for extended periods of time; (ii) acetonitrile provides an opportunity to observe reactive species such as $B_2H_7^-$ that are not stable in most solvents; and (iii) DMSO is the best solvent for BH_4^-. Figure 17 shows a comparison of the different products that can be observed in different solvents. Although D_2O/THF is the best "all-round" solvent, if only one solvent is used then there is a risk some species would not be identified.

Enhanced Low-Temperature Melt/Solidification Cyclability of $Mg(BH_4)_2$ via a Novel Additive, Tetramethylammonium Borohydride (TMAB)

Completely reversible melt/solidification was observed for five cycles of $Mg(BH_4)_2$:0.2TMAB, with a melting point of 185°±5°C. In situ XRD was used to verify melting, and ex situ XRD was used to verify return to fully crystalline material (no observable amorphous signal). The eutectic composition for this system giving the lowest melting point is being identified, and due to the nature of this system being a combination of borohydride salts, coupled with the XRD evidence, strongly suggest a eutectic melt at lower mass fraction of TMAB than the 25 wt % of TMAB in $Mg(BH_4)_2$:0.2TMAB. Preliminary results have shown that TMAB also effects the melt/solidification behavior of $Mg(BH_4)_2$:xTHF samples (Figure 18).

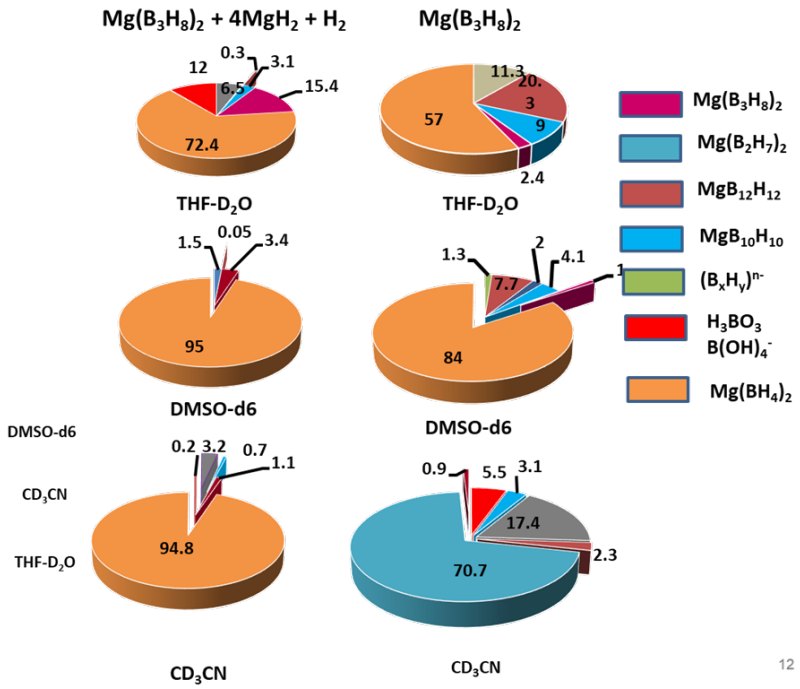

Figure 17. Comparison of boron species observed in ^{11}B NMR spectra of samples dissolved in different solvents. The sample compositions shown were heated under H_2 gas before dissolution.

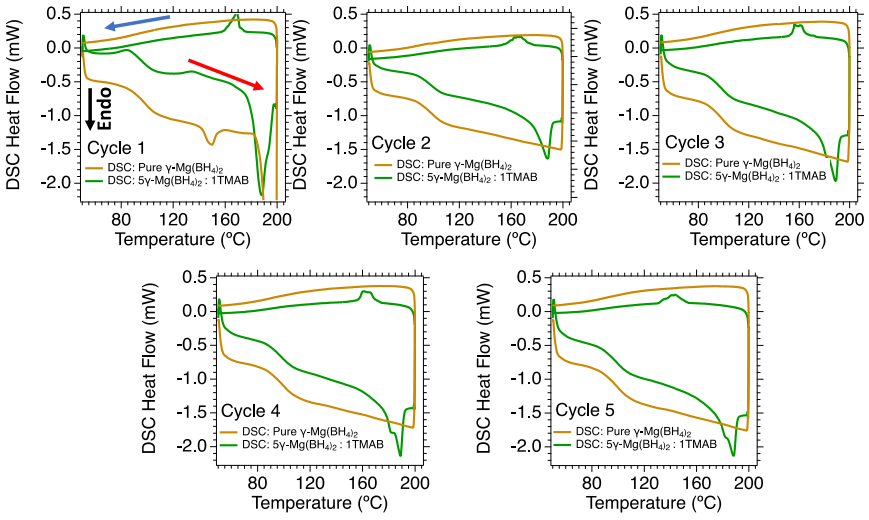

Figure 18. Differential scanning calorimetry (DSC) comparison of cycling pure γ-$Mg(BH_4)_2$ compared to a $Mg(BH_4)_2$:0.2TMAB blend. Heating ramp rates were 10°C/min and quench rates were 2.5°C/min. No cycled phase changes are observed for pure γ-$Mg(BH_4)_2$; however, the $Mg(BH_4)_2$:0.2TMAB blend exhibits endothermic melt events on heat up and exothermic re-solidifications during quench for all five cycles. The spikes and shifting temperature of the re-solidification event are consistent with a net off-eutectic stoichiometry quenched through a two-phase liquid/solid region where solid phases are repeatedly nucleated from the melt until the final solidification at the eutectic composition.

Nano-Confined Metal Hydrides under Mechanical stress

We used PCT to test the boron nitride coated magnesium for possible strain effects. The team selected the Mg-MgH_2 system for an encapsulation experiment designed to test metal hydrides under mechanical stress. The concept is to use atomic layer deposition (ALD) to coat magnesium powder with boron nitride. The material would then be hydrided using PCT. Formation of MgH_2 in the hydriding process would result in a volume expansion of the hydride where the rigid boron nitride coating could induce residual strain. PCT measurements of kinetics and thermodynamics would be performed to study cycling behavior.

Using a new ALD fluidized bed reactor, 20 g of Mg powder was coated with 25 ALD cycles of boron nitride at 225°C with air-free transfer. Figure 19a shows transmission electron microscopy (TEM) images after the ALD process where a possible ~10 nm film has been deposited on the powder.

Figure 19b shows the PCT (performed by H2Tech Consulting) results for a desorption-absorption-desorption cycle. Desorption 1 shows nominal release of hydrogen at 0.1 wt % at 220°C. This was also observed in temperature programmed desorption of the material (not shown) where the mass spectrum indicates hydrogen is the primary product. Absorption 1 shows hydrogen uptake at about 0.5 wt % by summing the amount absorbed at 220°C and 300°C. Desorption 2 shows weak desorption at 300°C. The cycling results are consistent with cycling of boron nitride coated $Mg(BH_4)_2$ where little absorption occurs. Recently, the ALD of boron nitride has been better characterized by the HyMARC seedling project to show a more complex material than simple BN. Additional bromine and oxygen have been detected and other efforts indicate that no crystalline boron nitride forms at these temperatures. It is possible that the complex ALD "boron nitride" material inhibits hydrogen uptake and the lack of a pure phase reduces its chance of high strength BN.

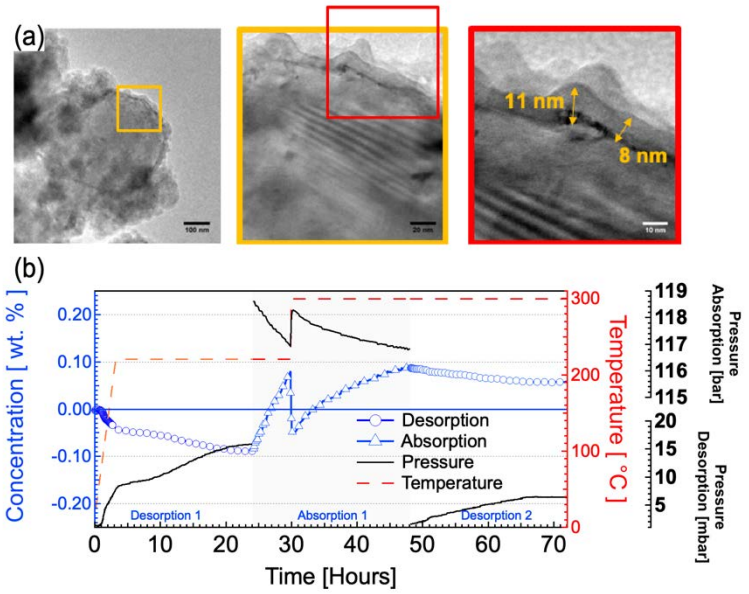

Figure 19. (a) TEM images of the boron nitride coated magnesium powder; (b) PCT data for the material after a desorption-absorption-desorption cycle

B-Bond Task—Physical Mixtures of Halides and $Mg(BH_4)_2$: Established as a No Go

With the goal to weaken the B-B bond, we studied the effect of physically mixing halides in borohydride materials on the H_2 storage performance of borohydrides. In this study, we investigated the materials mentioned in Table 4 with TPD, DSC, and H_2 desorption/adsorption cycles were performed using a PCT apparatus. The TPD results are summarized in Table 4. In all halide/borohydride mixtures, the onset desorption temperature was lowered, but the total H_2 capacity was substantially lowered compared to the neat material and H_2O or B_2H_6 were present.

Based on the TPD measurement, the temperature of 290°C was selected for H_2 desorption/adsorption cycles on the halide/$Mg(BH_4)_2$, but the cycling behavior was poor and far from the targets. Therefore, these efforts were discontinued for hydrogen onboard storage research.

Table 4. Overview of the Results Extracted from TPD

The gravimetric capacity is based on the signal normalized to the sample mass and a calibration of the H_2 signal that enables a quantification within 20% error (expressed with ±). If an impurity had a signal ≥10% of m/z=2, it was included in this table.

Material	Lowest desorption temperature (°C)	Gravimetric capacity (H_2 wt %)	Impurity, if present
$NaBH_4$	590	8.9 ± 1.8	
$NaBH_4$+$CaCl_2$	450	5.4 ± 1.1	H_2O
$Mg(BH_4)_2$	320	11 ± 2	B_2H_6
$Mg(BH_4)_2$+$CaCl_2$	180	5.2 ± 1	B_2H_6
$Mg(BH_4)_2$+$MgCl_2$	200	4.9 ± 1	B_2H_6

$Mg(B_3H_8)_2$—PNNL: Four triborane samples were measured with TPD: $Mg(B_3H_8)_2$ + 2NaBr, $Mg(B_3H_8)_2$ + 2NaBr + 4MgH_2, $Mg(B_3D_8)_2$ + 2NaBr, and $Mg(B_3D_8)_2$ + 2NaBr + 4MgH_2. The presence of MgH_2 seems to play a substantial role in the formation of undesired byproducts, such as B_2H_6 and B_5H_9 during the heat treatment. For more details, we refer to the manuscript that has recently been completed.

$Mg(BH_4)_2$*0.3THF—University of Hawaii: We performed TPD and TEM imaging of two samples synthesized at $Mg(BH_4)_2$*0.3THF neat and after 1 PCT cycle (performed at University of Hawaii at 180°C and 90 bar H_2). The most relevant results are summarized in Figure 20 and Table 5. In the as-synthesized samples, the H_2 liberation is low until a substantial portion of "excess" THF is released. Excess THF has an onset desorption temperature of T ~75°C and peaks at 134°C, and the rate of H_2 desorption (slope of m/z = 2 signal in Figure 20a) clearly increases from T >160°C. The TPD of $Mg(BH_4)_2$*0.3THF 1 PCT cycle, on the other hand, doesn't show any THF liberated above background level of the mass spectrometer, and the H_2 desorbs at a steady rate starting at T ~65°C and peaks at 120°C. These samples were held at 200°C over 12 hours and Table 5 shows that after this duration, the gravimetric H_2 released is very close for each sample. This indicates that the kinetics seem different for the two samples.

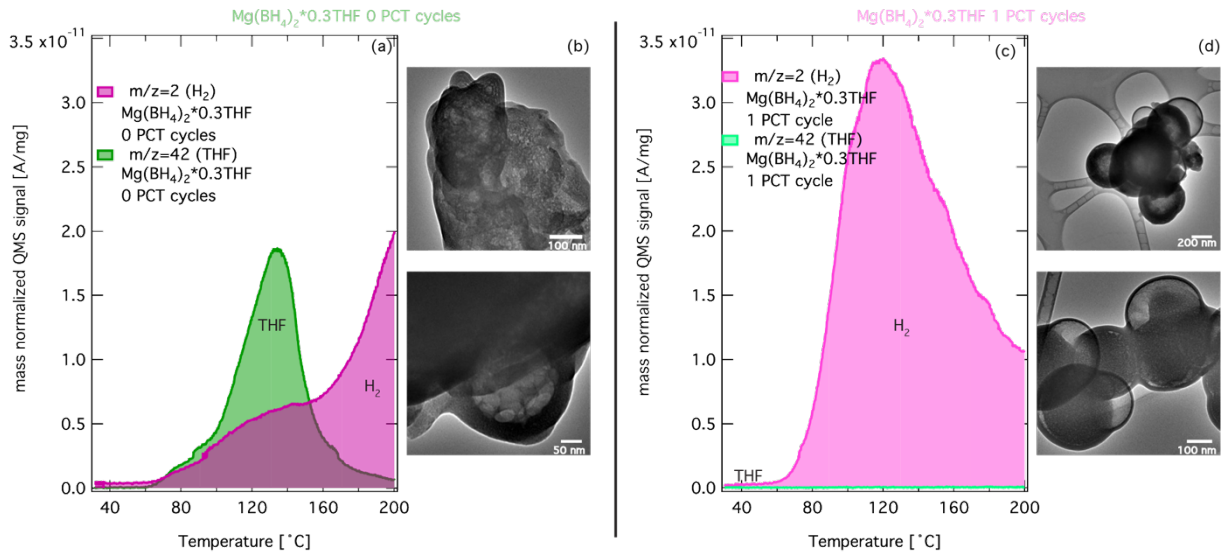

Figure 20. Mass normalized H_2 thermal evolution from TPD between 30°C and 200°C heated at 3°C/min of (a) the as-synthesized $Mg(BH_4)_2$*0.3THF and (c) $Mg(BH_4)_2$*0.3THF after 1 PCT cycle, with the respective TEM images of the samples after the TPD heat treatment to 200°C shown in (b) and (d).

The TEM images after TPD (only heated to 200°C, not held for 12 hours) shown in Figure 20b and Figure 20d give us further insight on a possible explanation for the good cyclability of the material: the THF treatment appears to trigger the formation of a shell, which may be dynamic enough to allow for the restructuring of the material when it is exposed to temperature and pressure (180°C and 90 bar H_2) from a shapeless agglomerate (Figure 20b) to spherical structures (Figure 20d).

Table 5. Overview of the Results Extracted from TPD for $Mg(BH_4)_2$*0.3THF Neat and After 1 PCT Cycle (over 1 hour and over 12 hours)

The gravimetric capacity is based on the signal normalized to the sample mass and a calibration of the H_2 signal that enables a quantification within 20% error (expressed with ±).

Sample	H_2 capacity 1 hour (once 200°C is reached)	H_2 capacity over 12 hours (at 200°C)
$Mg(BH_4)_2$*0.3THF	0.33 ± 0.07	0.83 ± 0.17
$Mg(BH_4)_2$*0.3THF 1 PCT cycle	0.71 ± 0.14	0.99 ± 0.2

Divalent Salt Additives

It was successfully determined that divalent salt additives can incorporate into $NaBH_4$, reducing the strength of B bonds within the system. Thermogravimetric analysis (TGA) shows that the decomposition temperature of $NaBH_4$ is significantly reduced by the salt additive, reducing the onset of weight loss from 400°C to as low as 100°C (Figure 21a). DSC finds that phase changes occur as low as 150°C, and Raman spectroscopy finds that the bending mode of B-H becomes less energetic with the additives, giving insight into how coordination of the salt occurs. Powder X-ray diffraction confirms that the additives expand the crystal lattice rather than forming new phases, with the most notable diffraction shifts occurring with the use of salts containing the larger I anion compared to Cl (Figure 21b). X-ray absorbance spectroscopy (XAS) suggests that the geometry of the metal of the salts as well as Na in $NaBH_4$ is not significantly altered when combined. However, it is clear from both XAS and X-ray photoelectron spectroscopy that the halogens have a notable influence on binding energies within the system, especially for B (Figure 21c). This work is improving the understanding of how exactly additives coordinate to $NaBH_4$, which will make future efforts in developing these mixed materials easier to target materials to improve H_2 release from $NaBH_4$.

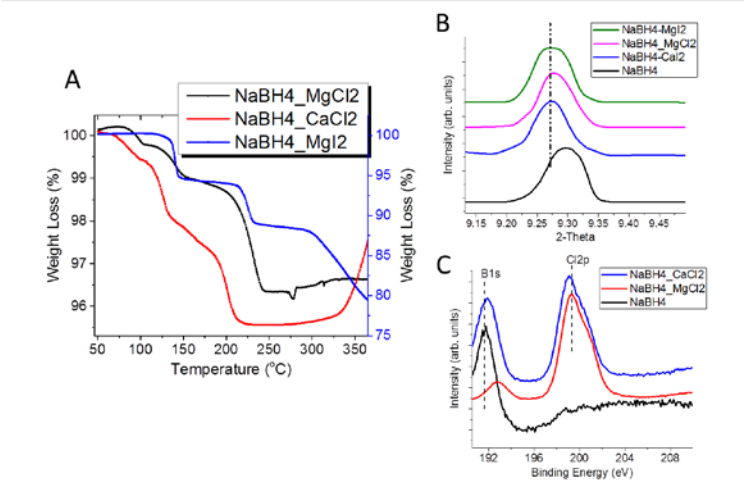

Figure 21. (a) TGA and (b) XRD of $NaBH_4$ with additives $MgCl_2$, $CaCl_2$, and MgI_2, and (c) XPS of NaBH4 with $CaCl_2$ and $MgCl_2$.

Magnesium Borohydride Eutectics

The eutectic mixture of $MgCl_2$ and $Mg(BH_4)_2$ was synthesized by chemical solution-based methods. To investigate the hydrogen storage performance depending on the degree of $MgCl_2$ in eutectic mixture the weight

ratio of Cl source to Mg source was controlled from 1:9 to 2:8 and 4:6, which are designed as 1$MgCl_2$-MBH, 2$MgCl_2$-MBH, and 4$MgCl_2$-MBH, respectively. As a result, TGA shows that larger weight loss in the mixture occurs than in pure gamma-MBH at between 100°C and 300°C. Interestingly, 4$MgCl_2$-MBH shows largest weight loss between 150°C and 350°C among the other mixture with the lowest temperatures of phase change confirmed by DSC. As a representative, 4$MgCl_2$-MBH was characterized by scanning electron microscopy (SEM) and energy dispersive spectroscopy (EDS). Figure 22b shows that the crystallite size of 4$MgCl_2$-MBH is approximately 2 micrometers and other mixtures show similar size as well. In addition, elemental analysis confirms that 4$MgCl_2$-MBH is composed of magnesium, chlorine, and boron and, notably, chlorine elements are well dispersive in bulk. The atomic weight (wt %) of chlorine in 1$MgCl_2$-MBH, 2$MgCl_2$-MBH, and 4$MgCl_2$-MBH is increasing from 0.654 to 2.79 and 13.0 respectively. Powder X-ray diffraction confirms that the crystal lattice of MBH is more expanded by $MgCl_2$, with larger quantities of $MgCl_2$ (Figure 22c). In addition, it is clear from XPS data that $MgCl_2$ and MBH have a notable influence each other on binding energies of B and Cl within the system (Figure 22d).

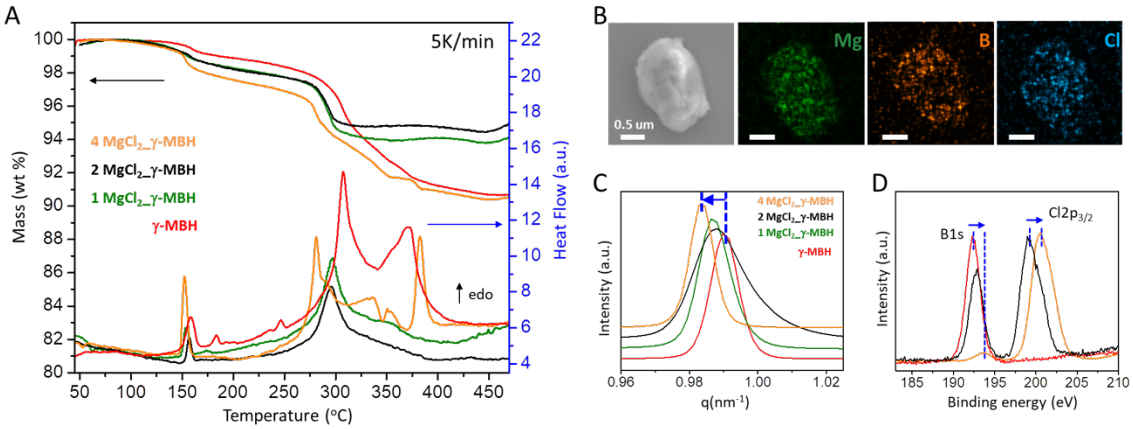

Figure 22. (a) DSC-TGA measurements of eutectic mixture and pure gamma-MBH. (b) SEM image and the corresponding energy dispersive X-ray spectroscopy (EDS) mapping of 4$MgCl_2$-MBH for Mg, B, and C, respectively. (c) Wide-angle X-ray scattering (WAXS) and (d) Cl K-edge X-ray absorption near edge structure spectroscopy (XANES) of gamma-MBH, 1$MgCl_2$-MBH (1:9), 2$MgCl_2$-MBH(2:8), and 4$MgCl_2$-MBH(4:6) (weight ratio of Cl source to Mg source).

Task 3: Carriers

Determining the Free Energy of Reaction for Release of Hydrogen from Aqueous Formate Salts

We used in situ NMR experiments to measure the equilibrium constant for the reversible reaction between formate and bicarbonate, Reaction 1, resolving an apparent discrepancy in the literature. The measured K_{eq} leads to a calculated ΔG^0 (ca. 0 kJ/mol H_2) consistent with reversibility at low temperature and pressure.

$$\text{(Reaction 1)} \qquad HCO_2^- + H_2O \Leftrightarrow HCO_3^- + H_2$$

It is notable that ½ the hydrogen comes from water and ½ from the formate salt. This is important as it can lead to a high volumetric density of storable hydrogen as the solid formate salt. Formate salt is attractive as a storage and hydrogen carrier as it is non-toxic and non-flammable. The product, bicarbonate, is non-toxic and non-flammable and used in both the food industry and as a road deicer. Solution phase NMR was used to measure the approach to equilibrium at room temperature and experimental work at 60°–80°C determined the optimum reaction conditions for the release and uptake of hydrogen. Figure 23 compares the volumetric capacity of different formate salts as:

1. Storable Capacity: the volumetric capacity of the solid at single crystal density or as a saturated solution.

2. Deliverable Capacity: the volume of hydrogen that can be released from a saturated formate solution with any additional water required provided after delivery.
3. Usable Capacity: the volume of hydrogen that can be released from a formate solution at the saturated concentration of the corresponding bicarbonate.

The figure demonstrates how the bicarbonate solubility limits the capacity of a purely liquid system, and that solid bicarbonate or a suspension of bicarbonate may need to be transported back for regeneration in a full cycle.

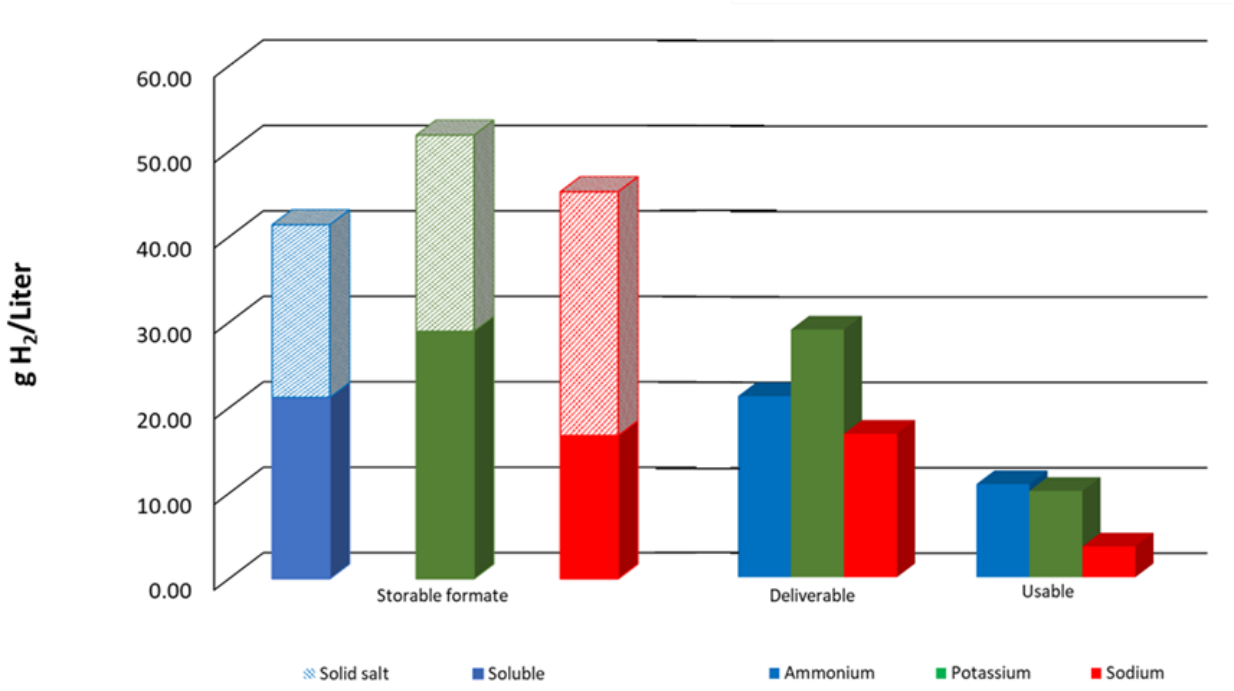

Figure 23. Comparison of hydrogen storage capacities of formate salts considering solubilities of both formate and bicarbonate

We initiated an experimental effort to develop catalysts for the reversible release of hydrogen from aqueous organic compounds, in particular alcohols and polyols. We considered several MOF-based catalysts for the dehydrogenation of methanol, ethanol, ethylene glycol, and glycerol. Catalysts based on the MOF-74 framework (i.e., M_2(dobdc), where M = Mg, Ni, Co and dobdc = 2,5-dioxido-1,4-benzenedicarboxylate) were prepared, both as-synthesized and Ni-doped. Experiments in a packed-bed gas-flow reactor demonstrated that the nickel-containing MOFs catalyze H_2 production from all three alcohols starting at ~150°C at atmospheric pressure, with hydrogen evolution rates as high as 28 mL/min. We also plan to explore these reactions in the liquid phase once an automated Parr reactor system is installed at Sandia. In general, zirconium-containing MOFs are a logical starting point because they are stable to both water and hydrogen. In addition, these MOFs, such as the UiO series, have Lewis acid open metal sites for binding the alcohol and tunable pore dimensions. Preliminary experiments were performed using UiO-67, which we synthesized and infiltrated with metal carbonyls (Fe, Co, Ir, Ru) to introduce transition metals in low oxidation states within the MOF pores. We find that that these doped MOFs catalyze hydrogen production from both ethylene glycol and glycerol.

Techno-Economic Analysis

We developed an adsorption process model and simulated the performance of a fixed-bed tube trailer system using experimental data for M_2(dobdc) and M_2(*m*-dobdc) (M = Co and Ni). Through this model, we found that parameters such as pellet and bed porosity had a significant effect on total H_2 uptake and saturation time

(Figure 24). The costs associated with the size and operation of equipment at the hydrogen terminal through to the refueling stations were demonstrated for these materials at experimental temperatures and pressures. We ran several scenarios using our carrier model to understand the allocation of energy and costs across supply chains. When studying costs for a carrier fleet delivering 50,000 kg/day with 100 km to an end point, we found that adsorption-based truck transmission is dominated by the cost of the trucks and their on-road operating costs. Increasing per-truck hydrogen working capacity without increasing upstream energy costs is critical for moving toward cost parity with 500 bar trucks and cryogenic liquid trucks. Distribution costs decrease substantially (potentially by as much as 40%) for adsorption-based gas trucks when allowing a twice-per-day truck delivery mode at in-city refueling stations, as a result of larger capacity refueling stations and the need for fewer trucks in operation.

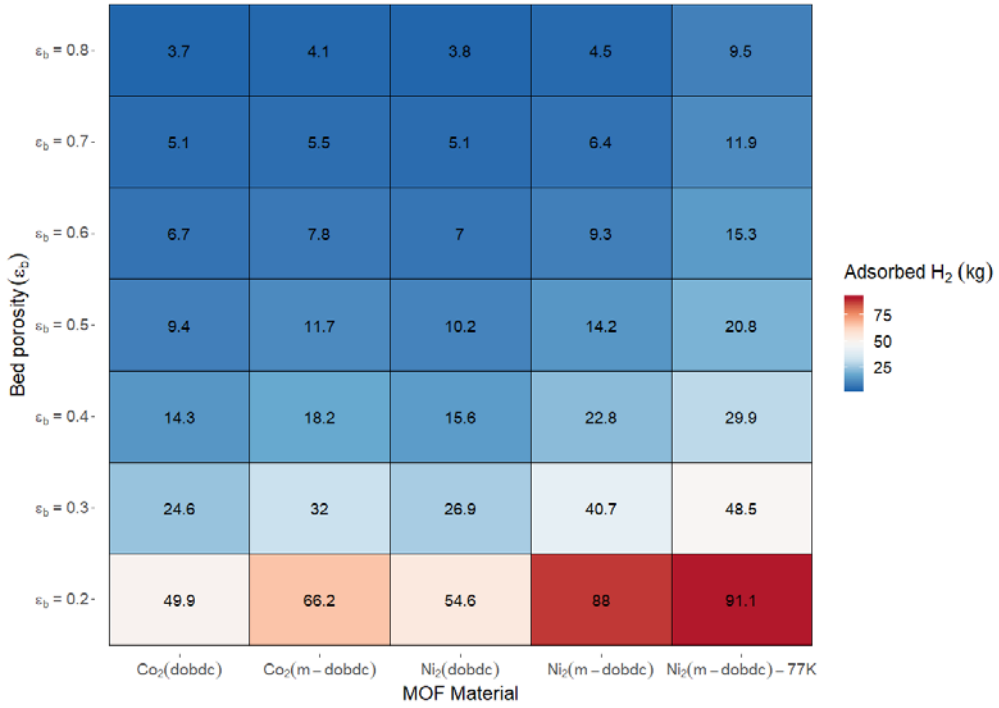

Figure 24. Effect of fixed-bed porosity on total H_2 uptake (kg H_2) in one 12-meter-long tube at a fixed pellet porosity of 0.2 (P = 100 bar, T = 200 K [first four MOF materials]). A typical trailer is assumed to have nine tubes.

Plasmonic Induced Release of Hydrogen

We have investigated the interaction with light and TiN/MgH_2 for hydrogen desorption. The group has calculated the electronic states at the interface of TiN and MgH_2 by DFT (Figure 25). The results suggest that charge transfer of photoexcited TiN electrons to the conduction band of MgH_2 may be favorable, while charge transfer from Au, Mg, or non-excited TiN surfaces seems to be thermodynamically disfavored.

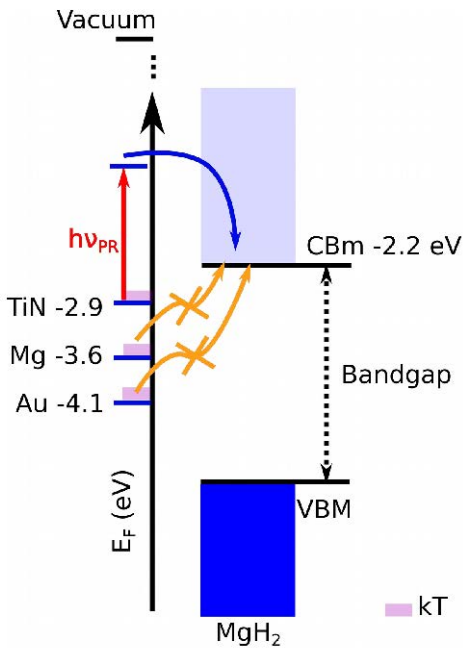

Figure 25. Schematic of DFT-calculated band alignments shown at the interface with MgH_2

We have synthesized Al_2O_3 coated TiN and combined with MgH_2, so that the Al_2O_3 blocks the electronic transfer from the TiN to the MgH_2 (Figure 26). The experimental results from temperature programmed desorption show that the Al_2O_3 coating on the TiN with MgH_2 decreases the H_2 desorption by 54% compared to uncoated TiN and MgH_2. This data and the DFT results suggest that the photonic excitation enables electron transfer from TiN to the MgH_2 to desorb H_2, and this transfer is hindered by the Al_2O_3 coating.

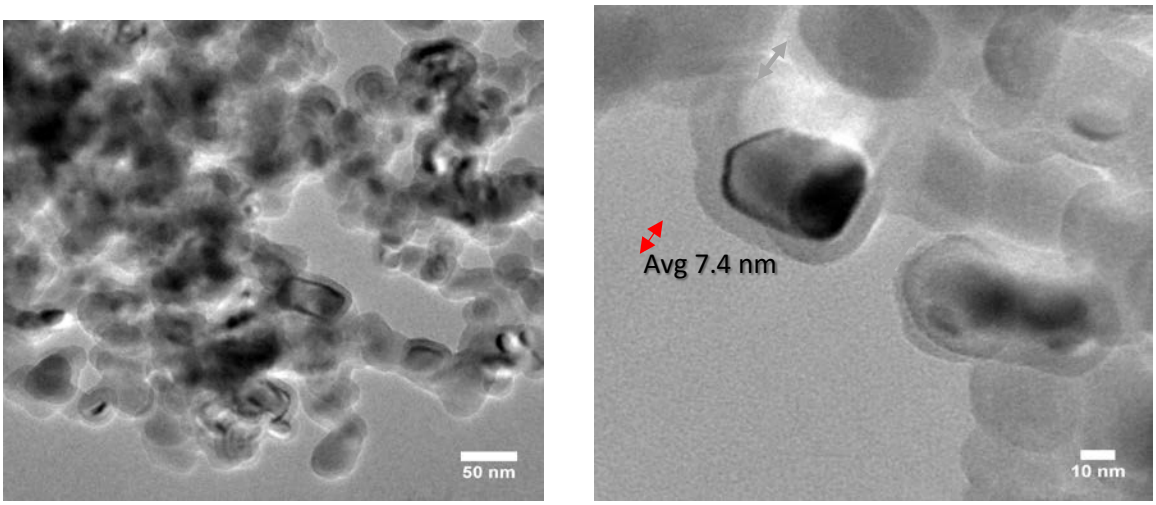

Figure 26. TEM of uniform ~7.4 nm ALD Al_2O_3 coating surrounding TiN particles

Our new cell for enhancing light exposure to the sample has been made. It is a versatile sample holder that can be connected to the TPD system for measuring desorption species with a mass spectrometer or connected to a Sieverts low-pressure volumetric system to accurately monitor the number of moles of gas desorption. This cell will enable more reproducible measurement and maximize efficient transfer of light to the sample.

The key result in FY 2019, 1 wt % H_2 desorbed from a TiN: MgH_2 mixture in 5 minutes by illuminating the sample with 200 mW 625 nm LED light source (Figure 27).

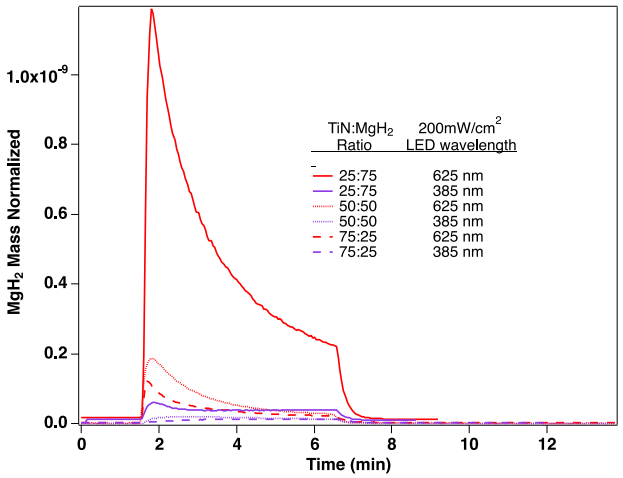

Figure 27. Hydrogen desorption of different compositions of TiN:MgH_2 mixture

Porous Liquids

We demonstrated viability of the click chemistry or nitrene approach for COF shell functionalization (Figure 28). The azide-alkyne cycloaddition reaction ("click chemistry") is an extremely efficient reaction for the functionalization of substrates and surfaces. Here, we employed the reaction to functionalize the surface of a colloidal COF particle in order to keep it better suspended in some liquid medium. A three-step reaction was designed, and DRIFTS was used to verify both the appearance and disappearance of all relevant frequencies during the three-step functionalization of COF (-Br, -N_3, and then respective ionic liquid). This approach was also used to covalently attach alkyne-functionalized polymers.

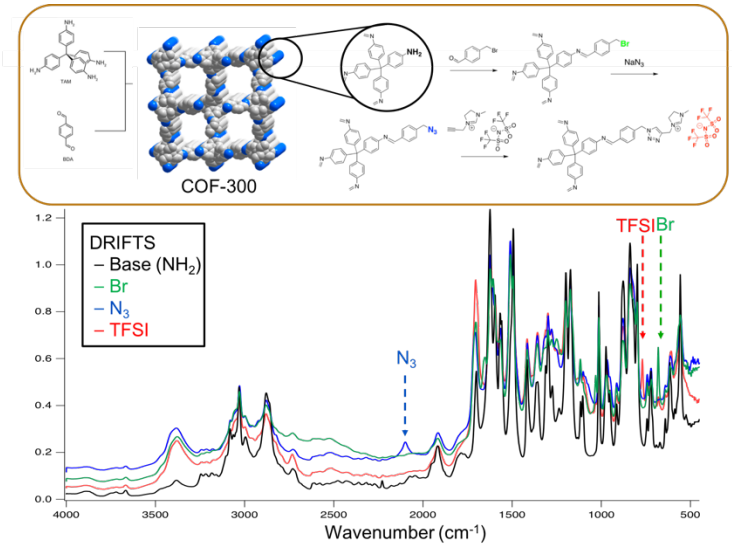

Figure 28. (Top) Synthetic scheme for "click-chemistry" approach to functionalizing COF particles with tethered ionic liquids. (Bottom) DRIFTS data confirming functionalization at each step.

Figure 29 and Figure 30 show the synthesis of the first COF-based porous liquid from COF colloids <100 nm in diameter. Functionalized COFs were successfully suspended in a bulky, size-excluded ionic liquid. No settling/aggregation of the colloidal COF suspension was observed after 6 h of centrifuging. Measurement of pore-size distribution of the colloidal COFs suggests that certain BAr^F-based ionic liquids should be size excluded from entering the framework pore. Confirmation of that size exclusion is under-way with solid-state NMR experiments being conducted at PNNL. Furthermore, H_2 desorption is currently being studied with TPD

for various porous liquid compositions. Preliminary data suggests the frozen liquid matrix may significantly influence the temperature at which H_2 desorbs from the framework.

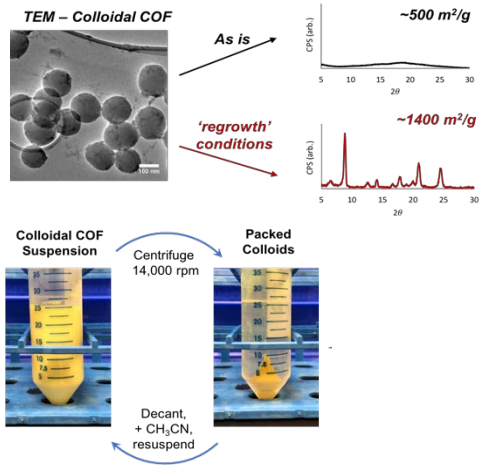

Figure 29. (Top) TEM images of 100 nm spherical COF-300 colloids. XRD reveals colloids become crystalline after "regrowth" process (bottom).

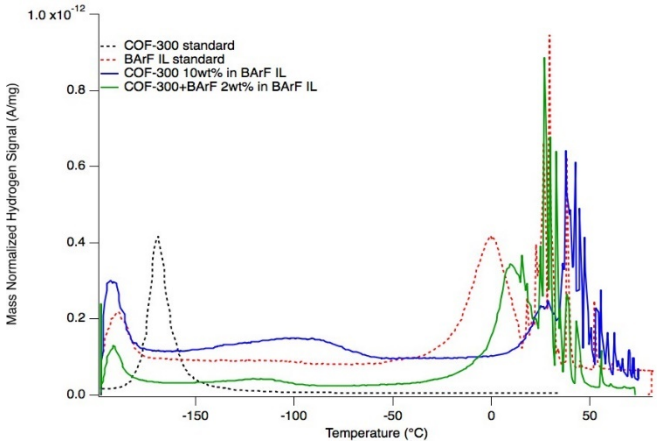

Figure 30. H_2 desorption was monitored from a dry COF-300 powder (black trace) in a tetrakis(3,5-bis(trifluoromethyl)phenyl)borate imidazolium-based IL (red) and in a 10 wt % COF-based porous liquid (blue) at a ramp rate of 10°C/min.

Bioinspired Process for Release of Hydrogen from Formate

We engineered *Escherichia coli* to release hydrogen from formate. This includes removing regulation of the formate hydrogen lyase complex (FHL) so that the hydrogenases are constitutively expressed, enabling prolonged H_2 release. The first task required the deletion of the repressor (encoded by *hycA*), which transcriptionally represses the FHL in the presence of oxygen and H_2. The second task required the overexpression of the activator, which increases FHL expression (encoded by *fhlA*) under low pH (pH ≤6.5) (Mcdowall et al. 2014). The resulting genetic modifications should enable constant expression of the FHL complex, which has been previously shown to improve H_2 release from hydrogen (Yoshida et al. 2005). In addition to genetic modifications, we additionally sought to improve the reactor conditions for optimal H_2 release. These included optimizing media composition, pH, temperature for H_2 release, and formate concentration.

Specific achievements:

- The repressor *hycA* was successfully deleted, and the *fhlA* gene was successfully expressed. Each of those modifications was tested individually, and the two were tested in conjunction. Deletion of the *hycA* regularly results in approximately 20% improvements in the H_2 release from formate than the unengineered wild type parent strain (60 mM versus 52 mM H_2 in 1 hour, respectively)
- Overexpression of *fhlA* was achieved, but it appeared to be unbalanced. Unbalanced expression manifested as a complete drop in H_2 production under *fhlA* overexpression. Lower expression may be required as overexpression can lead to insoluble protein expression or the formation of inclusion bodies—both would result in a nonfunctional FHL complex, as observed. We next seek to better balance *fhlA* expression.
- We optimized the concentration of sodium selenite in the medium, as we observed toxicity with the initial concentration of this compound tested, in addition to the formation of an orange color. Titrating this compound allowed us to identify a concentration that allowed H_2 release without cell toxicity, observed by lower growth.
- Additional process parameters were optimized, specifically media formulation for bacterial growth, and working formate concentration. Formate concentration was increased to a concentration of 100 mM, from which the bacteria were able to completely release H_2 within one hour.
- Between process and genetic engineering, we achieved 4.2-fold improvements in hydrogen release from formate during FY 2019 (Figure 31).

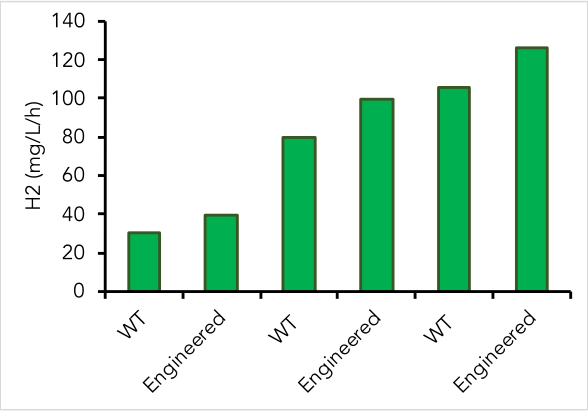

Figure 31. Biological hydrogen release from formate. "WT" denotes the unengineered *E. coli* strain, and "engineered" denotes an engineered variant of *E. coli* (MG1655 Δ*hycA*). Process improvements and increased cell density have improved H_2 release by 4.2 fold.

Boron Nitride Sorbents and LOHC Catalysis for Dehydrogenation

BN work: The interaction between few-layered BN nanosheets and ~2 nm Ni nanoparticles makes the BN/Ni nanocomposite promising in hydrogen storage as well as acting as a catalyst for dehydrogenation of liquid organic hydrogen carriers (LOHCs). We used a combined method of gas exfoliation and lithium intercalated exfoliation to prepare few-layered BN nanosheets (Figure 32a, top). Afterward, Ni nanoparticles with ~2 nm were deposited at the surface by reducing Cp_2Ni using Li- naphthalenide (Figure 32a, bottom). We performed PCT testing on the exfoliated BN, Ni nanoparticles, and Ni/BN composite (Figure 32b). The data shows that pure Ni nanoparticles and exfoliated BN didn't exhibit very clear hydrogen uptake property while the Ni deposited BN nanocomposite shows an improvement of ~3.5 times in the hydrogen storage, mainly due to the hydrogen spillover effect. This was eventually not meeting targets and selected as a no-go.

LOHC catalysis: In addition, the Ni/BN nanocomposite we prepared was found to be one of the best catalysts for the dehydrogenation reaction of LOHCs (methanol) with high activity and selectivity. This work is collaborative with Dr. Ji Su in the Somorjai Group (LBNL). The reaction started to be dehydrogenated at

150°C and shows very high hydrogen productivity of 57.13 mL/min and methanol conversion of 51.94% at 350°C (Figure 32c). Furthermore, the composite-based catalyst shows very high selectivity for the reaction. Methane byproduct that was always found in the reactions of other nickel-based catalysts was not found in Ni/BN based catalysts (inset of Figure 32c). The performance of Ni/BN based catalyst is also much better than that of the pure nickel nanoparticle and nickel nanoparticles with carbon substrates. The high activity and selectivity could be attributed to the ultrasmall-sized Ni nanoparticles and the BN substrate effect (spillover effect, appropriate hydrogen binding energy, and fast hydrogen diffusion rate on the substrate). This work is very promising and deserves further inquiry.

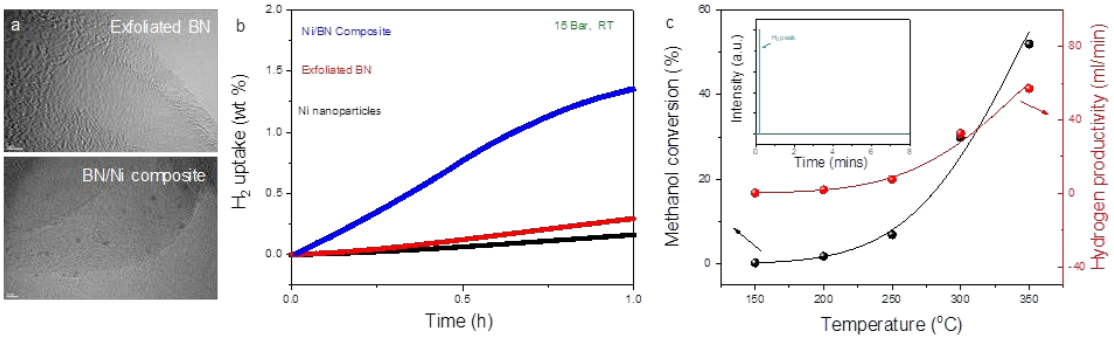

Figure 32. (a) TEM images of exfoliated BN nanosheets and Ni/BN nanocomposite. (b) PCT testing on the exfoliated BN, Ni nanoparticles, and Ni/BN composite. (c) Performance of Ni/BN composite used for the dehydrogenation reaction of LOHCs (methanol).

Task 4: Research and Development of Advanced Characterization Capabilities

High-Temperature PCT

During FY 2019, a high-temperature PCT capability was developed and met a milestone. Specifically, the capability extended the existing upper temperature range to 350°C from the previous limit of 30°C. The approach used a fluidized sand bath to control a stable, homogeneous, and reproducible temperature profile for the sample region under the current methodology for capacity determination using the manometric (Sieverts) technique. The new limit of 350°C provides a reasonable safety factor given the current pressure limit of ~200 bar and the mechanical properties of the stainless-steel sample containers under elevated temperatures and in the presence of hydrogen (embrittlement). The critical issues to maintain high accuracy for the PCT measurements are a stable and reproducible temperature profile for the instrument, a corresponding realistic mole-balance equation to determine the sorption amount, and appropriate measurement and calibration protocols. To verify that sufficient accuracy and precision has been achieved requires verification steps that can be divided into two categories: null measurements and measurements on known materials. The null measurements are actually the more important of the two categories as they test the entire system (temperature profile, mole-balance, and protocols) at high sensitivity, while the known-material tests provide verification of the absolute calibration of the system assuming that the null tests have been successfully passed.

The development of this capability also required integrating the fluidized sand bath with the existing equipment. This required both mechanical integration with an appropriate sample container and establishment of a stable and reproducible temperature profile and slight modification for the mole-balance model in the data analysis. Once this was accomplished, the null tests were performed at several temperatures giving satisfactory results with an accuracy of roughly 20 micromoles per cycle. For the known material, palladium metal was used and measured at four temperatures, as it is a highly known and studied material for hydrogen absorption. It showed excellent agreement with the known literature (see Figure 33).

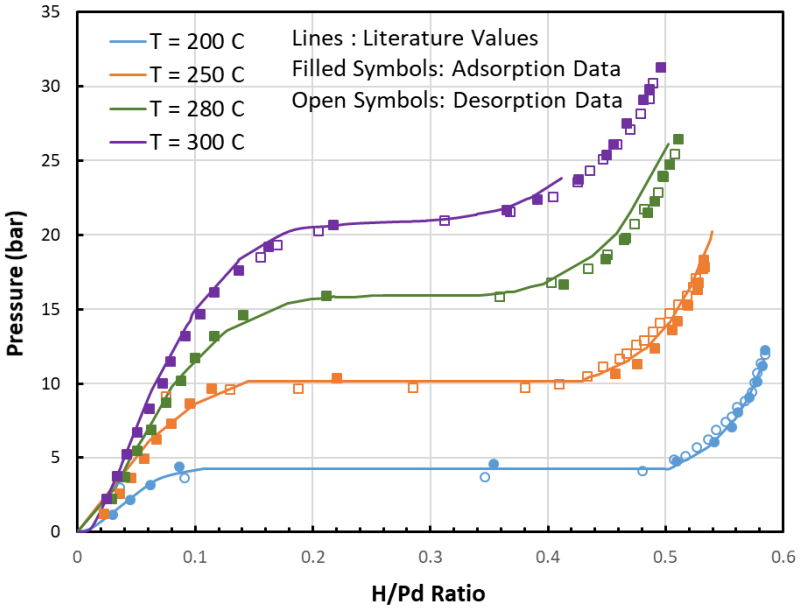

Figure 33. Comparison between the NREL data (symbols) compared to the literature values (lines; L.J. Gillespie and L.S. Galstaun, *J. Amer. Chem. Soc.* 58 [1936]: 2565) at four different temperatures

Development of Methodology for VT FT-IR

Here we determined the reproducibility and variance of the VT FT-IR method for determining adsorption thermodynamic parameters. Several sets of repeated measurements were performed on the framework Cu(I)-MFU-4*l* in order to generate statistics, and different data processing methods were applied in order to test the robustness of data. Multiple sets of data at different pressures, temperatures, and coverages were collected. We were able to generate a van't Hoff plot with errors from spectra processing and accordingly improve our methods of baseline correction and integration (Figure 34).

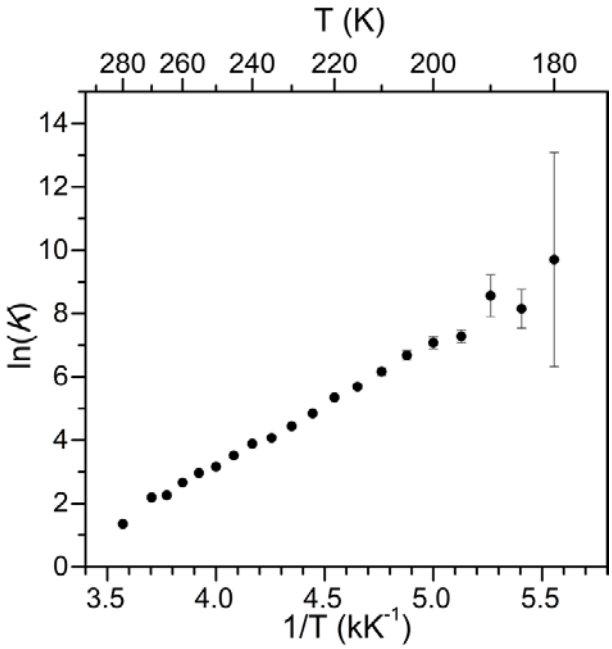

Figure 34. van't Hoff plot using integrated peak areas of H_2 adsorbed in Cu(I)-MFU-4*l*. Notably, error increases to infinity as coverage approaches 1.

Thermal Conductivity

The focus of this work was to expand the capabilities of the thermacl conductivity (TC) apparatus to do measurements under two different dosing conditions: (a) "equilibrium pressure" and (b) "micro-dosing conditions." The term "equilibrium pressure" refers to the equilibrium pressure reached in the measurement cell (i.e., the pressure value read by the pressure gauge connected to the measurement cell), as opposed to the pressure injected into the system, which is referred to "micro-dosing" and represents the dosing pressure. We are evaluating the apparatus' ability to perform these micro-dosing experiments, which would potentially enable us to correlate the TC with gravimetric/volumetric capacities based on PCT measurements, as well as differentiate different binding sites in sorbents.

"Equilibrium pressure": Cu-MFU-4*l* from LBNL (Long et al.) provided us with the first H_2 sorbent material in the form of a powder. Because LBNL was interested in the "volumetric" heat capacity (VHC), the graphs shown below focus on the VHC, which depends on the TC and the diffusivity (Diff.) of the material. These two properties, TC and Diff., were extracted from modeling the thermal response measured at room temperature and equilibrium pressures ranging from 0.02 bar to 5 bar. Using the Cu-MFU-4*l* material, we validated the measurement and analysis methods for powders, such as (the investigation of the bold parameters is complete):

the duration of the measurement	the sensor-to-sample dimensions
the data range to be fit	**the applied power to be chosen**
the model to be used	the validity of the thermal diffusivity

the need for adding a time correction into the analysis

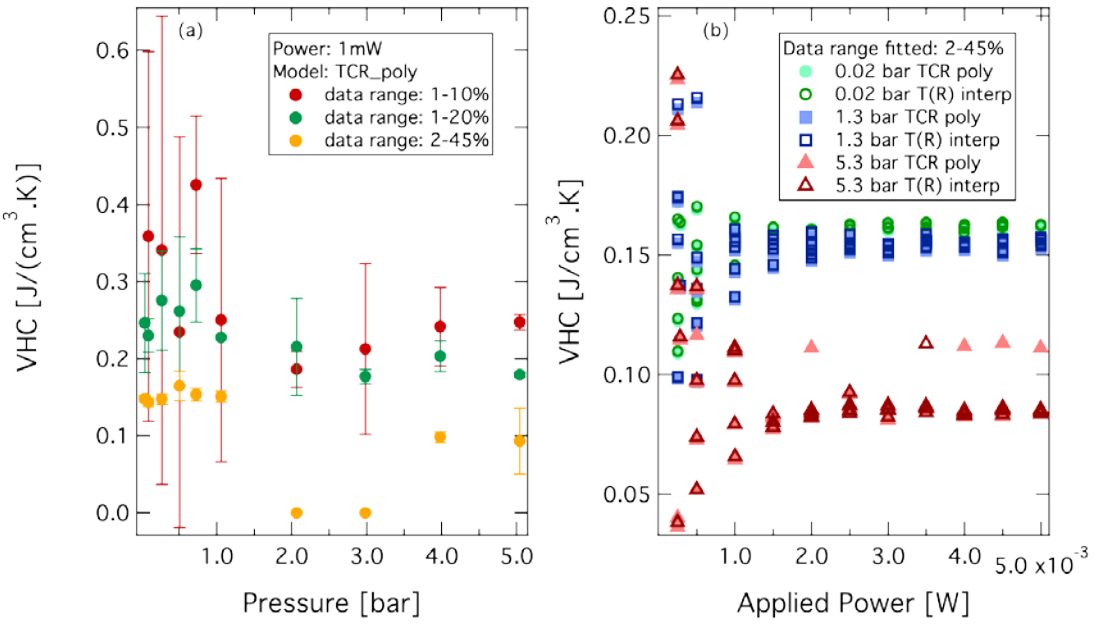

Figure 35. "Volumetric" heat capacity of Cu-MFU-4l depending (a) the data range being fit during the data analysis and the reproducibility of the data since the error bars depict the standard deviation over 5 measurements at the same conditions, and (b) on the applied power and on model used (TCR poly and T(R) interp).

The data shown in Figure 35 have all passed the rudimentary validity criteria imposed by the protocol developed and based from Gustafson et al. From the results shown in Figure 35a and Figure 35b, we concluded that for Cu-MFU-4*l* low pressures ($p \leq 1$ bar) and low applied powers ($P \leq 1$ mW) yield the broadest deviations, while the two different models currently do not show a trend. The lowest standard deviation was obtained

when fitting the data range of 2%–45% of the time series taken. To investigate if the irreproducibility in the low-pressure region is due to a regime in which the interaction of the material with H_2 is dominating the free gas contribution, we plan to attempt measuring the TC and Diff. at conditions in which we can predict the gravimetric capacity of the material, which is why we started developing the micro-dosing efforts.

"Micro-dosing conditions": The assessment of the apparatus potential for accurate TC and Diff. measurements at micro-dosing conditions requires a volume calibration and a test material for which the H_2 physisorption is known as a function of pressure and temperature. We completed the volume calibration and will test the capability with Cu-MFU-4*l* since its sorption performance is known.

SLAC X-Ray Techniques

Optimization of the in situ Sample Cell

Initial measurements at the Stanford Synchrotron Radiation Light Source were designed to demonstrate and optimize capabilities of the newly implemented in situ capillary sample cell. γ-$Mg(BH_4)_2$ was chosen as a prototypical material due to its rich decomposition phase diagram. X-ray diffraction measurements performed between room temperature and 600°C under 5 bar hydrogen back pressure can be seen in Figure 36. At room temperature pure γ-phase is observed with some amount of amorphous material evident by the broad band at 1.5 $Å^{-1}$. Surprisingly at temperatures as low as 50°C, the epsilon phase can be detected. By 150°C, the material transitions to pure β-$Mg(BH_4)_2$ before losing signal from the borohydride altogether at 300°C. Here, reflections from rutile-type MgH_2 are observed with simultaneous formation of MgO. At even higher temperatures Mg metal is generated prior to reaching the MgB_2 endpoint around 500°C. Low temperature capabilities were also explored using an Oxford Cryostream, which can achieve temperatures as low as 90 K. Lower temperatures (c.a. 12–90 K) require a custom-built cell to mount on the second stage of a cryostat (currently under development).

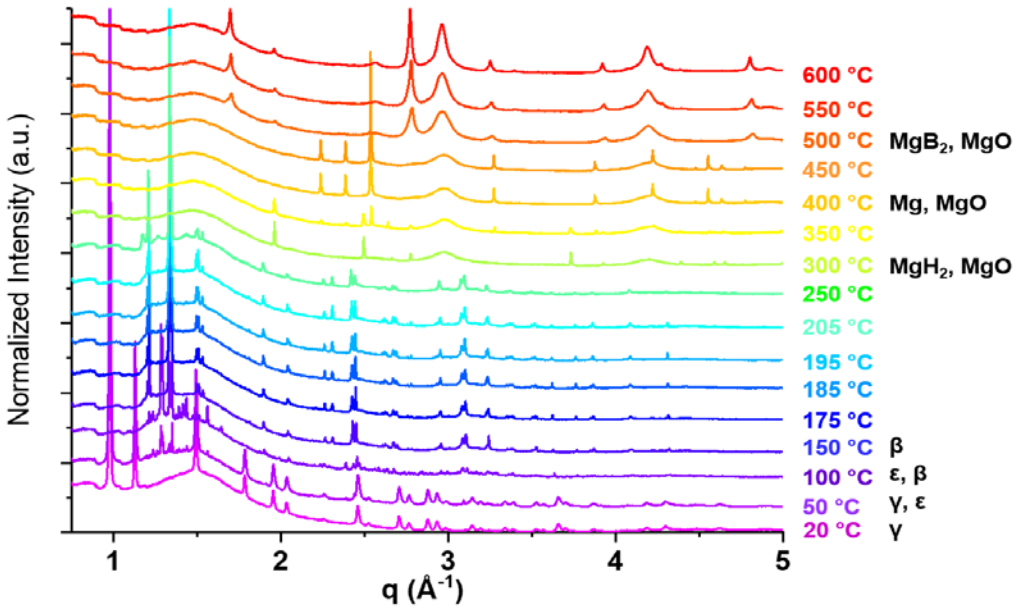

Figure 36. In situ XRD obtained during the thermal decomposition of SNL's γ-$Mg(BH_4)_2$ material between room temperature and 600°C under 5 bar H_2 pressure

Small Angle X-Ray Scattering of Mesoporous Carbons Infiltrated with $Mg(BH_4)_2$

Small angle x-ray scattering (SAXS) was used to examine melt-infiltration of β-$Mg(BH_4)_2$ in mesoporous carbons in collaboration with Sandia National Laboratories. Four samples were investigated: two graphene aerogels heat-treated at 1,500°C and 2,000 °C (synthesized by LLNL) and two templated carbons, CMK-3 and CMK-8 templated by SBA-15 and KIT-6 respectively. The size domains of pore infiltration were identified by

partial contrast matching between the borohydride and carbon. For the templated carbons, the mesostructures were largely unmodified by the infiltration process as indicated by the absence of shifts of mesostructure SAXS peaks. In situ measurements were conducted in order to compare the temperature dependence between melt and solvent infiltration methods. For the solvent infiltrated sample, a significant increase in low-q intensity was observed at high temperatures, which suggested borohydride particles agglomerated and formed larger domains. The melt infiltrated sample maintained a constant intensity at low-q (where agglomeration would be expected to appear) with increasing temperature, which suggested the size of infiltrated borohydride remained constant even at high temperatures (e.g., 500°C) (see Figure 37). While the β-$Mg(BH_4)_2$ infiltrated CMK-3 system did not yield sufficiently low decomposition temperatures, the results of this investigation were used to determine the optimal method for nanoconfining hydrides within porous materials. This approach also offers a path forward for preventing particle agglomeration in nanoparticles.

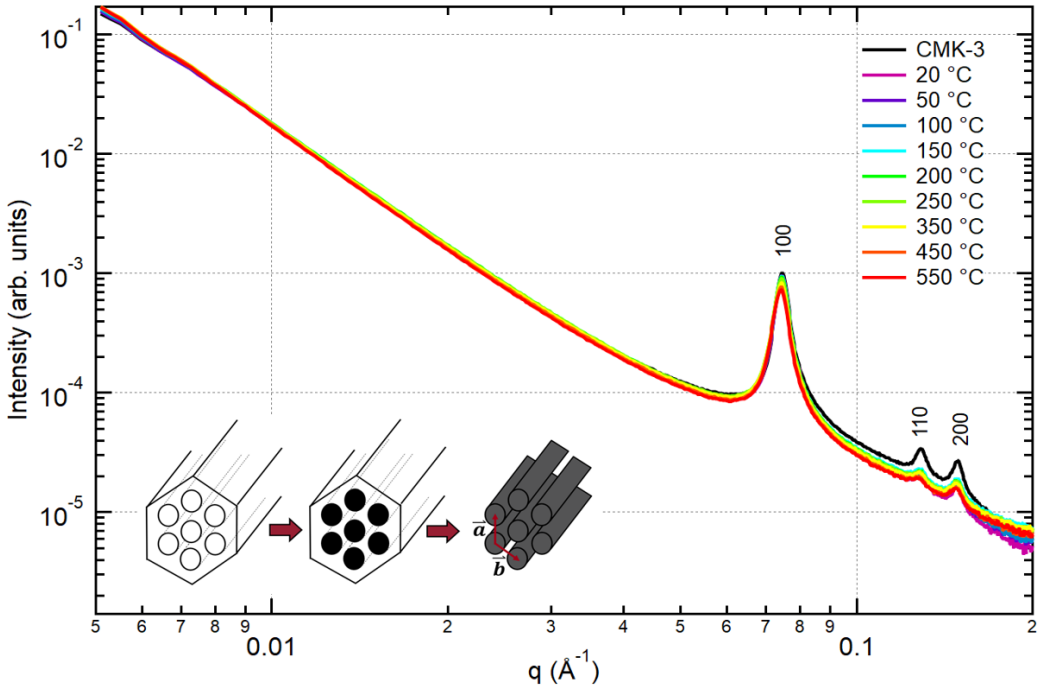

Figure 37. In situ SAXS for CMK-3 melt-infiltrated with β-$Mg(BH_4)_2$. The inset shows an illustration of the CMK-3 mesostructure, which corresponds to the 100, 110, and 200 reflections labeled in the SAXS pattern.

Structural Characterization of ALD-Coated $Mg(BH_4)_2$

XRD and SAXS were used to characterize the structure of ALD-coated magnesium borohydrides. The results of these investigations provided necessary information for understanding the rapid release of hydrogen at relatively low temperatures. Four different types of ALD-coatings were provided by NREL: [$Al_2(CH_3)_6$ + H_2O], [N_2H_4 + BBr_3], and [N_2H_4 + $TiCl_4$], and a combination [N_2H_4 + ($TiCl_4$ + BBr_3)]. Ex situ SAXS measurements on "Al-O" coated material (see Figure 38a) indicated the trimethylaluminum precursor accesses the pores of γ-$Mg(BH_4)_2$. The scattering contrast difference between argon-filled pores and TMA-filled pores is greater than an order of magnitude explaining the dramatic increase in intensity at q ~ 0.1 Å^{-1}. XRD patterns for 100 cycle [TMA+H_2O] ALD-coated $Mg(BH_4)_2$, shown between room temperature (~20°C) and 500°C, can be seen in Figure 38b. The inset provides a comparison between neat γ-$Mg(BH_4)_2$ (red trace) and ALD-coated γ-$Mg(BH_4)_2$ (black trace) under identical conditions. The crystalline component of the "as-deposited" material at room temperature is dominated by γ-phase $Mg(BH_4)_2$ identified by the open circles in Figure 38. Compared to the diffraction pattern from uncoated powder, this material exhibits appreciable peak broadening, presumably from defects induced by the ALD process, the coating itself, and/or possible hydrolysis. A broad diffraction band is also observed near q ~1.5 Å^{-1} which is likely a combination of amorphous Al-O species and hydrolyzed borohydride. Surprisingly, a secondary phase was also detected with significantly narrower peaks

than the primary $Mg(BH_4)_2$ phase. The identity of this phase is not immediately clear, but peak indexing suggests a cubic space group with lattice parameter, a = 6.59 Å. Crystals with this particular symmetry and lattice size are consistent with structures of some transition metal alloys (e.g., $GaLiMg_2$). Assuming this is not a result of residual impurity metals in the ALD chamber, it is possible this is an alloy containing Mg, Al, and/or B or potentially a composite hydride (or borohydride). It is important to note that this set of reflections persists at temperatures below 175°C. The borohydride exhibits very little change between room temperature and 100°C (see Figure 37). However, upon reaching 125°C, the peaks corresponding to the borohydride abruptly narrow. Simultaneously, the metastable (and currently unsolved) ε-$Mg(BH_4)_2$ phase begins to appear, identified by a series of peaks between q ~1 and 1.5 $Å^{-1}$. Peaks from the epsilon phase reach maximum intensities near 175°C before disappearing completely at higher temperatures. This behavior was unexpected since β-phase $Mg(BH_4)_2$ observed in the decomposition of pristine γ-$Mg(BH_4)_2$ was bypassed altogether prior to the loss of crystallinity. Concomitantly, peaks from the unknown "alloy-type" phase disappear in the same temperature regime, which may suggest at elevated temperatures these two phases interact. Alternatively, this temperature may correspond to the thermodynamic crossover in free energy where oxide phases become more stable. Coincidentally, the onset of MgO formation is first observed at 200°C with increasing concentrations at even higher temperatures.

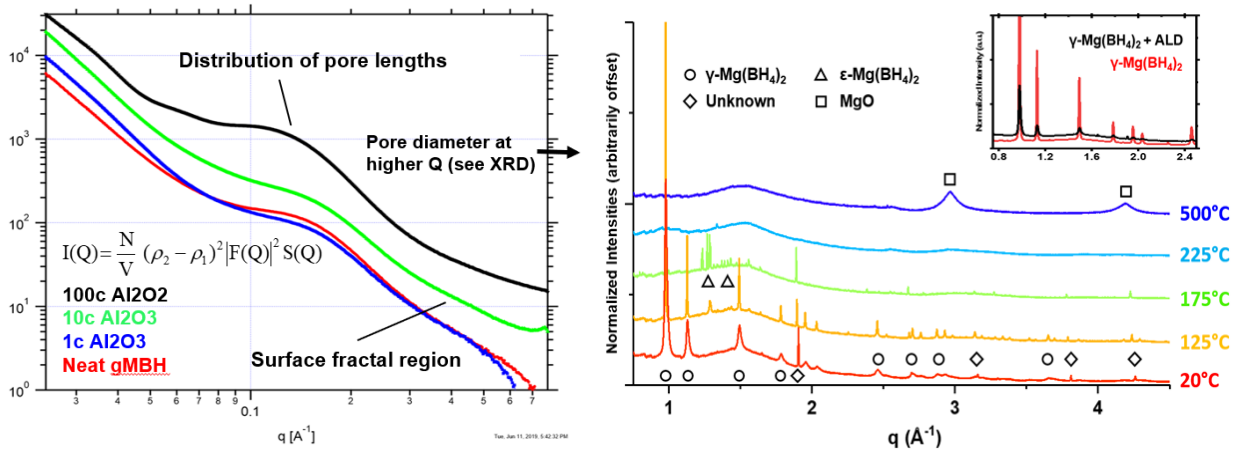

Figure 38. (a) SAXS patterns as a function of increasing ALD cycles. (b) In situ XRD obtained during the decomposition of $[Al_2(CH_3)_6 + H_2O]$ ALD-coated magnesium borohydride.

In situ XRD measurements were also obtained for 100 cycle $[N_2H_4+BBr_3]$ ALD-coated γ-$Mg(BH_4)_2$ between room temperature and 500°C. The full decomposition sequence is shown in Figure 39. Compared to the other two ALD deposition processes (i.e., Al-O and Ti-N), this powder exhibited the weakest signal for residual γ-$Mg(BH_4)_2$ in the as-deposited material at room temperature. Reflections from hydrazinium bromide (N_2H_5Br) were also observed at ~20°C and 50°C. As expected, a considerable amorphous signal was observed across a broad q range at temperatures below 90°C. Upon heating to 90°C, peaks corresponding to the borohydride and hydrazinium bromide disappear (note: HB m.p. = 93°C), accompanied by the onset of new amorphous bands located at approximately 1.5 and 2.1 $Å^{-1}$. At temperatures 90°C and above, a new set of diffraction peaks appear, consistent with the structure of $MgBr_2$ with anomalous hk-l absences. With increasing temperatures, the amorphous phase at 1.5 $Å^{-1}$ gradually increases in intensity while the secondary band at ~2.1 is lost by 400°C. At the highest temperatures (e.g., 400°–450°C), some previously absent $MgBr_2$ peaks begin to appear more clearly, although with poor powder averaging, which may suggest only a few small domains are formed. MgO is also apparent at 90°C with peaks increasing in relative abundance up to 500°C. Recent work has focused on reducing water content in the N_2H_4 precursor to limit the formation of hydrolysis products and oxide species, which are irreversible.

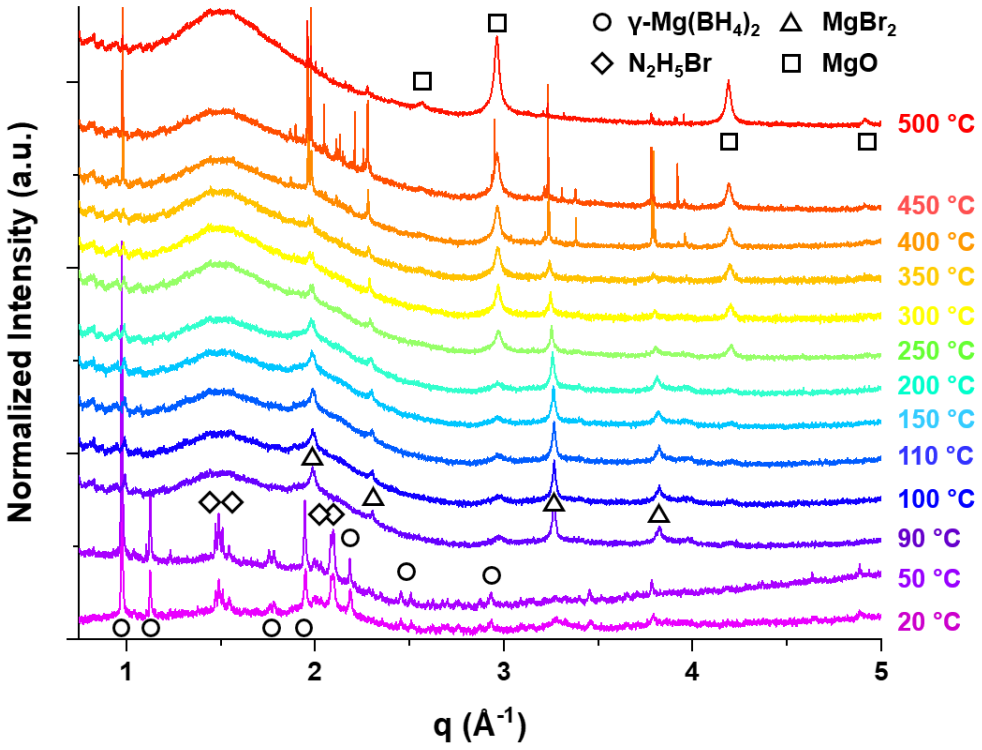

Figure 39. XRD patterns obtained during the thermal decomposition of 100c [N_2H_4+BBr_3] ALD-coated γ-$Mg(BH_4)_2$

XRD Structural Characterization of Self-Assembled 2D COFs

Ex situ XRD measurements were performed to support a seedling project led by J. Johnson at NREL. The purpose of this work was to demonstrate the impact of compression (in order to eliminate dead volume) on the crystallinity of phenyl- (COF1) and partially fluorinated phenyl- (COF3) covalent organic frameworks. As seen in Figure 40a, COF3 exhibits a significant enhancement in crystallinity compared to COF1 (Figure 40b). hk0 reflections display narrower peak widths compared to the non-fluorinated material. The 001 reflection is also observed at 2θ ~11.7 degrees, which is not present in the base-COF XRD pattern. Upon partial fluorination, hk-reflection peak shapes lose their asymmetric "sawtooth" peak shape and become dramatically more symmetric, which is further evidence of interplanar ordering.

Compression appears to have little effect (if any) on the in- and out-of-plane order except for the highest density sample (0.99 g/mL) where higher order reflections begin to broaden (e.g., 2θ = 9). One exception to this is the 0.36 g/mL sample where the peak intensities are slightly greater relative to the background suggesting there may be an "optimal" linear force (and compact density) at which the crystallinity can be improved. The peak widths are also largely unchanged with compression, which indicates that the distribution of atomic distances (and hence porosity) is maintained. Although these results indicate the self-assembly 1D sheets can be effectively controlled with click chemistry, the seedling project received a no-go decision from HyMARC. A new project focused on the design of 3D colloidal COFs as porous liquids is underway at NREL. As part of the FY 2020 Annual Operating Plan, SLAC is designing new sample cells and beamline configurations for conducting in situ SAXS/WAXS measurements during growth in order to provide greater control over particle size and structure.

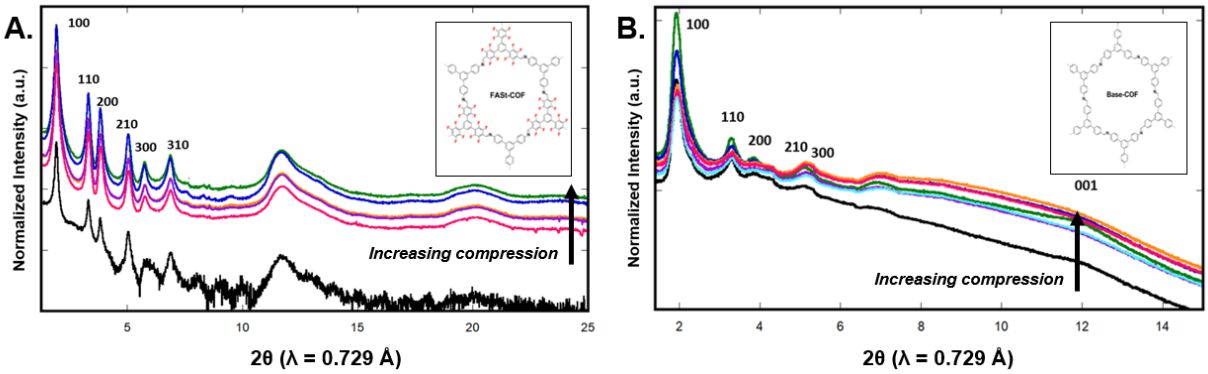

Figure 40. (a) XRD for partially fluorinated phenyl-based COFs (COF3) vs. (b) non-fluorinated phenyl COFs (COF1) as a function of increasing compression

Task 5: Seedling Support

Support for HyMARC Seedling Projects

Extensive calculations were performed in support of seedlings led by the University of Hawaii, NREL, and HRL. For the Hawaii project, we ran ab initio molecular dynamics simulations of MgB_2 chemistry and decomposition in the presence of key ether complexes, which showed possible mechanisms for weakening and restructuring of B-B bonds. In addition, X-ray absorption spectroscopy experiments were performed to complement the theory work and investigate possible B-B bond activation upon incorporation of additives that can alter the Mg composition. For the NREL project, we ran first-principles calculations of precursor incorporation into γ-$Mg(BH_4)_2$ to elucidate possible reaction chemistries during encapsulation via atomic layer deposition. We also provided guidance for testing the effects of mechanical strain on reaction enthalpy according to our models. For the HRL project, we initiated ab initio molecular dynamics simulations of MgB_2 in contact with molten alkali halide salts to understand how kinetics could be improved.

Characterization of copper loaded covalent organic frameworks (Cu-COF) provided important insights into the material's structure, chemical speciation, and activity. XAS verified that Cu(II) formate bound to the COF framework is reduced to Cu(I) when heated. As shown in the Cu k-edge XANES spectrum, Figure 41, peaks from the Cu(II) 1s to 3d transition and Cu(II) 1s to 4s or 4p transition are readily observable in the sample prior to heat treatment and are not present in the sample after heat treatment. The peak associated with the Cu(I) 1s to 4s or 4p transition is present only in the sample after heat treatment. Further, the decrease in intensity of the white line is indicative of a loss in coordination, as would be expected from the loss of CO_2 with heating and corresponding conversion to Cu(I). DRIFTS with hydrogen and deuterium allowed for the Cu(I)-H_2 stretch to be identified and confirmed that molecular hydrogen interacts directly with Cu(I) (Figure 42). Isolation and identification of the Cu(I)-H_2 stretch is important for ongoing work within our group as well as for work with Cu(I) in Jeff Long's group. FTIR was also valuable in confirming that the "click" chemistry used in the synthesis of COFs for liquid carriers was successful. DRIFTS was also the key to start unraveling the speciation and mechanism for hydrogen desorption in N_2H_4/BBr_3 ALD-coated magnesium borohydride. Substantial N-H speciation was clear in the spectra, and the peak positions were strongly indicative of a hydrazine bromide species being present (later confirmed with XRD).

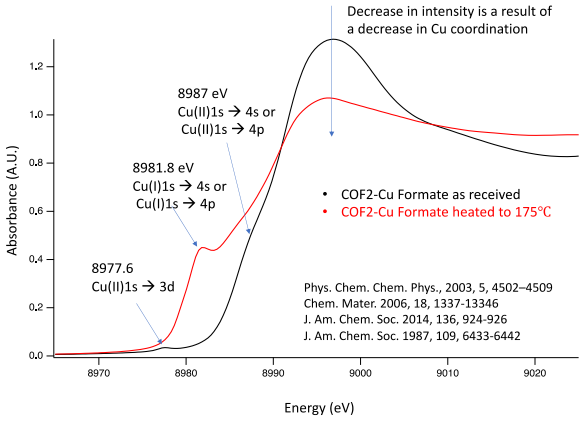

Figure 41. XAS spectra of Cu-formate loaded COF before heat treatment (black) and after heat treatment (red)

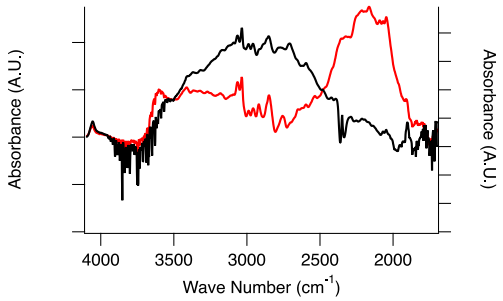

Figure 42. DRIFTS spectra of Cu(I)- COF with H_2 (black) and D_2 (red)

CONCLUSIONS AND UPCOMING ACTIVITIES

Our work this year lead us to several important conclusions. Regarding sorbents, solgel methods for creating dense MOF monoliths are extremely promising and represent a viable path forward for solving the powder packing problem and increasing the volumetric density. For metal hydrides, the non-intuitive tradeoffs revealed by systems analysis of nanoscale hydrides suggest that system modeling can provide valuable guidance during the evaluation of new strategies for developing storage materials. The results of our prototype machine learning investigation of metal hydride thermodynamics are very encouraging. We plan to make this an integral component of upcoming efforts to evaluate new strategies for these materials. As in the previous year, our integrated theory and characterization investigations provided new insights that prompt us to re-examine existing paradigms concerning the chemistry of metal hydrides. In particular, the assumption of fast surface- and near-surface hydrogen-releasing reactions is called into question by investigations of the Li-N-H system and Ti-doped $NaAlH_4$ (reported last year). In light of these results, we will refocus efforts in the coming year to take advantage of this new understanding. Finally, prototype experiments using MOFs as catalysts for releasing hydrogen from organic carrier molecules are encouraging. Expanded efforts in the coming year are planned to fully characterize and test these catalysts.

Progress continues to be made on predictive tools and capabilities that can guide strategies for accelerating kinetics and tuning thermodynamics of metal hydrides. We have placed particular emphasis this year on the development of modeling strategies that can predict nucleation kinetics, which are thought to be rate limiting in many of these materials. We have also demonstrated a new theoretical construct for understanding how additives can be used to accelerate MgB_2 decomposition. Future priorities will focus primarily on integration of our activities with experiments and validation of our proposed strategies, as well as extension to broader classes of metal hydride materials.

We have developed frameworks with basic metals, namely Cu(I)-MFU-4*l* and $V_2Cl_{2.8}$(btdd), that exhibit high H_2 adsorption enthalpies advantageous for the room-temperature hydrogen storage. During FY 2020, we will focus on structural characterization of the hydrogen binding sites within both materials. We will also endeavor to synthetically tune the binding energies and storage capacities for these frameworks by linker modification to alter binding electronics and decrease pore size toward higher volumetric capacities. We will also continue pursuing other frameworks capable of achieving desired adsorption enthalpies in the range of 15–25 kJ/mol. Finally, we will continue to pursue framework metalation to access low-coordinate metal sites capable of binding multiple H_2 molecules.

We also evaluated functionalized variants of the flexible framework Co(bdp) for their ability to exhibit enhanced H_2 working capacities as a result of step-shaped adsorption. Low-pressure H_2 adsorption measurements indicated that the pores of these frameworks remain closed at 77 K and below 1 bar H_2. We will evaluate the adsorption properties of these frameworks at ambient temperature and under higher pressures of H_2 (up to 100 bar) to investigate whether step-shaped H_2 adsorption can be achieved (relevant pressure for H_2 carriers is <250 bar). We will also explore whether metal substitution in Co(bdp) can be used to obtain step-shaped H_2 uptake. Over this reporting period, we also reproduced a published procedure for the preparation of monolithic HKUST-1 and demonstrated that H_2 uptake in this material at 298 K and 100 bar is twice that in powder HKUST-1. We plan to expand this strategy to other MOFs, such as M_2(dobdc) and M_2(*m*-dobdc), to achieve enhanced volumetric working capacities.

We will continue to devote efforts to in situ DRIFTS analysis for the elucidation of the temperature dependence of $\Delta H°$ and $\Delta S°$ upon H_2 adsorption in both physisorbed and backbonding systems. In order to probe H_2 binding sites at operational temperatures and pressures, we are in the process of upgrading the DRIFTS system with a quantitative high-pressure gas adsorption analyzer and combining the setup with a benchtop NMR spectrometer. By recording both NMR and IR spectra simultaneously, we will decipher the contributions of different adsorption sites to high-pressure H_2 uptake.

In concert with experimental data, computations of binding energies have validated the accuracy of an informed cluster model and subsequent optimization with high-quality range-separated hybrid functionals. Energy decomposition analysis on geometries gave additional insight into framework interactions with H_2, unraveling electrostatic, dispersion, polarization, and charge transfer effects. Evaluating free energy changes beyond existing architectures for large-sized clusters that incorporate anharmonic effects is a challenge that will be the focus of future computational endeavours. DFT computations combined with accurate free-energy predictions can play a key role in identifying binding motifs that give optimal usable capacities. We have identified inexpensive density functionals, such as GAM and B97M-V, that provide good accuracy in predicting binding energies for H_2 uptake in substrates composed of main group elements. In the future, we plan on extending this protocol to include transition-metal-containing substrates to represent the hydrogen storage problem more comprehensively.

We have estimated the levelized cost of hydrogen transmission and distribution in MOF fixed bed tube trailer systems. Given our estimates of energy and material balances and costs at the equipment level, we are now able to conduct detailed comparisons of technologies across a broad range of applications (e.g., long versus short range trips and low to high H_2 demand). This capability is critical for identifying cost reduction opportunities and for evaluating proposed configurations for storage technologies, transport infrastructure, and fueling stations. As our adsorption model was developed and tested using available experimental data, a clear next step is to simulation the effect of H_2 uptake at different temperatures and pressures on system-level costs. Here, it will be important to more precisely model heat management along with the desorption process. Additionally, we will employ sensitivity analysis techniques, such as Monte Carlo simulations, to understand the contribution of key parameters to overall costs, and complete a reverse-engineering analysis to identify material performance and properties where cost-parity is achieved with 500 bar trucks.

Hydrogen carriers. There is a need to develop faster catalysts to release hydrogen from carriers, while at the same time providing long-term stability. Our general strategy for future carrier work is to examine and define the advantages and challenges to using H_2 carriers to (i) transport H_2 to a city gate (e.g., a carrier capable of

producing 50,000 kg H_2/day), (ii) backup power for a data center, (e.g., the ability to store 5,000 kg H_2/day for up to 3 days), a microgrid neighborhood of 100 homes that would generate up to 5,000 kg H_2 in the summer and release up to 5,000 kg in the winter. Further specific work is planned for two areas.

- **Formate salts and formic acid.** The addition of formate salts is needed to provide the fastest rates of H_2 release from formic acid. Thus, we will look at mixtures of formic acid and formate salts to optimize both the rate and hydrogen storage density. We also propose to investigate the non-catalytic thermal hydrogen release from formate salts to investigate the proposal that more H_2 release is possible assuming the initial product, bicarbonate, leads to the decrease in activity of heterogeneous catalysts. We will also investigate catalyst stability from mixtures of formic acid and formate salts.
- **Modifying ΔH and ΔS in LOHCs.** Experimental validation of the calculated reaction enthalpy and entropy for the dehydrogenative coupling of alcohols provides an approach to reduce the magnitude of both ΔH, ca. 12.5 kJ/mol H_2, and ΔS. A low ΔS is necessary to realize a reversible reaction with a low ΔH. We suggest that the entropy loss from addition of H_2 to ethyl acetate is lower than a typical LOHC because the breaking of a carbon-carbon bond increases the entropy:

  $2CH_3CH_2OH \Leftrightarrow CH_3C(O)OCH_2CH_3 + 2H_2$ (theoretical density 53 g H_2/liter)

Magnesium borohydride. Our recent work has concluded that a less than stoichiometric amount of THF (or glyme) results in highest selectivity for $B_{10}H_{10}^{2-}$ and the fastest rate for H_2 release. Our future work will identify the specific intermediate leading to reversible storage in adducts of $Mg(BH_4)_2$ since we don't know what species are responsible for the cycling. It is possible that we currently have a mixture of reversible species and "regular" $Mg(BH_4)_2$. The regular $Mg(BH_4)_2$ does not cycle at these temperatures and so we can increase the density of storable H_2 if we could identify and synthesize the reversible species. We postulate that there are stable 0.67 and 0.5THF $Mg(BH_4)_2$ adducts that would tightly bind THF and yield 5–6 wt % H_2 reversibly.

Plasmonic materials will continue to improve the release of hydrogen to >2% w/w. Porous liquids demonstrate the ability to functionalize and re-suspend colloidal frameworks in various ionic liquids and/or liquid polymer solvents. Improve the reversible capacity by year's end to >0.1% w/w.

In year two, SLAC will build upon the goals outlined in year one and continue to establish collaborations with the HyMARC core team in order to help identify and overcome additional technological barriers by providing structure-property relationships under practical conditions. X-ray scattering and spectroscopic measurements involving groups at NREL, NIST, and PNNL are currently planned for the Stanford Synchrotron Radiation Light Source Fall 2019 cycle. Advanced synchrotron techniques (X-ray PDF, XRS) will also be used to provide in situ structural information previously unattainable (e.g., exact structural phase transformations between β-$Mg(BH_4)_2 \rightarrow MgB_{12}H_{12} \rightarrow MgB_2$). Additionally, SLAC will lead an Annual Operating Plan task to design an in situ ALD chamber compatible with SAXS/WAXS and XAS.

SPECIAL RECOGNITIONS AND AWARDS/PATENTS ISSUED

1. T. Gennett, K. Hurst, P. Parilla, DOE FCTO Hydrogen Storage award for excellence.
2. Plenary speaker at International Symposium on Metal-Hydrogen Systems, Guangzhou, China, October 2018.
3. Invited speaker at the International Conference on Boron Chemistry (ICBC-II), Taiyuan, China, July 2019.
4. Vice chair (chair elect 2021) Gordon Research Conference on Hydrogen-Metal Systems, July 2019.
5. Published invited perspective on Hydrogen Carriers. Challenges and Opportunities for Using Formate to Store, Transport, and Use Hydrogen.
6. Initiated collaboration on hydrogen carriers with Drs. Chang Won Yoon and Hyangsoo Jeong, KIST.
7. Edited special addition on Hydrogen Energy: Michael Hirscher, Tom Autrey, Shin-ichi Orimo. Hydrogen Energy. *ChemPhysChem* 2019, doi.org/10.1002/cphc.201900429, PNNL-SA-143944.

8. Hosted webinar on Hydrogen Carriers for Bulk Storage and Transport of Hydrogen, December 2018. https://www.energy.gov/eere/fuelcells/downloads/hydrogen-carriers-bulk-storage-and-transport-hydrogen-webinar.
9. Symposium organizer, Energy Storage in Chemical Bonds, ACS National Meeting, Spring 2019.
10. Symposium organizer for MRS 2020 Spring Meeting.
11. Provisional patent: "Encapsulated Hydrogen Fuels," USPTO Application No. 62/839,807, March 2018, Steve Christensen, Noemi Leick, Ashley Gaulding, Katherine Hurst, Thomas Gennett.

FY 2019 PUBLICATIONS/PRESENTATIONS

Publications

1. M.T. Kapelewski, T. Runčevski, J.D. Tarver, H.Z.H. Jiang, A. Ayala, T. Gennett, S.A. FitzGerald, C.M. Brown, and J.R. Long, "Evaluating Metal−Organic Frameworks for High-Pressure H_2 Storage: Record High Volumetric Capacity in Ni_2(*m*-dobdc)," *Chem. Mater.* 30, no. 22 (2018): 8179−8189.
2. T. Stauch, R. Chakraborty, and M. Head-Gordon, "Quantum Chemical Modeling of Pressure-Induced Spin Crossover in Octahedral Metal-Ligand Complexes," *ChemPhysChem* (2019): accepted author manuscript. DOI: 10.1002/cphc.201900853.
3. K.E. Hurst, T. Gennett, J. Adams, M.D. Allendorf, R. Balderas-Xicohténcatl, M. Bielewski, B. Edwards, L. Espinal, B. Fultz, M. Hirscher, M.L.S. Hudson, Zeric Hulvey, M. Latroche, D.-J. Liu, M. Kapelewski, E. Napolitano, Z.T. Perry, J. Purewal, V. Stavila, M. Veenstra, J.L. White, Y. Yuan, H.-C. Zhou, C. Zlotea, and P. Parilla, "An International Laboratory Comparison Study of Volumetric and Gravimetric Hydrogen Adsorption Measurements," *ChemPhysChem* 20, no. 15 (2019): 1997.
4. W.A. Braunecker, S. Shulda, M.B. Martinez, K.E. Hurst, J.T. Koubek, S. Zaccarine, S. Pylypenko, A. Sellinger, T. Gennett, and J.C. Johnson, "Thermal Activation of a Copper-Loaded Covalent Organic Framework for Near-Ambient Temperature Hydrogen Storage and Delivery," *ACS Materials Lett.*, submitted.
5. B.R. Barnett, H.A. Evans, G.M. Su, H.Z.H. Jiang, R. Chakraborty, M.B. Martinez, B.A. Trump, J.D. Tarver, M.N. Dods, W.S. Drisdell, K.E. Hurst, T. Gennett, S.A. FitzGerald, C.M. Brown, M. Head-Gordon, and J.R. Long, "Activated adsorption of hydrogen at a metal–organic framework open metal site occurring via a physisorbed precursor," Submitted to *Science* 2019.
6. K.W. Muller, S. Autrey, and K.P. Brooks, "Releasing Hydrogen at High Pressures from Liquid Carriers: Aspects for the H2 Delivery to Fueling Stations," *Energy and Fuels* (2018). doi:10.1021/acs.energyfuels.8b01724.
7. Y. Yu, T. He, A. Wu, Q. Pei, A.J. Karkamkar, S. Autrey, and P. Chen, "Reversible hydrogen uptake/release over sodium phenoxide-cyclohexanolae pair," *Angewandte Chemie International Edition* 58, no. 10 (2019): 3102–3107. doi:10.1002/anie.201810945.
8. M. Hirscher, S. Autrey, and S. Orimo, "Hydrogen Energy," *ChemPhysChem* 20, no. 10 (2019): 1157–1157. doi:10.1002/cphc.201900429.
9. K. Grubel, H. Jeong, C. Yoon, and S. Autrey, "Challenges and Opportunities for using Formate to Store, Transport and Utilize Hydrogen," *Journal of Energy Chemistry 41* (2020). doi:10.1016/j.jechem.2019.05.016.
10. M.D. Allendorf, Z. Hulvey, T. Gennett, A. Alauddin, S. Autrey, J. Camp, and E. Cho, et al, "An Assessment of Strategies for the Development of Solid-State adsorbents for Vehicular Hydrogen Storage," *Energy and Environmental Science* 11, no. 10 (2018): 2784–2812. doi:10.1039/c8ee01085d.
11. T.W. Heo and B.C. Wood, "On thermodynamic and kinetic mechanisms for stabilizing surface solid solutions," manuscript in review (2019).

12. Y.-S. Liu, L.E. Klebanoff, P. Wijeratne, D.F. Cowgill, V. Stavila, T.W. Heo, S. Kang, A.A. Baker, J.R.I. Lee, K.G. Ray, J.D. Sugar, and B.C. Wood, "Investigating potential kinetic limitations to MgB2 hydrogenation," *Int. J. Hydrogen Energy*, in press (2019).

13. L.F. Wan, E.S. Cho, T. Marangoni, P.T. Shea, S. Kang, C. Rogers, E.W. Zaia, R.R. Cloke, B.C. Wood, F.R. Fisher, J.J. Urban, and D. Prendergast, "Edge-functionalized graphene nanoribbon encapsulation to enhance stability and control kinetics of hydrogen storage materials," *Chem. Mater.* 31 (2019): 2960.

14. X.W. Zhou, S. Kang, T.W. Heo, B.C. Wood, V. Stavila, and M.D. Allendorf, "An analytical bond order potential for Mg-H systems," *ChemPhysChem* 20 (2019): 1404.

15. S. Kang, T.W. Heo, M.D. Allendorf, and B.C. Wood, "Morphology-dependent stability of complex metal hydrides and their intermediates using first-principles calculations," *ChemPhysChem* 20 (2019): 1340.

16. J.L. White, A.J.E. Rowberg, L.F. Wan, S. Kang, T. Ogitsu, R.D. Kolasinski, J.A. Whaley, A.A. Baker, J.R.I. Lee, Y.-S. Liu, L. Trotochaud, J. Guo, V. Stavila, D. Prendergast, H. Bluhm, M.D. Allendorf, B.C. Wood, and F. El Gabaly, "Identifying the role of dynamic surface hydroxides in the dehydrogenation of Ti-doped $NaAlH_4$," *ACS Appl. Mater. Interfaces* 11 (2019): 4930.

17. A. Schneemann, J.L. White, S. Kang, S. Jeong, L.F. Wan, E.S. Cho, T.W. Heo, D. Prendergast, J.J. Urban, B.C. Wood, M.D. Allendorf, and V. Stavila, "Nanostructured metal hydrides for hydrogen storage," *Chem. Rev.* 118 (2018): 10775.

18. V. Stavila, M.E. Foster, J.W. Brown, R.W. Davis, J. Edgington, A.I. Benin, R.A. Zarkesh, R. Parthasarathi, D.W. Hoyt, E.D. Walter, A. Andersen, N.M. Washton, A.S. Lipton, and M.D. Allendorf, "IRMOF-74(*n*)-Mg: A Novel Catalyst Series for Hydrogen Activation and Hydrogenolysis of C-O Bonds," *Chem. Sci.* (2019), DOI: 10.1039/C9SC01018A.

19. Y.S. Liu, S. Jeong, J.L. White, X.F. Feng, E.S. Cho, V. Stavila, M.D. Allendorf, J.J. Urban, and J.H. Guo, "In-Situ/Operando X-ray Characterization of Metal Hydrides," *ChemPhysChem* 20 (2019): 1261, doi:10.1002/cphc.201801185.

20. T.C. Wang, J.L. White, B.L. Bie, H.X. Deng, J. Edgington, J.D. Sugar, V. Stavila, and M.D. Allendorf, "Design Rules for Metal-Organic Framework Stability in High-Pressure Hydrogen Environments," *ChemPhysChem* 20 (2019): 1305, doi:10.1002/cphc.201801190.

21. S. Kang, T.W. Heo, M.D. Allendorf, and B.C. Wood, "Morphology-Dependent Stability of Complex Metal Hydrides and Their Intermediates Using First-Principles Calculations," *ChemPhysChem* 20 (2019): 1340, doi:10.1002/cphc.201801132.

22. X.W. Zhou, S. Kang, T.W. Heo, B.C. Wood, V. Stavila, and M.D. Allendorf, "An Analytical Bond Order Potential for Mg-H Systems," *ChemPhysChem* 20 (2019): 1404, doi:10.1002/cphc.201800991.

23. J.L. White, A.J.E. Rowberg, L.W.F. Wan, S. Kang, T. Ogitsu, R.D. Kolasinski, J.A. Whaley, A.A. Baker, J.R.I. Lee, Y.S. Liu, L. Trotochaud, J.G. Guo, V. Stavila, D. Prendergast, H. Bluhm, M.D. Allendorf, B.C. Wood, and F. El Gabaly, "Identifying the Role of Dynamic Surface Hydroxides in the Dehydrogenation of Ti-Doped NaAlH4," *ACS Appl. Mater. Interfaces* 11 (2019): 4930, doi:10.1021/acsami.8b17650.

24. A. Schneemann, J.L. White, S. Kang, S. Jeong, L.W.F. Wan, E.S. Cho, T.W. Heo, D. Prendergast, J.J. Urban, B.C. Wood, M.D. Allendorf, and V. Stavila, "Nanostructured Metal Hydrides for Hydrogen Storage," *Chem. Rev.* 118 (2018): 10775, doi:10.1021/acs.chemrev.8b00313.

25. S. Jeong, P.J. Milner, L.F. Wan, Y.-S. Liu, J. Oktawiec, E.W. Zaia, A.C. Forse, N. Leick, T. Gennett, J. Guo, D. Prendergast, J.R. Long, and J.J. Urban, "Runaway Carbon Dioxide Conversion Leads to Enhanced Uptake in a Nanohybrid Form of Porous Magnesium Borohydride," *Advanced Materials* (2019): 1904252.

26. C. Sugai, S. Kim, G. Severa, J.L. White, N. Leick, M.B. Martinez, T. Gennett, V. Stavila, and C. Jensen, "Kinetic Enhancement of Direct Hydrogenation of MgB_2 to $Mg(BH_4)_2$ upon Mechanical Milling with THF, MgH_2, and/or Mg," *ChemPhysChem.* 20 (2019): 1301.

27. M. Dzara, K. Artyushkova, S. Shulda, M. Strand, C. Ngo, E. Crumlin, T. Gennett, and S. Pylypenko, "Characterization of Complex Interactions at the Gas–Solid Interface with in Situ Spectroscopy: The Case of Nitrogen-Functionalized Carbon," *The Journal of Physical Chemistry C* 123, no. 14 (2019): 9074–9086

28. Sohee Jeong, Tae Wook Heo, Julia Oktawiec, Rongpei Shi, ShinYoung Kang, James L. White, Edmond W. Zaia, Liwen F. Wan, Keith G. Ray, Yi-Sheng Liu, Vitalie Stavila, Jinghua Guo, Jeffrey R. Long, Brandon C. Wood, and Jeffrey J. Urban, "Unveiling the mechanism of phase evolution and hydrogen storage behavior in nanocrystalline $Mg(BH_4)_2$ within reduced graphene oxide," under review (2019).

29. Yi-Sheng Liu, Sohee Jeong, Xuefei Feng, Eun Seon Cho, James White, Vitalie Stavila, Mark D. Allendorf, Jeffrey J. Urban, and Jinghua Guo, "In-situ/operando multimodal soft x-ray characterization in energy science," *Chem. Phys. Chem.* (2019).

30. Sohee Jeong, Phillip Milner, Liwen F. Wan, Yi-Sheng Liu, Julia Oktawiec, Edmond W. Zaia, Jinghua Guo, David Prendergast, Jeffrey R. Long, and Jeffrey J. Urban, "'Runaway' carbon dioxide conversion leads to enhanced sorption in a nanohybrid porous magnesium metal hydride," *Advanced Materials,* accepted (2019). Work highlighted in C&E News.

31. Tracy M. Mattox, Anne L. Pham, Andrew Doran, and Jeffrey J. Urban, "Cation lattice influence on hydrogenation kinetics in sodium borohydride," in preparation (2019).

Presentations:

1. N. Leick, "A Glimpse Into NREL's Hydrogen Storage Efforts," NREL seminar, Golden, CO, September 24, 2019.
2. S. Christensen, N. Leick, K. Gross, S. Pylypenko, M. Fitzgerald, "ALD (Atomic Layer Deposition) Synthesis of Novel Nanostructured Metal Borohydrides," HyMARC Seedling Tech Team, Detroit, MI, September 19, 2019.
3. Courtney Pailing, "HyMARC Data Hub Overview and Tutorial," HyMARC Face to Face Meeting, July 17 at PNNL.
4. "N. Leick, V. Stavila, N. Strange, M. Martinez, M. Toney, T. Gennett, S. Christensen, "Atomic Layer Deposition on $Mg(BH_4)_2$: A Route to Improved Automotive H_2 Storage,"
5. 19th Atomic Layer Deposition Conference, Seattle, WA, July 22-24, 2019.
6. N. Leick, T. Mattox, T. Gennett, J. Urban, "Modulation of B-H Bond Strength in Borohydrides,"
7. HyMARC Annual Face-to-Face Meeting, Richland, WA, July 17-18, 2019.
8. S. Shulda, P. Parilla, N. Strange, M. Toney, and T. Gennett, "Multi-Technique Characterization of Hydrogen Storage Materials for Improved Material Development," GRC, Barcelona, July 2019.
9. S. Shulda, P. Parilla, N. Strange, M. Toney, and T. Gennett, "Multi-Technique Characterization of Hydrogen Storage Materials for Improved Material Development," NREL MST Technical Review, September 2019.
10. N. Strange, S. Shulda, T. Gennett, and M. Toney, "HyMARC: Technical Activities at SLAC," Stanford Hydrogen Energy Workshop, March 2019, Poster Presentation.
11. N. Strange, S. Shulda, T. Gennett, and M. Toney, "HyMARC: Technical Activities at SLAC," Hydrogen and Fuel Cells Program Annual Merit Review and Peer Evaluation Meeting, May 2019, Poster Presentation.
12. N. Strange, M. Toney, S. Shulda, and T. Gennett, "X-Ray Characterization at SLAC," HyMARC Face-to-Face Meeting, July 2019, Oral Presentation.
13. N. Strange, S. Shulda, S. Christensen, N. Leick, T. Gennett, and M. Toney, "Characterization of Hydrogen Storage Materials Using Advanced Synchrotron Scattering and Spectroscopic Techniques," Stanford Synchrotron Radiation Light Source /LCLS Joint Users' Meeting, September 2019, Poster Presentation.

14. H. Furukawa, "Chemistry of Metal–Organic Frameworks," Department Seminar, Soongsil University, Seoul, Korea, November 19, 2018.
15. H. Furukawa, "Metal–Organic Frameworks with Exposed Metal Sites," UNIST seminar, Ulsan National Institute of Science and Technology (UNIST), Ulsan, Korea, November 20, 2018.
16. H. Furukawa, "Chemistry of Metal–Organic Frameworks," Department Seminar, Sookmyung Women's University, Seoul, Korea, November 21, 2018.
17. J.R. Long, M. Head-Gordon, and H.M. Breunig, "HyMARC: LBNL Technical Activities," H_2 Storage Tech Team (H_2ST^2) Meeting, Southfield, MI, February 20, 2019.
18. D. Prendergast and J.R. Long, "HyMARC: LBNL Technical Activities," 2019 DOE Hydrogen and Fuel Cells Program Review, Washington, DC, May 1, 2019.
19. S.P. Veccham and M. Head-Gordon, "Assessment of the Performance of Density Functionals for Hydrogen Storage in Sorbents," 257th ACS National Meeting & Exposition, Orlando, FL, April 3, 2019.
20. B.R. Barnett and J.R. Long, "Structural and Kinetic Effects of Framework-Dihydrogen Covalency," Nanoporous Materials Seminar, Center for Gas Separations, Berkeley, CA, June 26, 2019.
21. A. Anastasopoulou and H.M. Breunig, "Techno-economic and Life Cycle Assessment Framework for Methane and Hydrogen Storage in Advanced Porous Materials," International Symposium on Sustainable Systems & Technology, Portland, OR, June 27, 2019.
22. B.R. Barnett and J.R. Long, "Leveraging π-Basicity in Metal–Organic Frameworks for Ambient Temperature Hydrogen Storage: Structural, Thermodynamic, and Kinetic Insights," 258th American Chemical Society National Meeting, San Diego, CA, August 27, 2019.
23. H. Furukawa, "Design and Synthesis of Metal–Organic Frameworks for Hydrogen Storage Applications," Department Seminar, Tokyo Metropolitan University, Tokyo, Japan, September 10, 2019.
24. R.E. Mow, W.A. Braunecker, M.B. Martinez, S. Shulda, and T. Gennett, "Porous liquids from framework materials," Gordon Research Conference, Nanoporous Materials and Their Applications, Aug. 4-9, 2019, Andover, NH.
25. W.A. Braunecker, "Porous Liquids as Hydrogen Carriers," HyMARC Face-to-Face Meeting, PNNL, July 19, 2019.
26. W.A. Braunecker, M.B. Martinez, K.E. Hurst, S. Shulda, J.T. Koubek, A. Sellinger, T. Gennett, and J.C. Johnson, "Hydrogen sorption in fluorinated organic frameworks," 257th ACS Meeting, Mar. 31-Apr. 4, 2019, Orlando, FL, ENFL–0607.
27. R.E. Mow, M.B. Martinez, T. Gennett, and W.A. Braunecker, "Porous liquid covalent organic frameworks," 257th ACS Meeting, Mar. 31-Apr. 4, 2019, Orlando, FL, ENFL–0446.
28. W.A. Braunecker, "Fluorinated Organic Materials for Energy Generation, Storage, and Transport Applications," Colorado School of Mines Seminar Series, Feb. 22, 2019.
29. W.A. Braunecker, "Porous Liquids as Hydrogen Carriers," Phase 2 kick-off meeting, LLNL, Sept. 25, 2019.
30. W.A. Braunecker, "Thermo/photo responsive sorbent matrices," Phase 2 kick-off meeting, LLNL, Sept. 26, 2019.
31. Ashley Gaulding, Katie Hurst, Madison Martinez, Jeff Urban, and Tom Gennett, "H_2 Release via Plasmonic Heating," Tech Team Meeting, Detroit, MI, February 10, 2019.
32. Katie Hurst, Ashley Gaulding, Madison Martinez, Noemi Leick, Steve Christensen, Sarah Shulda, Nick Strange, Tom Gennett, David Prendergast, and Jeff Urban, "Plasmon interactions for on-demand hydrogen release in hydrogen carriers," HyMARC Face to Face Meeting Richland, WA, July 17, 2019.

33. Katherine Hurst, Ashley Gaulding, Madison Martinez, Noemi Leick, Steve Christensen, Sarah Shulda, and Tom Gennett, "Plasmonic Mediated Hydrogen Desorption from Metal Hydrides," ALD 2019, Oral presentation, July 22, 2019.
34. Katherine Hurst, Philip Parilla, Sarah Shulda, Wade Braunecker, Nick Strange, Justin Johnson, and Thomas Gennett, "Measurement and Materials for Hydrogen Storage," Department of Metallurgical and Materials Engineering Seminar, Colorado School of Mines, April 11, 2019.
35. M.E. Bowden, S. Autrey, M.O. Jones, B. Ginovska, K. Chernichenko, T. Repo, and A.J. Rameriz-Cuesta, "Hydrogen chemi-sorption in condensed-phase Frustrated Lewis acid-base Pairs," presented by M.E. Bowden at ACS National Meeting, Orlando, Florida, April 3, 2019.
36. K. Grubel, H. Jeong, M.E. Bowden, A.J. Karkamkar, and S. Autrey, "Hydrogen Carriers: Storage and Transport; The Formic Acid/Formate Pathway," presented by K. Grubel at 13th International Symposium Hydrogen & Energy, Incheon, Republic of Korea, January 20, 2019.
37. I.H. Nayyar, B. Ginovska, A.J. Karkamkar, M.E. Bowden, and S. Autrey, "Accelerating development of hydrogen storage materials through HYMARC, a U.S. DOE national laboratory-led consortium," Guangzhou, China, October 29, 2018.
38. A.J. Karkamkar, "Hydrogen Release from Solvated Magnesium Borohydride," presented at 2nd International Conference on Boron Chemistry, Taiyuan, China, July 15, 2019.
39. S. Kang, "Advanced modeling of thermodynamics in complex metal hydrides for hydrogen storage," Korea Advanced Institute of Science and Technology, Daejeon, Korea, October 2018.
40. S. Kang, "First-Principles Modeling of Hydrogen Storage Materials," Korea Research Institute of Standards and Science, Daejeon, Korea, October 2018.
41. S. Kang, "Multiscale Simulations of Entropy and Phase Nucleation in the Mg-B-H System," International Symposium Hydrogen & Energy, Incheon, Korea, January 2019.
42. S. Kang, "Advanced Modeling of De-/Rehydrogenation of Complex Metal Hydrides for Hydrogen Storage (Theoretical activities in HyMARC)," Livermore, CA, USA, March 2019.
43. S. Kang et al., "Modeling of Thermodynamics and Nucleation Kinetics in the Mg-B-H System," Orlando, FL, USA, April 2019.
44. S. Kang, "Size-dependent lattice parameters of Mg nanoparticles," KAIST Workshop, Daejeon, South Korea, May 2019.
45. S. Kang, "Improved thermodynamics and phase diagram prediction of the Mg-B-H system," HyMARC Face-to-Face Meeting, PNNL, July 2019.
46. S. Wan, "Modeling of B-H and B-B bond activation by catalytic additives," HyMARC Face-to-Face Meeting, PNNL, July 2019.
47. S. Weitzner, "Modeling the performance and stability of formate synthesis and dehydrogenation catalysts: Atomistic modeling strategies," HyMARC Face-to-Face Meeting, PNNL, July 2019.
48. T.W. Heo, "Interfaces, microstructures, and mechanical stress in metal hydrides," HyMARC Face-to-Face Meeting, PNNL, July 2019.
49. S. Kang, "Predicting chemical and structural properties of complex interfaces in battery and hydrogen storage materials," Warsaw, Poland, September 2019.
50. B.C. Wood, "Understanding reactive interfaces in complex metal hydrides through multiscale simulations," 16th International Symposium on Metal-Hydrogen Systems, Guangzhou, China, October 2018 (invited).
51. B.C. Wood, "Modeling kinetic mechanisms governing hydrogen interactions with complex hydrides," Korea Advanced Institute of Science and Technology, Daejeon, Korea, October 2018.

52. T.W. Heo, "HyMARC mesoscale modeling efforts for metal hydrides," Korea Advanced Institute of Science and Technology, Daejeon, Korea, October 2018.
53. B.C. Wood, "Hydrogen materials research at the U.S. Department of Energy: A high-performance computing perspective," Hyundai Motors Hydrogen Energy Development Team, Seoul, Korea, October 2018.
54. B.C. Wood, "Atomic-scale computational studies of metal hydrides within the HyMARC Consortium," Helmholtz-Zentrum Geesthacht, Germany, December 2018.
55. T.W. Heo, "HyMARC mesoscale modeling efforts for metal hydrides," Helmholtz-Zentrum für Material und Küstenforschung, Geesthacht, Germany, December 2018.
56. B.C. Wood, "Probing complex interfaces for renewable production and storage of hydrogen," San Francisco State University, February 2019.
57. B.C. Wood, "Multiscale modeling of reactive interfaces for chemical storage of hydrogen fuel," American Chemical Society Spring Meeting, Orlando, FL, April 2019 (invited).
58. B.C. Wood, "Heading towards a hydrogen-powered future," Modesto Area Partners in Science Lecture Series, Modesto, CA, September 2019.
59. B.C. Wood, "HyMARC: Atomistic modeling of metal hydrides for hydrogen storage," Helmholtz-Zentrum für Material und Küstenforschung, Geestacht, Germany, July 2019.
60. T.W. Heo, "HyMARC: Mesoscale modeling of metal hydrides for hydrogen storage," Helmholtz-Zentrum für Material und Küstenforschung, Geesthacht, Germany, July 2019.
61. B.C. Wood, "Multiscale simulations of metal hydrides for the DOE HyMARC Consortium," Helmut-Schmidt University, Hamburg, Germany, July 2019.
62. B.C. Wood, "Computational hydrogen materials research at the U.S. Department of Energy," Korea Institute of Science and Technology, Seoul, Korea, May 2019.
63. B.C. Wood, "Complex dynamics in metal hydroborates: From hydrogen storage to solid-state batteries," European Materials Research Society Fall Meeting, Warsaw, Poland, September 2019.
64. B.C. Wood, "Probing interfaces in complex metal hydrides through multiscale simulations," Gordon Research Conference on Metal-Hydrogen Systems, Barcelona, Spain, July 2019 (poster).
65. B.C. Wood, "HyMARC: LLNL technical activities," Hydrogen Storage Tech Team Review, Southfield, MI, February 2019.
66. B.C. Wood, "HyMARC: LLNL technical activities overview," FCTO Site Visit, Livermore, CA, September 2019.
67. S. Kang, "Thermodynamics of metal hydrides," FCTO Site Visit, Livermore, CA, September 2019.
68. T.W. Heo, "Interfaces, microstructures, and mechanical stress in metal hydrides," FCTO Site Visit, Livermore, CA, September 2019.
69. S. Wan, "Modeling of B-H and B-B bond activation by catalytic additives," FCTO Site Visit, Livermore, CA, September 2019.
70. K. Ray, "Direct simulation of MgB_2 hydrogenation," FCTO Site Visit, Livermore, CA, September 2019.
71. J. Lee and A. Baker, "X-ray spectroscopy of boron compounds," FCTO Site Visit, Livermore, CA, September 2019.
72. S. Akhade, "Heterogeneous catalysts for liquid organic hydrogen carriers," FCTO Site Visit, Livermore, CA, September 2019.

73. M.D. Allendorf, "Hybrid and Functionalized MOFs for Fuel Production, Transport, and Storage," Hybrid Functional Porous Materials: MOFs, Silica and Conductive Polymers Symposium, ACS Fall 2019 Meeting, San Diego, CA, Aug. 25–30, 2019, invited presentation.

74. V. Stavila, "Understanding Hydrogen Desorption Pathways in Nanoscale Metal Hydrides," Research Conference on Hydrogen-Metal Systems, Castelldefels, Spain, June 30–July 5, 2019.

75. V. Stavila, L. Klebanoff, J. Su, G. Somorjai, D. Prendergast, T. Autrey, and M. Allendorf, "Sustainable hydrogen storage in polyalcohols enabled by metal-organic framework catalysts," National Meeting of the American Chemical Society, Mar. 31–Apr. 4, 2019, Orlando, FL.

76. B. Wood, T. W. Heo, S. Kang, K. Ray, L. Wan, A. Rowberg, A. Baker, J. Lee, J. White, F. El Gabaly, V. Stavila, and L. Klebanoff, "Multiscale modeling of reactive interfaces for chemical storage of hydrogen fuel," National Meeting of the American Chemical Society, Mar. 31–Apr. 4, 2019, Orlando, FL.

77. Phil Parilla, "Optimum Thermodynamic Properties and Isosteric Heat Determination," Status Update Meeting with DOE, November 1, 2018.

78. Philip Parilla, "HyMARC Hydrogen Storage Research at NREL," 13th Int. Symposium Hydrogen & Energy, Incheon, Korea, January 21, 2019, invited.

79. Philip Parilla, "Thermodynamic Investigations," Tech. Team Meeting, February 21, 2019.

80. R. Bell, W. Braunecker, S. Christensen, M. Dimitrievska, A. Gaulding, K. Hurst, J. Johnson, N. Leick, M. Martinez, R. Mow, P. Parilla, S. Shulda, N. Strange, T. Gennett, G. Russell-Parks, B. Trewyn, and C. Wolden, "Thermodynamic Investigations," DOE site visit to NREL, April 10, 2019.

81. Thomas Gennett, Phil Parilla, Katie Hurst, Steve Christensen, Kristin Munch, Courtney Pailing, Wade, Braunecker, John Perkins, Sarah Shulda, Robert Bell, Noemi Leick, Madison Martinez, Jacob Tarver, Mira Dimitrievska, Nick Strange, Gayle Bentley, Ashley Gaulding, Rachel Mow, Glory Russel-Parks, "NREL HyMARC Technical Activities," DOE Hydrogen and Fuel Cells Program, 2019 Annual Merit Review and Peer Evaluation Meeting, May 1, 2019.

82. Phil Parilla, "Issues with Isosteric Heat Determination," HyMARC AOP Meeting, Lawrence Livermore National Laboratory, July 17, 2019.

83. Robert Bell, Phil Parilla, and Thomas Gennett, "Additive & Eutectic systems as hydrogen carriers," November 2018 DOE Site Visit, NREL.

84. Robert Bell, Glory Russell-Parks, Amelia Huffer, Sarah Shulda, Madison Martinez, Noemi Leick, Philip Parilla, Brian Trewyn, and Thomas Gennett, "Ionic Liquid Additives for Lowering the Decomposition Temperature of Magnesium Borohydride," April 2019 ACS Spring Meeting, Orlando, FL.

85. Robert Bell, Thomas Gennett, and Noemi Leick, "Improving $Mg(BH_4)_2$ Cyclability with Borohydride Salt Additives," July 2019 Face to Face Meeting, PNNL.

86. S. Christensen, N. Leick, K. Gross, M. Fitzgerald, and S. Pylypenko, "ALD (Atomic Layer Deposition) Synthesis of Novel Nanostructured Metal Borohydrides," DOE Hydrogen and Fuel Cells Program Annual Merit Review, Washington, D.C., April 2019.

87. S. Christensen, N. Leick, K. Gross, M. Fitzgerald, and S. Pylypenko, "ALD (Atomic Layer Deposition) Synthesis of Novel Nanostructured Metal Borohydrides: Progress Report," FCTO Hydrogen Storage Program face-to-face meeting, Richland, Washington, July 2019.

88. S. Christensen, V. Stavila, B. Wood, and T. Heo, "Nano-confined metal hydrides under mechanical stress: Progress Update," FCTO Hydrogen Storage Program face-to-face meeting, Richland, Washington, July 2019.

89. N. Leick, K. Gross, M. Fitzgerald, S. Pylypenko, T. Gennett, and S. Christensen, "Atomic Layer Deposition on $Mg(BH_4)_2$: A Route to Improved Automotive H_2 storage," invited talk, ALD 2019 – AVS, Seattle, Washington, July 2019.

90. S. Christensen, N. Leick, K. Gross, M. Fitzgerald, and S. Pylypenko, "ALD (Atomic Layer Deposition) Synthesis of Novel Nanostructured Metal Borohydrides: Progress Report," DOE Hydrogen Storage Tech Team, Southfield, Michigan, September 2019.

91. Gayle Bentley and Steve Christensen, "Biologically-based hydrogen production, storage, and release: a high efficiency H_2 production platform," LDRD presentation, April 2019, NREL.

92. Gayle Bentley, Steve Christensen, Thomas Gennett, "Biological formate-to-H_2 cycle," HyMARC Face-to-Face Meeting presentation, PNNL, July 2019.

REFERENCES

1. T. Tian, Z.X. Zeng, D. Vulpe, M.E. Casco, G. Divitini, P.A. Midgley, J. Silvestre-Albero, J.C. Tan, P.Z. Moghadam, and D. Fairen-Jimenez, *Nat. Mater.* 17 (2018): 174.

2. A. Schneemann, J.L. White, S. Kang, S. Jeong, L.W.F. Wan, E.S. Cho, T.W. Heo, D. Prendergast, J.J. Urban, B.C. Wood, M.D. Allendorf and V. Stavila, *Chem. Rev.* 118 (2018): 10775–10839.

3. U.S. Department of Energy Fuel Cell Technologies Office Hydrogen Storage Materials Database, http://hydrogenmaterialssearch.govtools.us/.

4. D. Denysenko, M. Grzywa, J. Jelic, K. Reuter, D. Volkmer, "Scorpionate-Type Coordination in MFU-4*l* Metal–Organic Frameworks: Small-Molecule Binding and Activation upon the Thermally Activated Formation of Open Metal Sites," *Angew. Chem. Int. Ed.* 53, no. 23 (2014): 5832–5836.

5. M.I. Gonzalez, E.D. Bloch, J.A. Mason, S.J. Teat, and J.R. Long, "Single-Crystal-to-Single-Crystal Metalation of a Metal−Organic Framework: A Route toward Structurally Well-Defined Catalysts," *Inorg. Chem.* 54, no. 6 (2015): 2995−3005.

6. J.A. Mason, J. Oktawiec, M.K. Taylor, M.R. Hudson, J. Rodriguez, J.E. Bachman, M.I. Gonzalez, A. Cervellino, A. Guagliardi, C.M. Brown, P.L. Llewellyn, N. Masciocchi, and J.R. Long, "Methane Storage In Flexible Metal–Organic Frameworks With Intrinsic Thermal Management," *Nature* 527, no. 7578 (2015): 357–361.

7. M.K. Taylor, T. Runčevski, J. Oktawiec, M.I. Gonzalez, R.L. Siegelman, J.A. Mason, J. Ye, C.M. Brown, and J.R. Long, "Tuning the Adsorption-Induced Phase Change in the Flexible Metal−Organic Framework Co(bdp)," *J. Am. Chem. Soc.* 138, no. 45 (2016): 15019−15026.

8. T. Tian, Z. Zeng, D. Vulpe, M.E. Casco, G. Divitini, P.A. Midgley, J. Silvestre-Albero, J.-C. Tan, P.Z. Moghadam, and D. Fairen-Jimenez, "A Sol–Gel Monolithic Metal–Organic Framework with Enhanced Methane Uptake," *Nat. Mater.* 17, no. 2 (2018): 174–179.

9. Y. Peng, V. Krungleviciute, I. Eryazici, J.T. Hupp, O.K. Farha, and T. Yildirim, "Methane Storage in Metal–Organic Frameworks: Current Records, Surprise Findings, and Challenges," *J. Am. Chem. Soc.* 135, no. 32 (2013): 11887–11894.

10. S. Kang, T.W. Heo, M.D. Allendorf, and B.C. Wood, "Morphology-dependent stability of complex metal hydrides and their intermediates using first-principles calculations," *ChemPhysChem* 20 (2019): 1340.

11. Zavorotynska et al., *J. Mat. Chem. A* 3 (2015): 6592.